The spatial variability and structure of turbulent kinetic energy in the convective boundary layer over an isolated mountain

Mark D. Sghiatti
B.S., University of Georgia, 2012

A Thesis presented to the Graduate Faculty of the University of Virginia in Candidacy for the Degree of Master of Science

Department of Environmental Science

University of Virginia

May 2016

Abstract

Convective boundary layer (CBL) turbulence is not well understood over mountainous terrain. In the presences of topography, orographic forcings can create a multitude of sub-mesoscale phenomena that affect turbulence variability in the CBL. Improvement of numerical weather prediction relies on observations and an understanding of the effects of such phenomena on turbulence. The objectives of this study are to investigate the spatial variability of turbulent kinetic energy (TKE) and to distinguish the underlying mechanisms generating turbulence in a CBL over and around the isolated mountain, Granite Peak, Utah. To address these objectives, the analysis utilizes *in-situ* 10 Hz meteorological and Doppler Wind Lidar observations collected by a Navy Twin Otter research aircraft in the Fall 2012 Mountain Terrain Atmospheric Observations and Modeling Experiment (MATERHORN). The spatial variability of TKE is investigated by calculating TKE from *in-situ* airborne observations over and around Granite Peak. To examine the mechanisms important for TKE generation, the TKE budget terms of shear production, buoyancy production, and dissipation are estimated from *in-situ* aircraft and Twin Otter Doppler Wind Lidar observations. TKE estimated from aircraft show TKE maxima directly over ridge tops, the crest of Granite Peak, and in and at the exit of a terrain gap. Results from the TKE budget analysis indicate buoyancy production is a dominant contributor to TKE in the CBL at lower levels over ridge tops and the crest of Granite Peak. However, shear production is also a dominant source of turbulence within and above the CBL due to entrainment of higher momentum from aloft. During periods with winds > 5 m s^{-1}, dynamically forced flows are an important mechanism for shear production of TKE above the CBL. Based on our findings, we show that TKE variability is significantly influenced by topography and that shear production can be a dominant production mechanism in and above the CBL over an isolated mountain. The variability and generation of TKE are due to a complex array of phenomena including buoyant plumes, entrainment processes, and dynamically driven terrain flows. This study provides information for improving the representation of turbulence variability and the mechanisms important for turbulence generation over complex terrain.

Acknowledgements

I would like to express my gratitude to my advisor Stephan de Wekker for his patience and guidance through my research. He has given me many opportunities to expand my scientific and professional horizon. A big thanks to Zeljko Vecenaj for taking time out of his busy schedule in Croatia to share his deep knowledge of aircraft turbulence analysis with me. In addition, I am grateful for his many helpful suggestions regarding analysis methods and goals for my research. I would also like to thank Dave Emmitt for taking time out of his work to meet and discuss science. He shared his expansive knowledge of aircraft meteorological observations and analysis methods. Without such teachings, I would have been lost. Additionally, I wish to thank my committee members, Todd Scanlon and Bob Davis. They have provided helpful feedback and support over the course of my work.

San dip Pal has been instrumental towards the development and progress of my research. We both share the experience of the MATERHORN campaign and the harsh and unforgiving Dugway, Utah. He has provided help and guidance since the very first seconds we met in the middle of the desert. I not only consider him a great colleague but also a great friend. My office mate and friend Nevio Babic has been a great resource of knowledge and suggestions. His scientific intellect is only second to his fellow country mate Nicola Tesla. Nevio has provided me with unwavering encouragement, which has allowed me to push forward during challenging periods of my research. I don't think I would be here without Stephanie Phelps. She allowed me first to connect with Stephan. Stephanie also helped me acclimate to graduate life and the lab group. Temple Lee taught me the ins and outs of field work. I thank him for his patience and thorough teachings on all things related to meteorological instrumentation.

On a more personal note, I would like to thank Olivia Stoken for personal and scientific encouragement. She has provided me with vital aid after an injury and subsequent surgery. Her patience and instrumental care have allowed me to stay healthy and positive during some challenging times. Without her, it would have been tough to stay motivated. Of course, I would not be here without the love and support of my parents. I owe infinite thanks for their continued encouragement and help in many aspects not just related to my research.

Contents

List of Figures

List of Tables

This thesis is dedicated to my mom and sister. They are two of the best people I know.

Chapter 1

Introduction

1.1 Introduction

The planetary boundary layer (PBL) is part of the lowest 100 to 3000 m of the troposphere that is directly influenced by the presence of the earth's surface, and responds to surface forcings with a timescale of about an hour or less (Stull 1988). Turbulent transport of heat and moisture from the surface is mixed through the PBL before being available to the circulation of the free atmosphere (FA). These transport processes are important in the atmosphere and affect the formation and dissipation of atmospheric phenomena such as pollutant transport, convection, and cloud formation. In general, during daytime fair weather conditions, turbulence is mainly generated by convection in the PBL and is therefore referred to as the unstable or convective boundary layer (CBL). Because CBL turbulence has an influence on many atmospheric processes, numerous studies have attempted to gain a better understanding of CBL turbulence and its implications for weather, climate, and numerical weather prediction.

The CBL can be divided into three different layers – the surface layer (SL), the mixed layer (ML), and the entrainment zone (EZ), the last of which represents the transition zone between the CBL and the FA (Figure 1.1). The characteristics of the CBL have been examined over flat homogeneous terrain for several decades. Previous works have often used turbulent kinetic energy (TKE) and associated budget terms to describe the evolution of turbulent mixing and development of the CBL over flat terrain. TKE terms frequently calculated include buoyant production/destruction, mechanical production, and dissipation of turbulence.

Results from the 1968 Kansas Surface Layer and 1973 Minnesota Boundary Layer

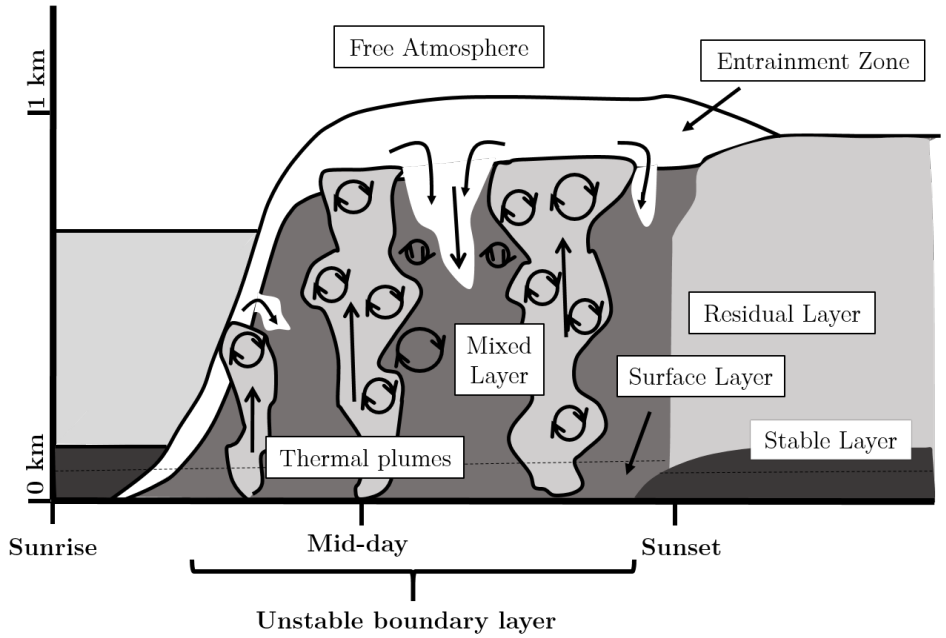

FIGURE 1.1: Schematic of fair-weather atmospheric boundary layer structure over flat terrain (adapted from Stull (1988))

Experiments have provided the general structure of CBL turbulence during quiescent fair weather and convective conditions over flat homogeneous terrain (e.g. Wyngaard and Coté 1971; Kaimal et al. 1976; Caughey and Palmer 1979). A summary of the structure of TKE and associated budget terms through the unstable boundary layer is given in Figure 1.2. These studies suggest that the evolution of the boundary layer is driven by the rising and mixing of warm thermals from the unstable surface layer. Although this layer is relatively thin, being on the order of tens of meters thick, it provides the turbulent input that drives the developing CBL. Buoyant production of turbulence by surface heating and shear production due to wind shear near the surface aid in the production of TKE in this layer. The production of turbulence in the surface layer is balanced by the vertical transport of TKE into the mixed layer. Shear production of TKE decreases sharply above the surface layer, and buoyant production of turbulence drives turbulent mixing in the mixed layer. Dissipation is relatively constant with respect to height and proportional to the production of TKE. In the upper half of the CBL, buoyancy production decreases nearly linearly and becomes negative near the entrainment zone. The vertical transport of TKE increases almost linearly with height in the mixed layer

and becomes maximum near the CBL top. Through the mixed layer, TKE decreases and becomes negligible above the CBL top and in the entrainment zone. While knowledge of the TKE budget terms in the surface and mixed layer is quite complete, and theories about them are well developed, the entrainment zone has received much less attention (Moeng and Sullivan 1994).

Since a solely unstable boundary layer rarely exists in nature, past investigations have found that the structure of the TKE budget terms can be altered depending on the flow strength and amount of shear present at the surface and the top of the CBL. In a purely shear-driven boundary layer, Moeng and Sullivan (1994) found that shear dominated the production of TKE from the surface layer through the middle part of the boundary layer. Dissipation was proportional to shear production, and buoyancy production was negligible in the shear driven boundary layer. When the boundary layer is characterized by both buoyancy and shear-driven processes, Moeng and Sullivan (1994) found that the contribution of shear and buoyancy was nearly equal from the surface layer through the mid part of the CBL. However, they note that shear production was likely underestimated since shear near the CBL top was not taken into account.

Other investigations have attempted to distinguish the effects a shear-driven layer atop a CBL has on the vertical variability of the TKE budget terms (e.g. Fedorovich and Conzemius 2008; Pino and Vilà-Guerau De Arellano 2008; Conzemius and Fedorovich 2006a; Conzemius and Fedorovich 2006b). These investigations found that when shear exists near the CBL top the CBL develops a two-layered structure. The two-layered structure is characterized by a shear-driven upper CBL and a buoyantly driven lower CBL. Near the CBL top, entrainment is enhanced by the shear, causing higher momentum FA air to be transported downward. This process increases shear production in the upper part of the CBL. Depending on the strength of the entrainment and mixing within the mid-CBL, shear production of TKE can also be increased in the mid part of the CBL.

Over complex topography, terrain and heterogeneous surface characteristics can significantly influence the dynamical and thermodynamical mechanisms important for TKE generation. The complexity of the terrain and various phenomena that occur in mountainous regions make investigating the structure and development of TKE challenging.

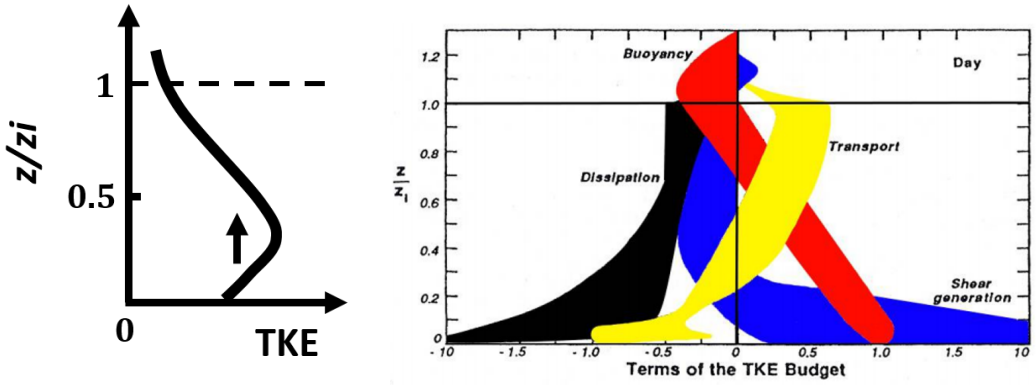

(a) TKE profile (b) TKE budget terms

FIGURE 1.2: a.) Typical vertical profile of TKE (*black arrow* represents the transport of TKE from the surface layer into the mixed layer) and b.) normalized TKE budget terms in an unstable boundary layer over flat homogeneous terrain . The shaded area represents the range of values determined from modeling and observational studies. All terms are divided by w^{*3}/zi, which is on the order of 6×10^{-3} m^2 s^{-3} (adapted from Stull (1988))

We know little of the boundary layer over truly inhomogeneous terrain such as mountains. Additional factors must be considered such as thermally driven mountain wind systems and topographically forced flows induced by terrain features. These processes often dictate the location and development of turbulent regions that would otherwise be non-existent over flat topography.

Some examples of terrain-driven flows include slope-valley flows, lee side eddies, flow separation, wakes, and vortices. Whiteman (1990) and Banta (1984) have described the classical representation of terrain driven flow systems that are important for influencing the boundary layer structure. In general, these mountain wind systems include slope and valley flows. These flows form in response to pressure differences created by the heating of the mountain slopes and valley during the daytime and play an important role in transporting heat, moisture, and momentum in the boundary layer (Kossmann et al. 1998). It is common for these mountain flows to interact and create localized regions of increased turbulent transport. The upward heat flux and mass transport associated with the interaction of terrain flows are important mechanisms for turbulence production in the boundary layer over mountainous terrain (Kirshbaum and Wang 2014; Kirshbaum 2013; Kossmann et al. 1998; Banta 1984).

The effects of airflow over mountain barriers are also of relevant concern for influencing turbulence over complex topography. The development and conditions necessary for mountain waves and turbulent plumes over topography are summarized by Corby (1954) and Scorer (1953). Generally speaking, the wind must be within 30° normal to a mountain ridge and > 7 m s^{-1} at mountain top level. The atmosphere must also be stably stratified, with a stable layer above and below mountain top. Other studies (e.g. Houghton and Kasahara 1968; Baines 1987; Hunt and Snyder 1980) have described the formation of stationary eddies, hydraulic jumps, mountain waves, and wave breaking regions on the lee side of mountains. All of these phenomena have been noted for having a significant influence on turbulent transport within and above the boundary layer.

The interaction between topographically forced flows and thermally driven flows is also a possibility. Banta (1984) describes a convergence zone as the interaction of upslope flows and the mean flow over a mountain ridge. These convergence zones are suggested to influence the turbulent transport of heat and momentum over topography.

Various methods exist to investigate the boundary layer turbulence structure over mountainous terrain. The most effective approaches include the use of *in-situ* aircraft and supporting ground-based observations. Aircraft observations over mountainous terrain have the capability to reveal the presence of two-dimensional features, which are otherwise impossible with just fixed point measurements. Additionally, aircraft expand observations over greater depth and spatial area within the boundary layer (Lothon et al. 2003). A few studies have addressed the TKE structure over mountainous terrain with aircraft (Karacostas and Marwitz 1980; Hahn 1980; Lothon et al. 2003; Jiang and Doyle 2004; Rotach and Zardi 2007; Weigel et al. 2007b; Jiang et al. 2010).

During conditions when the mean flow is moderate to strong (> 10 m s^{-1}) near mountain top level, the generation of TKE is highly influenced by stationary eddies, hydraulic jumps, mountain waves, and wave breaking regions on the lee side of mountains (Kirshbaum and Wang 2014; Jiang et al. 2010; Jiang and Doyle 2004; Lothon et al. 2003; Attié et al. 1997; Karacostas and Marwitz 1980; Hahn 1980). These flow features create turbulent areas characterized by a TKE maximum on the lee side, which can extend 10-15 km downwind of a mountain (Lothon et al. 2003; Attié et al. 1997; Karacostas and Marwitz 1980; Hahn 1980). The TKE maxima generated by these flow features are

a product of shear instability and increased momentum transport due to the dynamical interaction of the mean flow and underlying terrain. In such scenarios, shear production of turbulence is the main mechanism of TKE production.

Relatively fewer studies have investigated the turbulence structure over mountainous terrain in a CBL with weak winds (< 10 m s^{-1}). The turbulence in the CBL over complex topography can be affected by the convergence of thermally driven terrain flows and thermal forcings created by heating of the surface (Kirshbaum and Wang 2014; Kirshbaum 2013). However, unlike TKE over flat homogeneous terrain in unstable conditions, TKE in mountainous terrain can be generated through mechanical rather than buoyant forces (Weigel et al. 2007b; Hahn 1980; Lenschow et al. 1979). This is because air above mountain ridge tops becomes well-mixed earlier than air in adjacent valley due to its higher potential temperature. Higher momentum air from aloft can then mix down near the ridge tops and aid in turbulence production (Banta 1984; Hahn 1980; Lenschow et al. 1979). Frequently, these effects of terrain on the development of turbulence can extend to a significant vertical depth into and above the CBL (Hahn 1980).

At present, many numerical models do not account for the effects of the aforementioned terrain driven processes on the variability of boundary layer turbulence. An understanding of these effects and the spatial variability of turbulence is imperative for the improvement of model parameterizations and numerical weather prediction over complex topography. This study is motivated by the need for an improved understanding of the variability of turbulence in a mountain boundary layer. Many previous investigations have shown that TKE within the CBL is significantly influenced by topography. However, the complex interactions in regions with multiple ridges and valleys make it challenging to identify the processes responsible for the spatial variations in the TKE structure. The presence of an isolated mountain surrounded by flat terrain provides an opportunity to simplify the investigation of boundary layer processes over mountainous terrain in a daytime CBL.

In this contribution, we attempt to fill this gap in knowledge by utilizing the Mountain Terrain Atmospheric Observations and Modeling Experiment (MATERHORN) airborne and surface based dataset. The overarching goal of the MATERHORN project is

motivated by the need to improve our knowledge of how mountainous terrain and associated dynamical and thermodynamical processes influence the boundary layer structure. The data used in this thesis is from *in-situ* high-frequency meteorological aircraft data, Doppler wind lidar, and surface meteorological observations collected by a Navy Twin Otter (TO) during the MATERHORN-X experiment (Fernando et al. 2015). The available airborne observations used for analysis were obtained over and around the isolated mountain Granite Peak, Utah (10 x 1 km) during daytime CBL conditions. The *in-situ* and Twin Otter Doppler Wind LiDAR (TODWL) measurements are available from seven flights on six days in October 2012.

The primary goal of this thesis is to investigate the location of TKE maxima and associated generation mechanisms over and around the isolated mountain, Granite Peak. This goal is divided into two parts. In the first part of this thesis, the objectives are to determine the location of TKE maxima and to distinguish how/if ambient flow, stability, and terrain influence the location of the TKE maxima over Granite Peak. The second part of this thesis aims to identify the mechanisms and processes responsible for the generation of the observed TKE field and TKE maxima. This investigation is completed by using *in-situ* airborne observations to calculate the TKE budget terms of shear production, buoyant production/destruction, and dissipation.

This research will be beneficial to both public and scientific communities. Accurate knowledge of the location and mechanisms that generate TKE maxima over complex topography is of particular importance for increasing aviation safety, understanding the mixing and transport of dust and pollutants, and convection and cloud formation. In addition, this knowledge has potential to provide verification of models and improve the mesoscale and local scale representation of CBL processes in complex terrain. In Chapter 2, the investigation of the location of TKE maxima and influence from ambient flow and stability is given. Chapter 3 provides the investigation of the generation mechanisms processes important for TKE maxima using the TKE budget equation. Last, Chapter 4 includes summary and conclusions.

Chapter 2

Location of TKE maxima

Abstract

The evaluation and development of boundary-layer parameterizations require observations and an understanding of turbulence that is particularly limited in mountainous terrain. The objective of this study is to investigate the spatial variability of turbulence kinetic energy (TKE) in the convective boundary layer over an isolated mountain ridge with a focus on the location of TKE maxima. The study uses airborne *in-situ* meteorological and Doppler wind lidar observations from the first field experiment of The Mountain Terrain Atmospheric Modeling and Observations (MATERHORN) Program at Dugway Proving Ground (Utah, USA) in Fall 2012. The airborne observations were made during seven flights over the steep isolated mountain, Granite Peak, of a horizontal and vertical scale of about 10 km and 1 km, respectively. The seven flights took place during three mornings and four afternoons with boundary layers up to 1000 m deep and near-surface winds up to 5 m s^{-1}. Regions with enhanced TKE (maximum values of 1.5-2.5 m^2 s^{-2}) are found over the mountain crest of Granite Peak, over small ridges along the eastern side of the mountain, and in the center and exit of a terrain gap to the south of Granite Peak. These regions are characterized by the presence of dynamically and thermally induced features such as breaking waves and organized convective plumes, respectively. Areas of large TKE are apparent near and above the CBL top. The vertical variability of TKE is contrary to the traditional vertical TKE profile over flat and homogeneous terrain, where TKE becomes negligible near and above the CBL top. A mountain-induced effect on turbulence characteristics in and above the CBL extends approximately 5-10 km downwind and 2.5-5 km upwind of Granite Peak.

2.1 Introduction

Observations of turbulence in the atmospheric boundary layer are essential for the evaluation and development of turbulence parameterizations. Current parameterizations assume flat and homogeneous topography which are not expected to represent certain characteristics of turbulence (e.g. spatial-temporal evolution) over complex terrain (e.g. Rotach and Zardi 2007; Weigel et al. 2007b). Consequently, there are large uncertainties in the application of turbulence parameterizations over complex terrain.

Turbulence in the convective boundary layer (CBL) over flat and homogeneous terrain has been examined for several decades and is well-understood (e.g. Wyngaard and Coté 1971; Kaimal et al. 1976; Caughey and Palmer 1979). The turbulent kinetic energy (TKE) and associated budget terms are typically used to quantify turbulence and the processes that generate and destroy turbulence (e.g. Wyngaard and Coté 1971; Kaimal et al. 1972; Kaimal et al. 1976; Kaimal and Wyngaard 1990). These studies show maximum TKE values near the surface, a general decrease with height in the CBL, and a strong decrease at the top of the CBL above which TKE is close to zero. The rising and mixing of warm thermals and wind shear near the surface drive the production of TKE and the evolution of the CBL. Above the surface layer, TKE is transported vertically within the mixed layer.

Several studies have addressed TKE observations of the boundary layer over complex terrain (Orlanski 1975; Karacostas and Marwitz 1980; Hahn 1980; Bougeault and Lacarrere 1989; Lothon et al. 2003; Rotach and Zardi 2007; Weigel et al. 2007b; Jiang et al. 2010; Wulfmeyer et al. 2011). These studies have demonstrated the important effects of mountainous terrain on TKE in neutral, stable, and unstable conditions (e.g. Jiang et al. 2010; Weigel et al. 2007b; Lothon et al. 2003; Karacostas and Marwitz 1980; Hahn 1980). Results from these observational studies show that thermally-driven flows (e.g. slope and valley flows) and terrain driven flows (e.g. flows associated with hydraulic jumps, wakes, and waves) govern boundary layer turbulence by affecting the turbulence production mechanisms and the transport of heat, moisture, and momentum. TKE maxima have been documented over and downwind of small ridge tops, mountain crests, and adjacent to valley sidewalls in neutral boundary layers with moderate winds

and unstable boundary layers with weak winds (e.g. Karacostas and Marwitz 1980; Hahn 1980; Weigel et al. 2007b; Lothon et al. 2003).

Hahn (1980) found that when winds at low levels in the CBL were weak, TKE increased in localized buoyant plumes associated with an isolated ridge and organized thermally driven upslope winds along the Front Range of the Rocky Mountains. These flow characteristics created TKE maxima ($\approx 1-2$ m^2 s^{-2}) in a CBL above a small steep ridge in the lee of a larger north-south oriented mountain range. At upper levels in the boundary layer, a TKE maximum was found of about 2-4 m^2 s^{-2} 1-5 km downwind of a large mountain crest (elevation $\approx$ 4200 m MSL; ridgetop height $\approx$ 1300 m). This TKE maximum was attributed to a wave breaking region caused by the interaction of the cross mountain flow and the mountain crest. Weigel et al. (2007b) showed that in an alpine valley with a valley floor width of 1.5 km and valley depth of 2–2.5 km, the shear generated by the interaction of thermally driven valley winds and terrain features produced maximum TKE above the surface layer and adjacent to valley side walls. The terrain flow interaction produced a vertical TKE profile with a secondary peak in TKE above the surface layer, which is different from what has been observed over flat and homogeneous terrain. Karacostas and Marwitz (1980) used aircraft to measure TKE over the isolated Elk Mountain, WY in a neutral boundary layer. They found a hydraulic jump that produced a TKE maximum that extended 10 km downwind of Elk Mountain. The largest values of TKE (5 m^2 s^{-2}) over and downwind of mountain crests occurred during conditions with strong low level winds ($>$ 10 m s^{-1}) (Karacostas and Marwitz 1980; Lothon et al. 2003; Jiang et al. 2010). However, significant TKE maxima (1.5-4 m^2 s^{-2}) have also been observed near mountain crests during conditions with moderate winds at or above mountaintop and weak winds at low levels ($<$ 5 m s^{-1}).

TKE within the CBL is clearly influenced by topography, but the complex interactions in settings with multiple ridges and valleys make it challenging to identify the processes responsible for the spatial variability of TKE. The presence of an isolated mountain surrounded by flat terrain provides an opportunity to simplify the investigation of boundary layer processes over mountainous terrain. While some previous studies examined daytime CBL processes over an isolated mountain, these studies did not make observations of the spatial variability of TKE (e.g. Demko and Geerts 2010; Raymond

and Wilkening 1982). The main objectives of this study are to 1) investigate the location and magnitude of TKE maxima in the CBL over and around an isolated mountain and 2) explore how the location and magnitude of TKE maxima depend on the lower-level ambient flow speed and direction, and on boundary layer stability.

To address these objectives, we use aircraft based turbulence data and airborne Doppler wind lidar data collected during the first Mountain Terrain Atmospheric Observations and Modeling Experiment (MATERHORN-X; Fernando et al. 2015). The airborne measurements includes a broad array of high-frequency (up to 10 Hz) meteorological *in-situ* and Doppler wind Lidar observations collected by a Navy Twin Otter research aircraft that flew multiple flight legs over an isolated mountain, Granite Peak, and surrounding heterogeneous terrain. The *in-situ* and Twin Otter Doppler Wind Lidar (TODWL) measurements are available from seven flights on five days in October 2012. The airborne *in-situ* and TODWL datasets, combined with surface-based observations, are capable of illustrating the interactions between turbulence, terrain driven wind systems, and CBL structure over complex terrain on a spatial scale of about 50 km x 50 km.

The remainder of the paper is organized as follows: Section 2.2 provides details of the MATERHORN-X field campaign, aircraft flights, observational data, and turbulence analysis used in this study. In this section, several methods are used to define the appropriate turbulence averaging method and length scale for the estimation of TKE from aircraft observations. Section 2.3 presents the results of the analysis of TKE during the seven flight periods in the study. In addition, a conceptual discussion of the location of TKE maxima over and around Granite Peak related to observed thermodynamical and dynamical processes is given. Last, Section 2.4 provides summary and conclusions from this study.

2.2 Experimental data set

2.2.1 Experimental area

Measurements used in this study were collected during the MATERHORN campaign in the Fall of 2012 (MATERHORN-X; Fernando et al. 2015). MATERHORN-X consisted

of nine intensive observation periods (IOPs) that took place around the isolated Granite Peak, Utah, Dugway Proving Ground, (elevation ≈ 2159 m MSL; length ≈ 10 km; base width ≈ 1.5 km; ridgetop height ≈ 800-900 m). The immediate area surrounding Granite Peak is characterized by relatively flat terrain (≈ 1300 m MSL) that is gently increasing in height towards the south (Fig. 2.1).

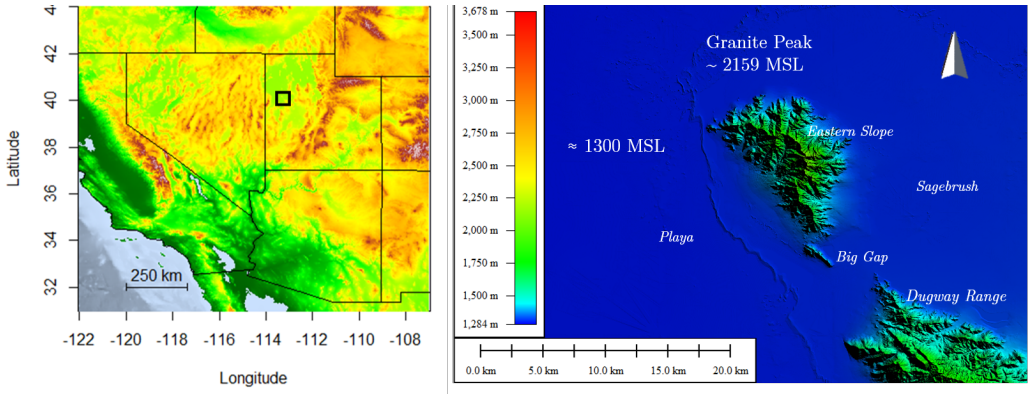

FIGURE 2.1: **Left:** *Black box* denotes the location of the experimental area in northwestern Utah, US. **Right:** Topography of Granite Peak (centered), the Dugway Range, and the surrounding region.

Flow patterns and boundary layer processes are expected to be related to various topographical and surface features in the investigation area including 1) Granite Peak, 2) a 5 km long 1 km wide terrain gap ("big Gap") between Granite Peak and a mountain range (Dugway Range) to the south, 3) the relatively flat and desert shrub region (Sagebrush) to the east of Granite Peak, 4) the small ridge tops associated with small tributary valleys along the eastern slope of the mountain (Eastern Slope), and 5) the barren but relatively moist salt-sand flat (Playa) to the west of Granite Peak (Fig. 2.1). The Playa consists of a thin layer of salt-sand crust sitting atop the relatively moist silt-sand soil. The difference in surface characteristics between the western and eastern side of Granite Peak is an important feature affecting the overlying CBL, which will be described in more detail in Section 3. It is also important to note that a small mountain (Sapphire Mountain) is located between Granite Peak and a mountain range to the south (Dugway Range).

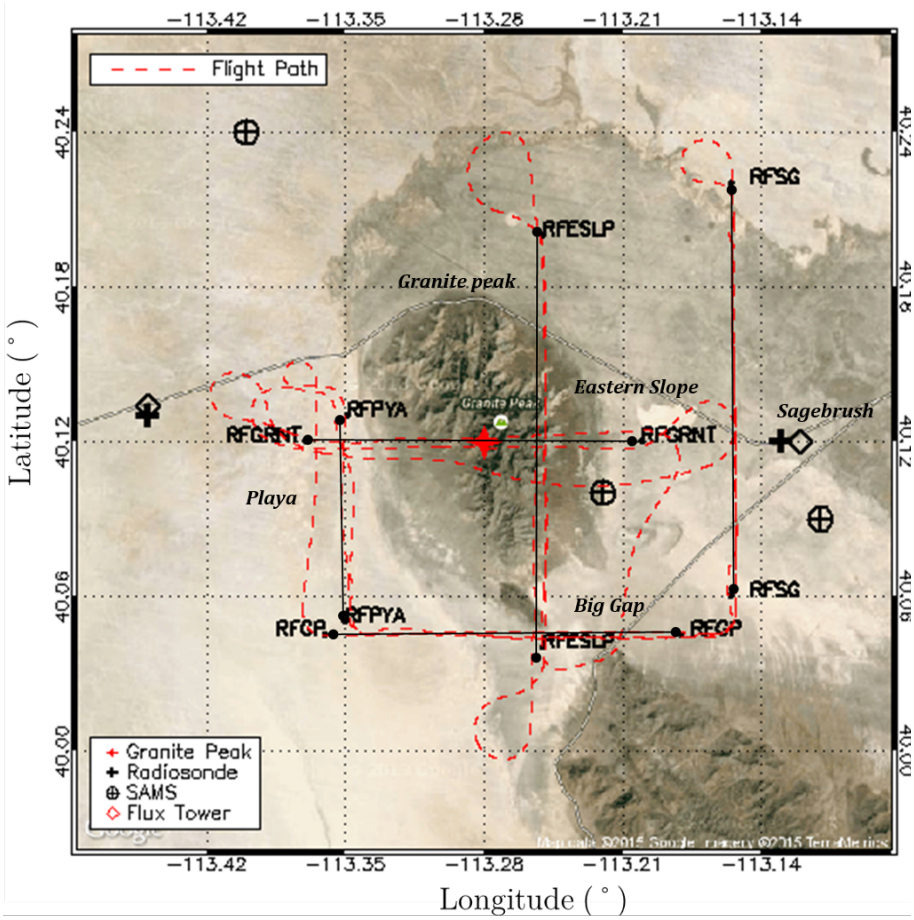

FIGURE 2.2: Geographical overview of the experimental area and location of selected observations. Red dotted lines represent the aircraft flight path on 9 October 2012. Granite Peak and the following five regions are referred to in the main text: Playa, Big Gap, Eastern Slope, and Sagebrush regions, which are to the west, south, immediately east, and east of Granite Peak, respectively. Black solid lines represent the approximate location of research flights (RF) during the seven flight periods used for analysis: Sagebrush (RFSG), Gap (RFGP), Playa (RFPYA), Granite Peak (RFGRNT), and Eastern Slope (RFESLP). The location of surface automated meteorological stations (SAMS; circle with cross), radiosondes (black cross), and flux towers (black triangle) are provided

2.2.2 Observational data set

An overview of the geographical location of observational platforms and aircraft flight legs used in this study is given in Fig. 2.2. Data are used from airborne *in-situ* meteorological measurements collected from a Navy Twin Otter (TO) research aircraft that flew multiple flight legs over Granite Peak and surrounding terrain. These *in-situ* airborne measurements are available from seven flights on five days in October 2012. The average aircraft speed was 50 m s^{-1} and aircraft in-situ measurements were sampled at

10 Hz. *In-situ* 10 Hz measurements include horizontal and vertical wind velocity components (u, v, and w), potential temperature (θ), and specific humidity (q). In addition, TODWL wind profiles were obtained at a vertical resolution of 50 m from about 200 m AGL to 2200 m AGL) and a horizontal resolution of about 1500 m to investigate the effects of Granite Peak on the mean flow patterns. Details about the instruments on-board the TO are given in appendix A.

The investigation in the current study focuses on *in-situ* observations from multiple north-south and east-west oriented flight legs over the five main regions (Fig. 2.2). These flight legs include "turbulence flights", where the TO was flown in straight-and-level legs between 1500 m to 3000 MSL and ranged in length from 7 to 20 km. The majority of these flight legs were flown within the CBL and slightly above the CBL height (z_i). To assist in the interpretation of the turbulence structure, a selection of TODWL wind profiles are also used. TODWL flight legs were at a constant altitude of 3500 m MSL and ranged in length from 20 to 30 km.

Flight legs for the turbulence analysis were selected using criteria, which require the flight legs to have ample length (>10 km) and a relatively constant flight altitude (m MSL) and heading (Foken and Wichura 1996; Vickers and Mahrt 1997; Mahrt 1998). The purpose of the flight leg criteria is to reduce uncertainty in the turbulence calculations. Post-flight data quality control steps included the application of a standard deviation filter to the raw data as described by Mahrt (1998). Above 3σ, observations were considered outliers and were removed from further analyses.

Surface-based observations at the time of the flights include radiosonde and tower measurements. Radiosondes were launched roughly every three hours during IOPs and were from two sites, the Playa and Sagebrush, located on the western and eastern side of Granite Peak, respectively. Tower observations were from three surface automated meteorological stations (SAMS) over the Sagebrush, Playa, and Eastern Slope and two flux towers over the Sagebrush and Playa (Fig. 2.2). Measurements from SAMS towers include 5 min averaged wind speed, wind direction, temperature, pressure, incoming solar radiation, and humidity measured at 10 m. Flux tower measurements include 15 min averaged sensible heat flux (H).

TABLE 2.1: Flight times of TODWL and *in-situ* flights given for each flight period. Average *zi* over the Sagebrush during each flight period is given.

Flight period	**Time (MST): TODWL**	**Time (MST): *in-situ***	***zi* (m MSL)**
06Oct_{PM}	$1515 - 1635$	$1640 - 1741$	2100
07Oct_{AM}	$1030 - 1200$	$1204 - 1309$	1900
09Oct_{PM}	$1605 - 1727$	$1731 - 1900$	2200
10Oct_{AM}	$1015 - 1145$	$1151 - 1318$	1600
14Oct_{AM}	$0924 - 1118$	$1124 - 1218$	1800
14Oct_{PM}	$1506 - 1645$	$1650 - 1800$	2000
17Oct_{PM}	$1400 - 1545$	$1551 - 1700$	1750

2.2.3 Flight periods

In this study, we investigate the spatial variability of turbulence from all four IOPs with TO research flights: IOP 4: 6-7 October, IOP 5: 9-10 October, IOP 6: 14 October, and IOP 7: 17 October 2012. During the four IOPs, the seven different flight periods were the afternoon of 06 October (06Oct_{PM}), the morning of 07 October (07Oct_{AM}), the afternoon of 09 October (09Oct_{PM}), the morning of 10 October (10Oct_{AM}), the morning of 14 October (14Oct_{AM}), the afternoon of 14 October (14Oct_{PM}), and the afternoon of 17 October (17Oct_{PM}). Each of the flight periods was chosen based on the criteria that quiescent, dry, fair weather (700 mb wind < 5 m s^{-1}) periods dominated (Fernando et al. 2015). However, lower and upper-level winds, as well as stability, differed. Flight periods contained upper-level (3500 m MSL) TODWL flight legs and lower level (1600-3000 m MSL) *in-situ* turbulence flight legs. Each of the flight periods lasted 3-4 hours.

The flight times of TODWL and turbulence flight legs during each IOP are given in Table 2.1. The ambient flow conditions and CBL structure during each flight period are summarized using radiosonde, airborne *in-situ*, and TODWL (Table 2.2). The prevailing synoptic conditions during each flight period are given in appendix B. Under typical fair weather conditions in the investigation area, thermally driven flows are from a northerly direction during the afternoon, changing towards southerly directions at night. During the 06Oct_{PM} period, near surface winds were northerly and weak at 3-4 m s^{-1}. The upper-level flow was characterized by moderate northwesterly winds (> 5 m s^{-1}) above

TABLE 2.2: Ambient conditions during the flight periods including the upper-level (UL) wind speed (2000-3000 m MSL), upper-level wind direction, CBL (lower-level) wind speed (1300-*zi* m MSL), CBL (lower-level) wind direction, surface sensible heat flux (H), and wind class for each flight period.

Flight period	**UL ws (m s^{-1})**	**UL wd**	**CBL ws (m s^{-1})**	**CBL wd**	**H (W m^{-2})**	**Wind class**
06Oct$_{\mathrm{PM}}$	$5-10$	300°	$3-4$	330°	120	Moderate
07Oct$_{\mathrm{AM}}$	<5	330°	$3-5$	300°	120	Quiescent
09Oct$_{\mathrm{PM}}$	<5	190°	$2-3$	340°	<10	Quiescent
10Oct$_{\mathrm{AM}}$	$5-8$	200°	$4-7$	190°	90-100	Transitional-moderate
14Oct$_{\mathrm{AM}}$	<5	300°	$2-4$	140°	80-90	Quiescent
14Oct$_{\mathrm{PM}}$	<5	300°	$2-4$	140°	50-75	Quiescent
17Oct$_{\mathrm{PM}}$	$5-15$	305°	$2-4$	340°	90-100	Transitional-moderate

2500 m MSL. 07Oct$_{\mathrm{AM}}$ was a morning flight period with northerly near surface flow 3-5 m s^{-1}. Similar to 06Oct$_{\mathrm{PM}}$, upper-level flow was northwesterly and moderate. During the 09Oct$_{\mathrm{PM}}$ period, weak near surface flow 2-3 m s^{-1} and upper level flow <5 m s^{-1} existed, with the wind direction changing from northerly diurnal/thermally driven flow near the surface to southwesterly flows in the upper levels. The surface flow during the 10Oct$_{\mathrm{AM}}$ period was weak (2-3 m s^{-1}) and south-southwesterly. However, within and above the boundary layer the wind speed increased to 8-10 m s^{-1} at 2000-3000 m MSL and decreased slightly above this layer. Flows during the 14Oct$_{\mathrm{AM}}$ and 14Oct$_{\mathrm{PM}}$ periods were relatively weak (2-4 m s^{-1}) and south-southeasterly at lower levels, while at upper levels they were southwesterly and weak (<5 m s^{-1}). On 17Oct$_{\mathrm{PM}}$, the flow was northerly at 2-4 m s^{-1} below 2000 m MSL. Above this height the wind speed increased to >10 m s^{-1}, which was the largest observed wind speed above the CBL of all the flight periods.

During the flight periods of 06Oct$_{\mathrm{PM}}$, 09Oct$_{\mathrm{PM}}$, and 14Oct$_{\mathrm{PM}}$, CBL depths of up to 1 km AGL were observed from radiosonde data from the Playa and Sagebrush sites (not shown). On each of these days, average z_i ranged from 2000-2200 m MSL (800-1000 m AGL) over the Sagebrush and 1800-2000 m MSL (500-800 m AGL) over the Playa. The difference in *zi* between the Sagebrush and Playa is attributed to differences in surface

characteristics and thus differences in the surface energy budget and forcings between the regions. The *zi* observed during morning flight periods of 07Oct_{AM}, 10Oct_{AM}, 14Oct_{AM} and the afternoon flight 17Oct_{PM} were relatively shallow. The average *zi* during these flight periods ranged from 1600-1900 m MSL (300-600 m AGL) over the Sagebrush and 1500-1800 m MSL (200-500 m AGL) over the Playa.

2.2.4 Turbulence averaging length for TKE calculation

Many previous studies have shown that spectral analysis is a useful tool for determining the spectral energy gap and thus turbulence averaging length of a time series (Lothon et al. 2003; Jiang et al. 2010). Spectral analysis was performed using the Fast Fourier Transform (FFT) method to identify the dominant scales and energy gap in the longitudinal and vertical wind components. This information was then used to determine a turbulence averaging length to estimate TKE. Spectral analysis was completed using linearly de-trended 10 Hz aircraft data. After applying FFT, spectra were averaged over equal intervals of 2048 data points (205 s) using 50% overlap and a Nyquist frequency of 5 Hz.

The variation of spectral densities of the horizontal and vertical wind components was compared across flight regions and flight periods. There are multiple peaks in the spectra between 500 and 1500 m in u, v and w, and the existence of an energy gap is not obvious. Arguably, the energy gap in the u and v components is between 400 and 1500 m and in the w component between 300 and 1500 m. These peaks in the spectra indicate the presence of larger scale motions contributing to the variance, which should not be included in turbulence calculations. Therefore, based on the spectra, 500 m would be the suitable averaging length for TKE calculation (where $e = 0.5(u'^2 + v'^2 + w'^2)$). Other methods exist to determine an appropriate averaging length, including the sensitivity test to the length of moving average as discussed by Večenaj et al. (2012). In this procedure, turbulent perturbations of the three wind velocity components (w', u', and v') are calculated by subtracting moving averages of varying lengths from the *in-situ* aircraft measurements (Lenschow and Stankov 1986; Foken and Wichura 1996; Večenaj et al. 2012). Moving averages 500, 1000, and 1500 m long are used to test the dependence of the spatial variability and magnitude of TKE on averaging length. The sensitivity tests

show that the shape and spatial distribution of TKE are largely conserved regardless of moving averaging length. The moving average method confirms that an averaging length of 500 m (10 s of flying at 50 m s^{-1}) is appropriate for this study.

2.3 Results and discussion

2.3.1 Influence of terrain, ambient flow, and stability on TKE

In this section, we describe the TKE variability across flight legs over the Sagebrush, Eastern Slope, Gap, Playa, and Granite Peak. While the results are presented as an instantaneous snapshot of the TKE variability, it should be recognized that the flight legs are separated in time by as much as 15-20 minutes. Furthermore, the flight legs over a region are not exactly in vertical alignment. Instead, flight legs may be offset vertically by as much as 0.5-1 km in some instances. These considerations need to be taken into account when interpreting the results presented below. In our discussion of the results, we focus on the location of TKE maxima over the flight regions related to the influence of terrain, ambient flow, and boundary layer stability.

TKE magnitudes during the $09Oct_{PM}$ and the $14Oct_{AM}$ and $14Oct_{PM}$ flight periods were considerably smaller than during the other flight periods. The $09Oct_{PM}$ flights took place during the transition from a CBL to a stable nocturnal boundary layer (sunset 1731 MST) between 1730 and 1900 MST when surface sensible heat fluxes became negative (Table 2). As a result, CBL turbulence decayed, resulting in the small values of TKE ($<$ 0.5 m^2 s^{-2}). During the $14Oct_{AM}$ and $14Oct_{PM}$ flights, the surface heat forcing is lower than during the other flight periods due to a frontal passage and associated precipitation event that occurred two days prior (Table 2). The small surface sensible heat flux (50-90 W m^{-2}) compared to the other days (90-150 W m^{-2}) along with weak flow (2-3 m s^{-1}) produced weak buoyant and mechanical forcings resulting in small TKE values ($<$ 0.5 m^2 s^{-2}) (Fig. 2.3e and 2.3f). In the following sections, we focus our discussion of TKE maxima during the periods that have significant surface forcings and/or relatively strong flow. These periods include $06Oct_{PM}$, $07Oct_{AM}$, $10Oct_{AM}$, and $17Oct_{PM}$.

2.3.2 Eastern Slope

Eastern Slope flight legs used for analysis were flown in the north-south direction over the eastern slope of Granite Peak. During the $06Oct_{PM}$, $07Oct_{AM}$, $10Oct_{AM}$, and $17Oct_{PM}$ flight periods, maximum TKE values ranged between 1 and 2.5 m^2 s^{-2} over the Eastern Slope with some well-defined local maxima in TKE. These maxima are associated with ridge lines corresponding to small tributary valleys along the Eastern slope. The largest values of TKE over the Eastern Slope occur during the $10Oct_{AM}$ flight (> 1.5 m^2 s^{-2}) (Fig. 2.3d). In particular, two local TKE maxima (> 2.0 m^2 s^{-2}) in the wake of a small ridge (40.14° N) are evident at the mid and upper flights, while at the lower most flight level, very high spatial variability in TKE is observed most likely due to the underlying orography. The TKE field during $06Oct_{PM}$ and $07Oct_{AM}$ also exhibits local maxima (1-1.5 m^2 s^{-2}) at lower and mid-flight levels that correspond to underlying ridge tops at 40.09° N and 40.13° N, respectively (Fig. 2.3a and 2.3b). A local TKE maximum (1.4 m^2 s^{-2}) is also evident to the north of the ridge (40.16° N) during the $06Oct_{PM}$ period. However, unlike $10Oct_{AM}$, TKE is negligible (< 0.05 m^2 s^{-2}) at the $06Oct_{PM}$ and $07Oct_{AM}$ upper flight levels. Relatively large values of TKE are apparent at all flight levels during the $17Oct_{PM}$ period directly over a prominent ridge (Fig. 2.3g) with TKE maxima of ≈ 1.5 m^2 s^{-2}at the mid and uppermost flight levels. A local maximum of 0.60 m^2 s^{-2} is evident along the lower flight level.

During the $10Oct_{AM}$ flight period, surface H was $\approx$ 90-100 W m^{-2} and $z_i \approx$ 1650-1750 m MSL over the Sagebrush. South-southwesterly flow (5-8 m s^{-1}) prevailed at low levels and upper levels (Table 2). The *in-situ* aircraft observations suggest the occurrence of a breaking wave in the stably stratified FA over the slope. As seen in Fig. 2.4, there is a narrow band of sharp variations in vertical velocity (2 to -2.5 m s^{-1}) and potential temperature (309-307 K) north of 40.13°N on the lee side of a small ridge. These variations in the vertical wind component and potential temperature are approximately 180° out of phase, which indicates that this feature is related to a small wave and/or a wave breaking region (Jiang et al. 2010). The phase relations imply negative heat and momentum fluxes. The generation of TKE by shear and negative momentum fluxes is larger than the destruction of TKE due to negative heat fluxes at these locations. Consequently, the wave breaking region is characterized by large values

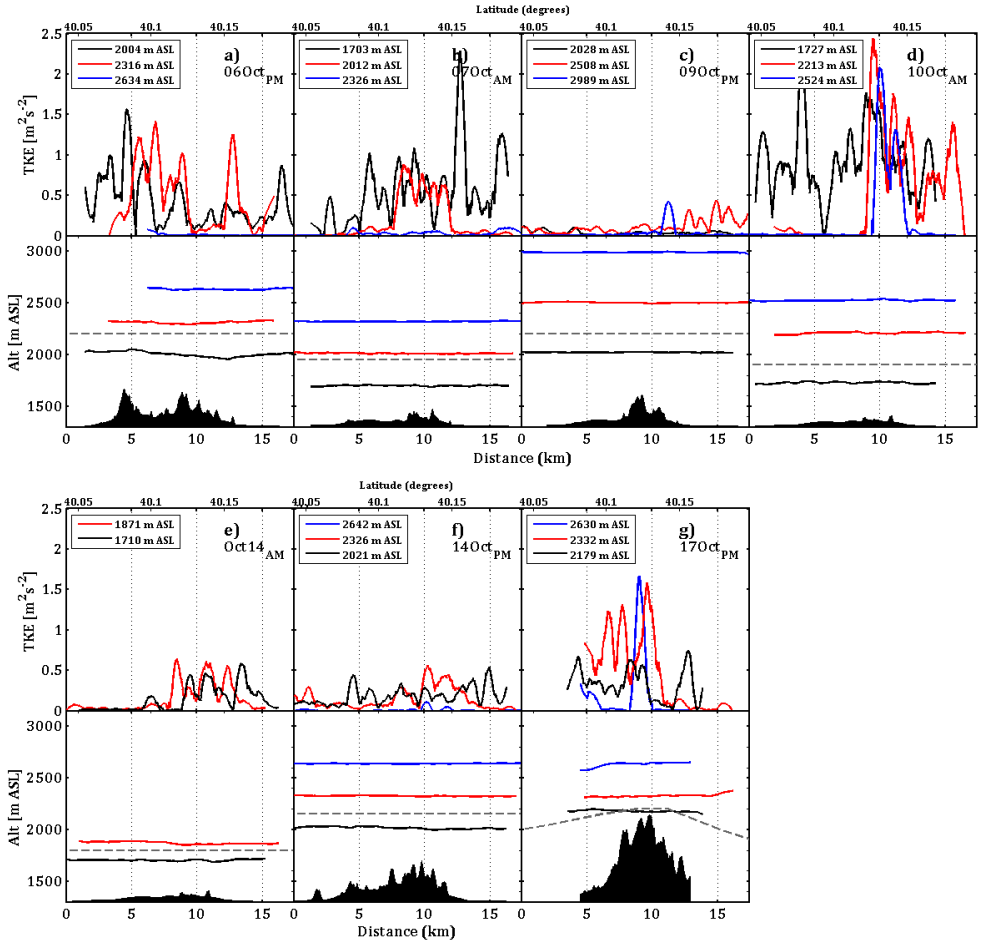

FIGURE 2.3: Top: Turbulent kinetic energy calculated from airborne observations for the Eastern Slope flight legs during the a.) $06Oct_{PM}$, b.) $07Oct_{AM}$, c.) $09Oct_{PM}$, d.) $10Oct_{AM}$, e.) $14Oct_{AM}$, f.) $14Oct_{PM}$, and g.) $17Oct_{PM}$ flight periods. Bottom: Flight legs plotted over elevation profiles of underlying terrain (*black solid line*) Estimated CBL height (*zi*) included (*grey dotted line*).

of TKE (2-2.5 m^2 s^{-2}) that exist well above the estimated *zi* over the Eastern Slope (Fig. 2.3d).

The maximum values of TKE during the $06Oct_{PM}$, $07Oct_{AM}$, and $17Oct_{PM}$ are smaller than during the $10Oct_{AM}$ flight (Fig. 2.3a and 2.3b). We attribute this difference primarily to the weaker lower-level winds during these periods (Table 2). During the $06Oct_{PM}$ period, low-level winds are weakest (2-3 m s^{-1}) and the vertical wind gradients smallest, while surface thermal forcings are relatively large (H > 100 W m^{-2}). *In-situ* airborne observations show localized regions of increased sensible heat fluxes that correspond to the TKE maxima over the ridge tops (40.09° N and 40.11° N) (not shown).

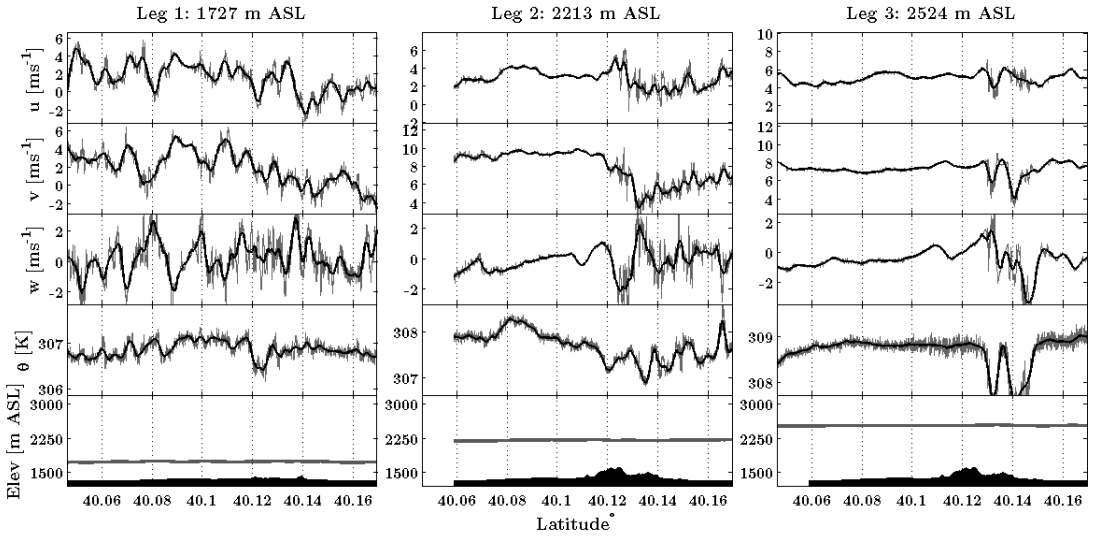

FIGURE 2.4: Airborne *in-situ* observations (w, u, v, and θ) from three flight legs over the Eastern Slope during the 10Oct_{AM} flight period. Solid black line is a 500 m smoothed average. Elevation cross section of underlying terrain is plotted below.

The flow during 07Oct_{AM} is also relatively weak (3-4 m s^{-1}), and no strong forced terrain flows are apparent. Similar to 06Oct_{PM}, increased heat fluxes over ridge tops are observed and correspond with TKE maxima (40.13° N). These buoyant plumes generated over the ridge tops are obviously essential for TKE production in this region. Surface thermal forcings during the 17Oct_{PM} period are also large with H $\approx$ 90-100 W m^{-2}. The flow during this flight period is weak within the CBL (3-4 m s^{-1}), but increases to 7 m s^{-1} from the lower to upper flight level (2100-2600 m MSL). TKE maxima over the ridge top (40.13° N) during the 17Oct_{PM} flight period (Fig. 2.3g) correspond to regions of increased momentum fluxes and heat fluxes (not shown). In summary, there is large variability in the location and magnitude of TKE maxima across the flight periods over the Eastern Slope. However, the location of TKE maxima has some dependence on wind speed and direction. Conditions with relatively strong northerly and southerly flow components produce the largest TKE maxima over the Eastern Slope downwind of ridges.

2.3.3 Granite Peak

East-west flight legs, keeping Granite Peak approximately in the middle, are used for analysis here. The crest of Granite Peak influences the location of turbulent zones. Figure 5 reveals the presence of TKE maxima (0.5-2.5 m^2 s^{-2}) over the slopes and the mountain crest of Granite Peak during all flight periods except during the $09Oct_{PM}$ and $14Oct_{PM}$ periods. In general, TKE decreases an order of magnitude at a distance of 2.5-5 km from the mountain.

During the $06Oct_{PM}$ flight period, the influence of Granite Peak on the location of maximum values of TKE is not as evident as the other flights (Fig. 2.5a). Low level winds during this flight period are relatively weak and north-northwesterly (2-4 m s^{-1}) over Granite Peak. The average decrease of TKE from Granite Peak to the surrounding region is $\approx$ 0.4-0.5 m^2 s^{-2}. There are two TKE maxima ($\approx$ 0.60 m^2 s^{-2}) at the mid-level flight leg associated with two small ridges (113.27° W and 113.29° W). A broad TKE maximum (0.50 m^2 s^{-2}) is apparent at the lower flight directly over the mountain crest. Relatively weak north-northwesterly lower level winds (2-4 m s^{-1}) are also observed during the $07Oct_{AM}$ period. However, larger values of TKE are found over Granite Peak during this period than during the $06Oct_{PM}$ period (Fig. 2.5b). The influence of topography is evident, and the TKE closely follows the shape of the underlying terrain. TKE maxima of 0.75 m^2 s^{-2} exist at the lower and upper flights while a maximum of 1.5 m^2 s^{-2} is apparent at the mid-flight level over the mountain crest (113.27° W).

There are maxima in the TKE field associated with Granite Peak during the $10Oct_{AM}$ period (Fig. 2.5d). During this flight period, there is a TKE maximum (1.0 m^2 s^{-2}) directly over Granite Peak at the lower flight level. A smaller TKE maximum (0.70 m^2 s^{-2} is also apparent at the uppermost flight level (2500 m MSL, approximately 900 m above estimated *zi*). The strongest influence of terrain on the TKE field over Granite Peak is during the $17Oct_{PM}$ period (Fig. 2.5g). TKE maxima $>$ 1.5 m^2 s^{-2} are found at all flight levels directly over the crest of Granite Peak. Moving away from the crest of Granite Peak, the TKE decreases to negligible values at a distance of 5 km east and 2.5 km west from the crest of Granite Peak.

During the $06Oct_{PM}$ flights, localized regions of positively buoyant air generated from two small ridges (113.27° W and 113.29° W) correspond with TKE maxima in the

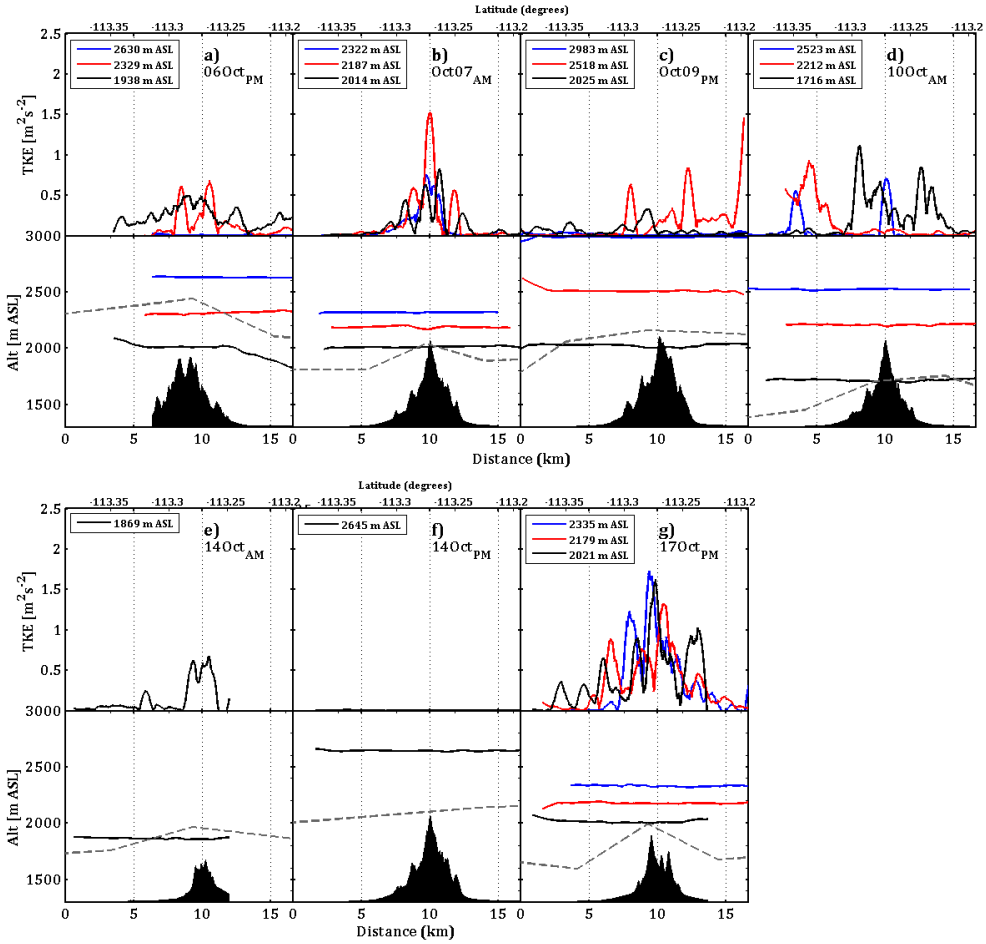

FIGURE 2.5: Top: Turbulent kinetic energy calculated from airborne observations for the Granite Peak flight legs during the a.) 06Oct_{PM}, b.) 07Oct_{AM}, c.) 09Oct_{PM}, d.) 10Oct_{AM}, e.) 14Oct_{AM}, f.) 14Oct_{PM}, and g.) 17Oct_{PM} flight periods. Bottom: Flight legs plotted over elevation profiles of underlying terrain (*black solid line*) Estimated CBL height (zi) included (*grey dotted line*).

absence of shear generated turbulence. *In-situ* aircraft observations at the upper-level flight legs during the 10Oct_{AM} period reveal that strong perturbations in vertical velocity occur in a narrow zone over Granite Peak. In general, the vertical velocity variations are out of phase with u, v, and θ variations. Similar to the observations over the Eastern Slope, these phase relations imply a small wave breaking region with negative momentum and sensible heat fluxes (Jiang et al. 2010). The airborne observations confirm the existence of a negative heat and momentum flux in this region on both of these days (not shown). While negative heat flux suppresses TKE, the negative momentum flux aids the generation of TKE over the mountain.

In contrast to other flights, the location of TKE maxima during the $07Oct_{AM}$ and $17Oct_{PM}$ periods can partly be explained by a terrain following *zi* as observed by aerosol structure information from TODWL during the $07Oct_{AM}$ and $17Oct_{PM}$ flights (not shown) and by *in-situ* observations of potential temperature. The terrain following *zi* caused the aircraft to sample air in the CBL over the mountain crest and air above the CBL over the surrounding plains. On $07Oct_{AM}$, there is a 1 K decrease in potential temperature over Granite Peak at the lower-level flight leg (Fig. 2.6a). On $17Oct_{PM}$, the potential temperature along the flight legs is more variable. However, the potential temperature still decreases approximately 0.5-1 K from the western to the eastern side of Granite Peak during the $17Oct_{PM}$ period indicating that *zi* was higher over Granite Peak and the Sagebrush compared to the Playa (Fig. 2.6b).

Interestingly, during the $07Oct_{AM}$ and $17Oct_{PM}$ periods, the terrain following shape of TKE along a horizontal flight leg is conserved even at the upper-level flight legs; which were several hundred meters above the *zi* estimated from the aerosol structure. *In-situ* aircraft observations used to estimate TKE were taken as much as 120-150 minutes after the TODWL flight observations during which the CBL could have grown another 100-200 m. The large values of TKE (> 0.25 m^2 s^{-2}) observed by aircraft (Fig. 2.5b and 5g) suggest this is indeed the case, and that the aircraft was sensing air from the CBL at lower-levels and/or the entrainment zone at the upper flight levels.

The strongest winds over Granite Peak are south-southwesterly at 5-8 m s^{-1} during the $10Oct_{AM}$ period. Winds during the $06Oct_{PM}$, $07Oct_{AM}$, $17Oct_{PM}$ are north-northwesterly and relatively weak (3-5 m s^{-1}). There is no clear relationship between the location and magnitude of TKE maxima, stability, and lower level winds over Granite Peak. TKE maxima are consistently found over the crest of Granite Peak regardless of the winds or stability. Interestingly, the largest TKE maxima are observed during the $17Oct_{PM}$ period, which neither has the strongest winds or most unstable conditions. The location and magnitude of TKE maxima may also be affected by other factors that are difficult to quantify including the amount of heat and momentum transfer between the CBL and the free troposphere.

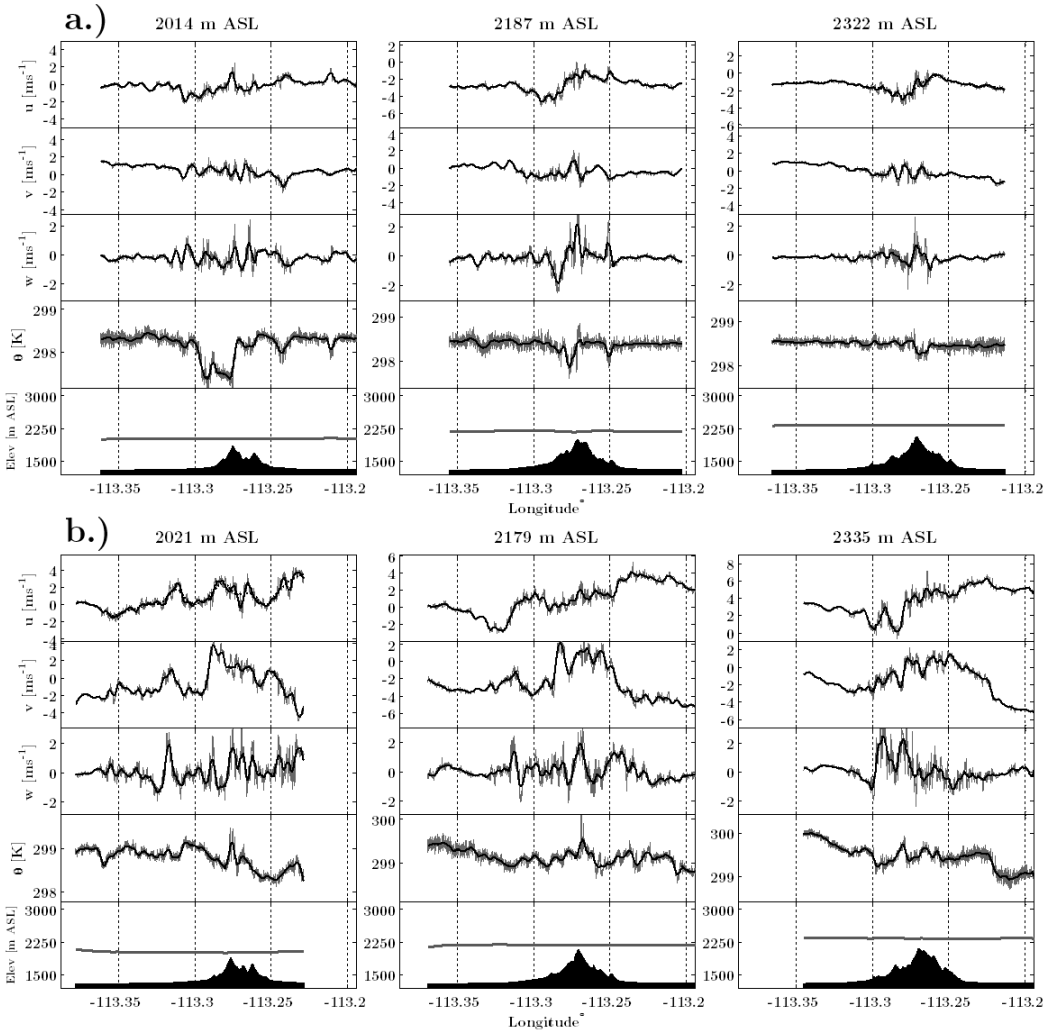

FIGURE 2.6: Airborne*in-situ* observations (w, u, v, and θ) from three flight legs over Granite Peak during the a.) 07Oct_{AM} and b.) 17Oct_{PM} flight periods. Solid black line is a 500 m moving average. Elevation cross section of underlying terrain is plotted below.

2.3.4 Big Gap (terrain gap)

Multiple TKE maxima are observed in and at the exit of the Big Gap during the flight periods. The largest TKE maximum occurs during the 17Oct_{PM} period while the smallest occurs during the 07Oct_{AM} period. During the 17Oct_{PM} flight, there are TKE maxima of 1.0 $\text{m}^2\ \text{s}^{-2}$ and 1.5 $\text{m}^2\ \text{s}^{-2}$ at the lower and upper flight levels, respectively, near the western exit of the gap (Fig. 2.7g). A relatively broad TKE maximum (1.5 $\text{m}^2\ \text{s}^{-2}$) is present in the middle of the terrain gap during the 06Oct_{PM} period (Fig. 2.7a). TKE maxima larger than 0.5 $\text{m}^2\ \text{s}^{-2}$ occur at the 10Oct_{AM} lower flight compared

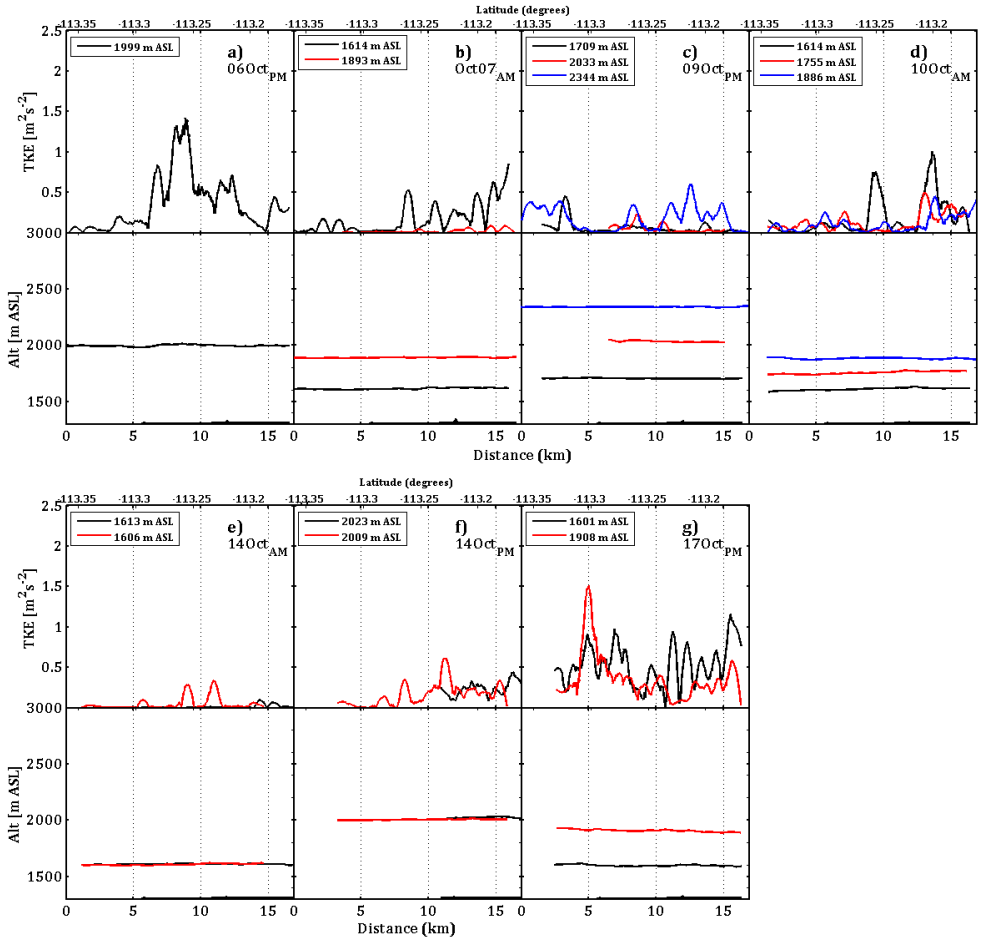

FIGURE 2.7: Top: Turbulent kinetic energy calculated from airborne observations for the Gap flight legs during the a.) 06Oct_{PM}, b.) 07Oct_{AM}, c.) 09Oct_{PM}, d.) 10Oct_{AM}, e.) 14Oct_{AM}, f.) 14Oct_{PM}, and g.) 17Oct_{PM} flight periods. Bottom: Flight legs plotted over elevation profiles of underlying terrain (*black solid line*) Estimated CBL height (*zi*) included (*grey dotted line*).

to the mid and upper flight levels during the 06Oct_{PM} and 17Oct_{PM} flight periods with TKE < 0.50 m^2 s^{-2}. Similarly, TKE is < 0.50 m^2 s^{-2} at all 07Oct_{AM} flight levels, and no significant TKE maxima are observed in the gap.

Acceleration of the flow through the terrain gap and the generation of turbulent wakes at the gap exit extending downstream could be responsible for the large values of TKE observed during the 06Oct_{PM} and 17Oct_{PM} periods. During these flight periods in the afternoon, flows with a northerly component dominate with a northeasterly flow component through the gap aligned with the gap direction.

TODWL horizontal winds show that lower-level northerly flow diverged around

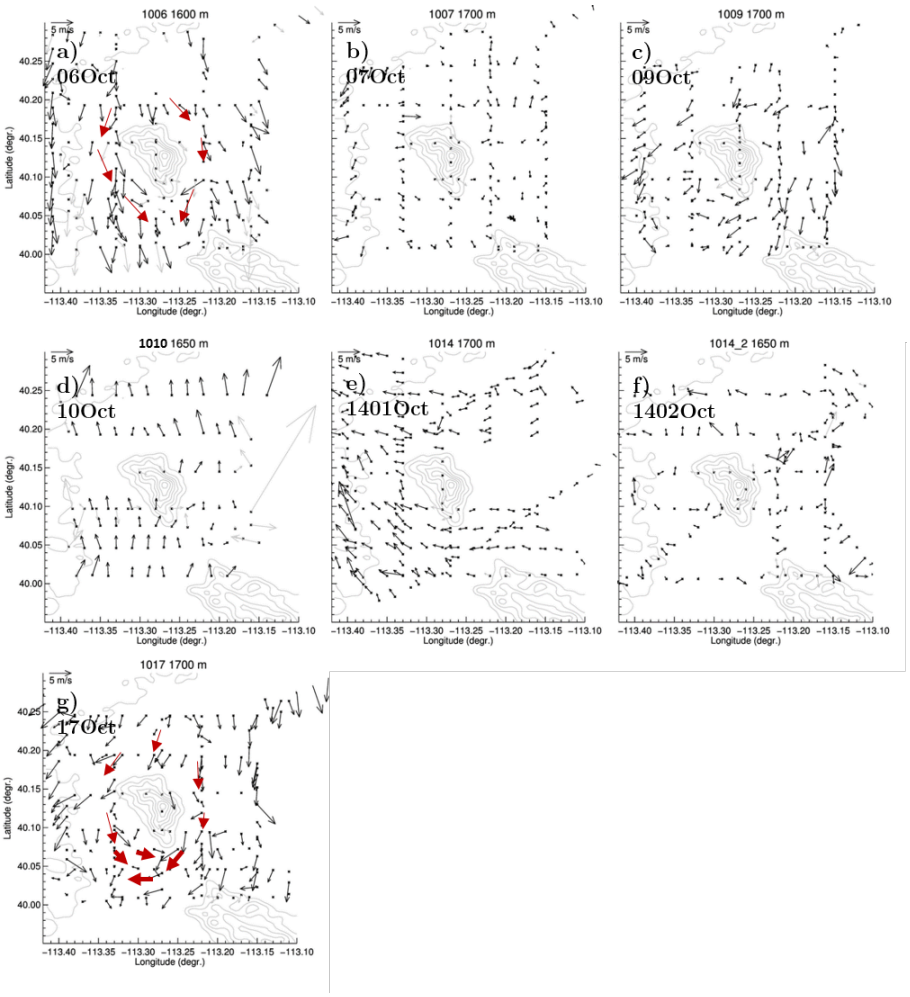

FIGURE 2.8: TODWL horizontal wind profiles at 1600-1700 m ASL over the experimental domain for the seven flight periods. Elevation contours are plotted below. Red arrows outline the flow that diverged around Granite Peak and through the gap during the a) 06Oct_{PM} and g) 17Oct_{PM} period. *Thick dark red arrows* during the 17Oct_{PM} period represents the turbulent wake region.

Granite Peak and went through the terrain gap during the 06Oct_{PM} and 17Oct_{PM} periods (Fig. 2.8a and 2.8g). When there is airflow through a gap, the air accelerates, with the strongest winds at the narrowest point, a phenomenon known as the Bernoulli or "venturi" effect (Whiteman 1990). However, the venturi mechanism is different from most real gap wind situations, where the strongest winds are generally over the exit region of the gap, not at the narrowest section or constriction (Mayr 2005). Previous investigations suggested that strong winds at the exit region of a gap can create turbulent wakes that can propagate downwind of a gap (Baines 1979).

The 17Oct_{PM} TKE maximum corresponds to acceleration of the horizontal flow (u

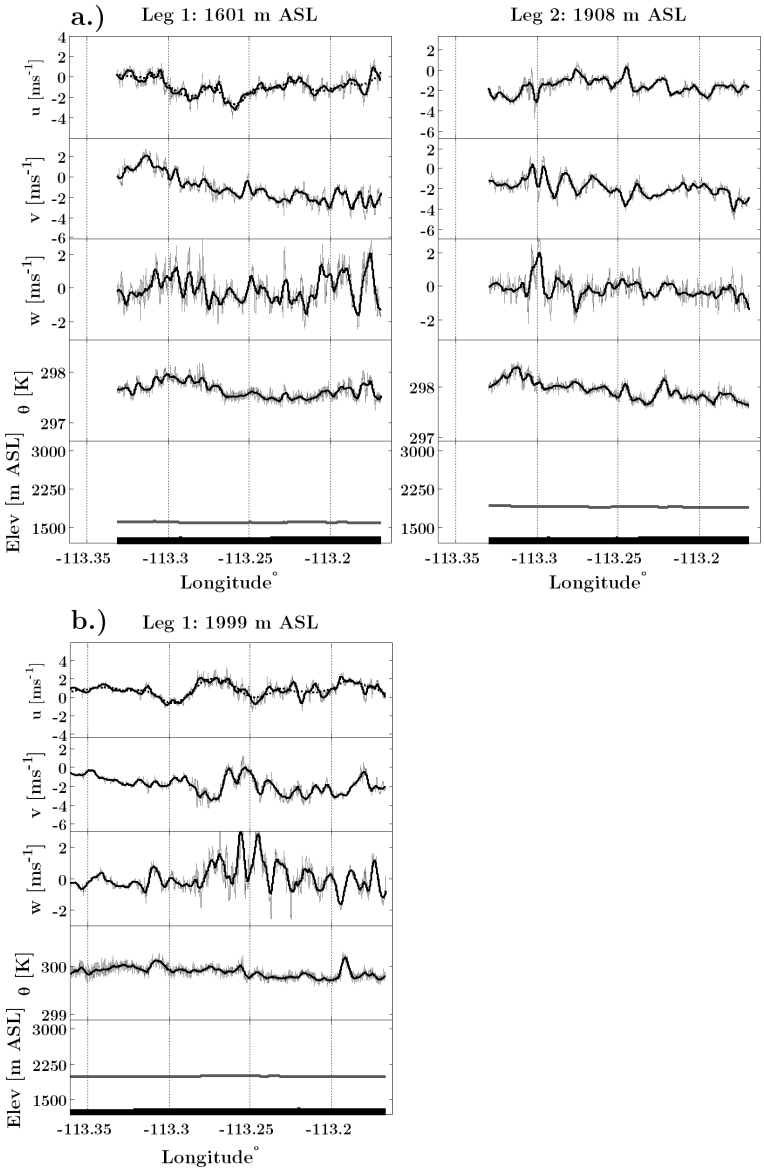

FIGURE 2.9: Airborne *in-situ* observations (w, u, v, and θ) through the Big gap at the lower (a) and upper (b) flight legs during the 17Oct_{PM} flight period and the flight leg during the 06Oct_{PM} flight period (c). Solid black line is a 500 m moving average. Elevation cross section of underlying terrain is plotted below with altitude of flight leg (*solid gray line*)

component) from < -1 m s^{-1} to -3.5 m s^{-1} (easterly acceleration) between 113.25° – 113.30° W (Fig. 2.9a) and to a possible turbulent wake region at the western exit of the gap (113.26°W - 113.31°W). This region is denoted with thick dark red arrows in Fig. 2.8g. Flight observations during the 17Oct_{PM} also indicate increased momentum and heat fluxes (not shown). These observations suggest increased turbulence and vertical mixing as the flow fans out from the gap exit (Baines 1979). In a previous study,

Fernando et al. (2015) noted the development of a turbulent wake and vortex shredding in this region due to northerly flow diverging around Granite Peak through the gap.

The origin of the TKE maxima in the middle of the gap during 06Oct_{PM} is different than 17Oct_{PM}. Airborne *in-situ* and TODWL observations (not shown) of the horizontal wind indicate relatively weak winds (< 3 m s^{-1}) from 1500-2000 m MSL and no significant acceleration of the flow in the gap. However, some deceleration of the flow (associated with a change in lateral wind component (v) from -4 to 0 m s^{-1} and the longitudinal wind component (u) wind component from ≈ 0 to 2 m s^{-1}) is evident in the middle of the gap ($113.23° - 113.27°$ W) (Fig. 2.9b). This region is also associated with increased vertical uplift (Fig. 2.9b), momentum, and heat fluxes (not shown). These observations suggest that the TKE maximum in the gap during the 06Oct_{PM} period is not produced by flow acceleration through the gap. One possible explanation is the generation of turbulence in the wake south of Granite Mountain as northerly flows go over and around the mountain (lee side turbulence). A TKE maximum generated this way would also occur in the absence of the gap.

2.3.5 Sagebrush and Playa

TKE along the flight legs over the Sagebrush and Playa is shown in Figs. 10 and 11, respectively. The average TKE over the Sagebrush is largest during the 17Oct_{PM} period, with a number of TKE maxima at the lower flight level that are > 1.0 m^2 s^{-2}. Some of these maxima are associated with localized regions of increased heat fluxes, while others correspond to negligible heat fluxes but relatively large negative momentum fluxes (not shown). TKE is somewhat smaller during the 10Oct_{AM} period, and maxima of 0.50-1.0 m^2 s^{-2} are observed at the lower and mid-levels in the region $40.15° - 40.20°$ N. In this area, increased uplift and heat fluxes are evident. There are also a few narrow TKE maxima of 0.50-1.0 m^2 s^{-2} observed across the 06Oct_{PM} flight leg which are more associated with negative momentum fluxes than with positive heat fluxes (not shown). Only a few small TKE maxima ≈ 0.6 m^2 s^{-2} are observed during the 07Oct_{AM} flight period.

TKE is generally negligible and < 0.25 m^2 s^{-2} over the Playa across most flight periods. The only flight period where TKE is > 0.25 m^2 s^{-2} is during the 17Oct_{PM}

flights. In particular, there is a TKE maximum ≈ 0.75 m^2 s^{-2} at the lower flight level at approximately 40.09° N. Heat and momentum fluxes are too small to explain these TKE maxima. However, increased vertical velocities corresponding with the TKE maxima suggest that these maxima are due to the vertical transport of TKE from lower levels within the CBL.

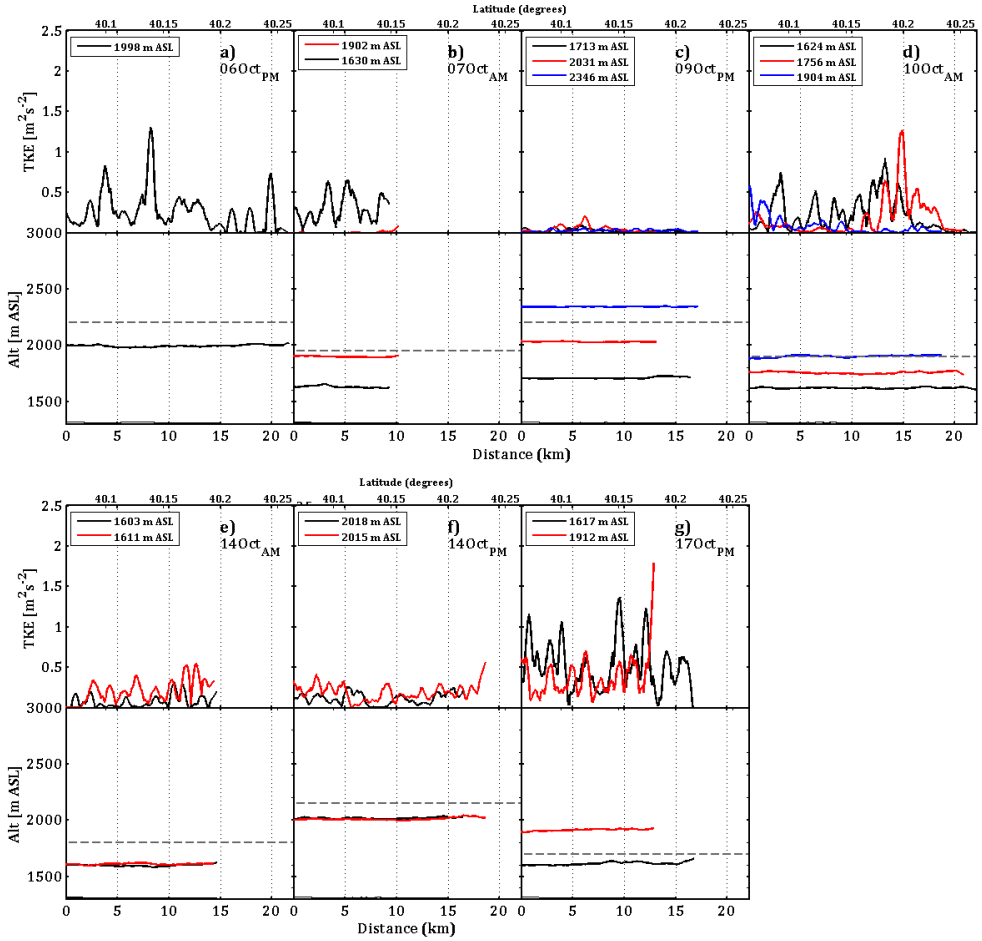

FIGURE 2.10: Top: Turbulent kinetic energy calculated from airborne observations for the Sagebrush flight legs during the a.) 06Oct$_{PM}$, b.) 07Oct$_{AM}$, c.) 09Oct$_{PM}$, d.) 10Oct$_{AM}$, e.) 14Oct$_{AM}$, f.) 14Oct$_{PM}$, and g.) 17Oct$_{PM}$ flight periods. Bottom: Flight legs plotted over elevation profiles of underlying terrain (*black solid line*). Estimated CBL height (*zi*) included (*grey dotted line*).

TKE over the Sagebrush varies considerably from flight period to flight period. The largest TKE is observed during 17Oct$_{PM}$ when the flow within the CBL is weaker (3-4 m s^{-1}) compared to the 10Oct$_{AM}$ period (5-8 m s^{-1}) (Table 2). However, the wind above the CBL during the 17Oct$_{PM}$ increases to ≈ 10 m s^{-1} at 2500 m MSL and there

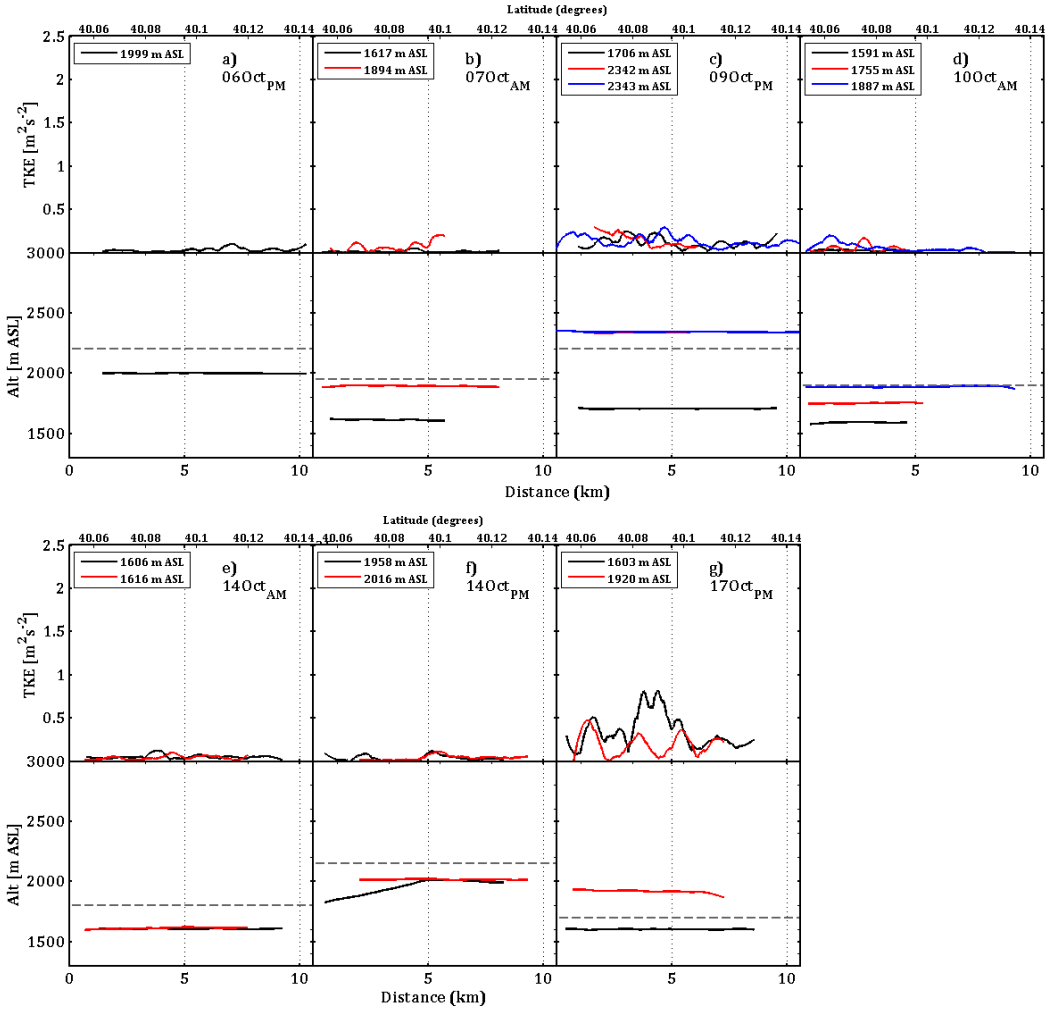

FIGURE 2.11: Top: Turbulent kinetic energy calculated from airborne observations for the Playa flight legs during the a.) 06Oct_{PM}, b.) 07Oct_{AM}, c.) 09Oct_{PM}, d.) 10Oct_{AM}, e.) 14Oct_{AM}, f.) 14Oct_{PM}, and g.) 17Oct_{PM} flight periods. Bottom: Flight legs plotted over elevation profiles of underlying terrain (*black solid line*). Estimated CBL height (*zi*) included (*grey dotted line*).

is significant shear near the CBL top ($10^{-2}s^{-1}$). Past studies have noted that shear near the top of the CBL can enhance entrainment of upper-level flow from the FA to the CBL (e.g. Fedorovich and Conzemius 2008; Pino and Vilà-Guerau De Arellano 2008; Conzemius and Fedorovich 2006a). It is likely that the shear topped CBL increases the downward transport of momentum and subsequently increases TKE. Shear near the CBL top during the 10Oct_{PM} period ($10^{-3}s^{-1}$) is not as large. The weakest winds (2-3 m s^{-1}) occur during the 06Oct_{PM} flight period but relatively large surface sensible heat fluxes (120 Wm^{-2}) during this period result in comparable TKE during the 06Oct_{PM}

flight period compared to the 10Oct_{AM} flight period. Wind speed, wind shear, surface forcing, and stability all impact the magnitude and location of TKE maxima but the relative contribution from each of these factors is difficult to assess.

An aspect that deserves some attention concerns the occurrence of TKE maxima over the flat terrain of the Sagebrush area at somewhat regular distance during the 06Oct_{PM}, the 07Oct_{AM}, 10Oct_{AM}, and 17Oct_{PM} flight period. Surface based convection generates thermal updrafts and downdrafts that can have a signature in the TKE (Young 1988; Lenschow 1970). In a CBL with significant wind shear, semi-organized convective rolls could also be present (LeMone 1973). The aircraft observations reveal increased uplift and locally buoyant air (positive heat fluxes) associated with many of the TKE maxima over the Sagebrush and both thermals and rolls generated the observed TKE variability.

Overall, TKE in the CBL is 0.5–1 $\text{m}^2\ \text{s}^{-2}$ larger over the Sagebrush than over the Playa (Fig. 2.10 and 2.11). The only period with TKE $> 0.25\ \text{m}^2\ \text{s}^{-2}$ over the Playa is during the 17Oct_{PM} flights. A large part of the differences in TKE between the Sagebrush and Playa can be attributed to the differences in surface forcings over these regions (Doran et al. 1992; Doran et al. 1995; Michels and Jochum 1995). Observations from towers over the Sagebrush and Playa indicate the Sagebrush had larger surface sensible heat fluxes than the Playa resulting in larger TKE over the Sagebrush than over the Playa.

2.3.6 Conceptual discussion of TKE

Our results can be summarized in Fig. 2.12 and 2.13 , which show how the location of TKE maxima is influenced by terrain.

There are TKE maxima along the flight legs that correspond to underlying ridge tops over the Eastern Slope. Large TKE values over the Eastern Slope ranging from 1-2.5 $\text{m}^2\ \text{s}^{-2}$ are not only found during periods with strong low-level flow ($> 5\ \text{m}\ \text{s}^{-1}$) but also during periods with weak low-level flow ($< 5\ \text{m}\ \text{s}^{-1}$). Previous studies have found comparable TKE values of 1-1.25 $\text{m}^2\ \text{s}^{-2}$ over valley sidewalls in the presence of up valley flows (Weigel et al. 2007b) and of 2-4 $\text{m}^2\ \text{s}^{-2}$ over mountain ridges during ambient winds $> 5\ \text{m}\ \text{s}^{-1}$ Hahn 1980). Forced flow ($> 5\ \text{m}\ \text{s}^{-1}$) over topography produces dynamical phenomena in the form of wave breaking regions at upper levels above the terrain (Fig.

2.12a). At lower levels, the interaction between the flow and topography aids in the vertical transport of heat from the ridge tops and drives the production of TKE by thermal forcings. Turbulence is largest in the wave breaking regions, where downward momentum transport drives the production of TKE.

During periods when the flow is < 5 m s^{-1} over the Eastern Slope, intense mixing over the topography is driven by positively buoyant air originating from the slopes and ridge tops (Fig. 2.12b). These buoyant plumes rise above the ridge tops and penetrate into the stable layer above the CBL . The interaction between the rising buoyant plumes and stable layer draws down faster flow from aloft into the CBL. The buoyant air at lower-levels and downward momentum transport at mid and upper levels aid in the production of TKE.

In the presence of a terrain following *zi*, large TKE maxima are noted above the crest of Granite Peak (Fig. 2.12c). A terrain-following *zi* causes the aircraft to observe turbulent CBL air over the mountain crest (below *zi*) and non-turbulent FA air over the surrounding plains (above *zi*). The effect of a terrain following *zi* is clearly seen as a rapid decrease in TKE 5 km from Granite Peak with a more rapid decline west than east of Granite Peak. The more rapid decrease towards the west is attributed to a relatively lower *zi* and shallower CBL mixed layer on the western side (Playa) compared to the eastern side (Sagebrush) of Granite Peak (Fig. 2.12c).

The observed TKE maxima over Granite Peak are generated by a combination of positively buoyant air originating from the heated mountain top and mechanical mixing driven by the transport of higher momentum from aloft. The generation of TKE by heating of the mountain top and downward transport of momentum is similar to what has been observed in past studies (Banta 1984; Hahn 1980; Lenschow et al. 1979).

The magnitude of TKE over the Sagebrush is greater than that over the Playa within the CBL (Fig. 212c.). This is due to larger surface sensible heat fluxes over the Sagebrush which create a deeper CBL over the Sagebrush than over the Playa. These results are consistent with previous investigations (e.g. Doran et al. 1992; Doran et al. 1995; Michels and Jochum 1995).

The TKE maxima in and at the exit of the terrain gap are due to several processes. The first is associated with terrain gap flow fanning out creating a turbulent wake at

the exit of the terrain gap (Fig. 2.13a). Second is the formation of a lee side turbulent region in the middle of the terrain gap (wake of Granite Peak) due to flow coming over and around the mountain (Fig. 2.13b).

2.4 Summary and conclusions

The objective of this study was to investigate the spatial variability of turbulence kinetic energy (TKE) in the convective boundary layer over an isolated mountain ridge with a focus on the location and magnitude of TKE maxima. The analysis was based on airborne *in-situ* observations over the isolated mountain, Granite Peak from seven different flight periods during the MATERHORN-X experiment. Airborne Doppler wind lidar observations over the experimental domain were also utilized to illustrate how the flow structure and spatial variations in *zi* influenced the observed TKE field.

TKE was investigated from multiple flight legs over five main regions 1) Sagebrush, 2) Big Gap, 3) Playa, 4) Granite Peak, and 5) Eastern Slope. Results showed that terrain significantly influenced the location of TKE maxima. The influence of terrain on the location of TKE maxima was most prevalent and the clearest over Granite Peak and the Eastern Slope during the 06Oct_{PM}, 10Oct_{AM}, and 17Oct_{PM} flight periods. TKE over these regions ranged between 1-2.5 $\text{m}^2\ \text{s}^{-2}$ and was considerably variable. The generation of TKE during these periods is attributed to 1) shear production associated with flow forced over topography and the downward transport of momentum from aloft and 2) buoyant production related to increased heat fluxes over ridge tops and the mountain crest. In Part II of this study, the relative contributions of shear and buoyancy generated turbulence will be investigated, for a select number of flights where TKE was large over the Eastern Slope and Granite Peak.

The use of TODWL observations in the analysis of general flow patterns proved to be useful for visualizing the spatial patterns and variations of the flow that would otherwise not be seen with radiosonde or *in-situ* observations. In particular, TODWL revealed flow through a terrain gap to the south of Granite Peak. This information offered some novel insights of gap flow features and associated TKE variability under unstable conditions.

Considerable variability in the magnitude and location of TKE maxima was observed among the flight periods that could only partially be explained. This study therefore also demonstrates the difficulty of finding consistent and repeatable patterns in TKE variability even in the presence of a single mountain ridge.

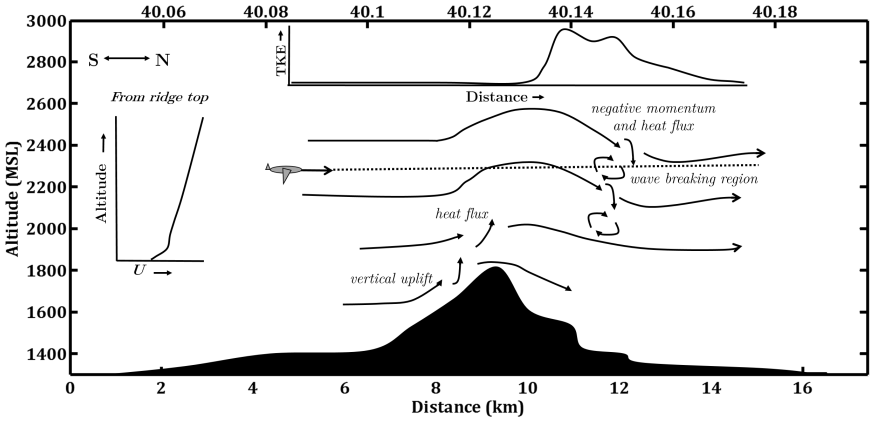

(a) Eastern Slope flow

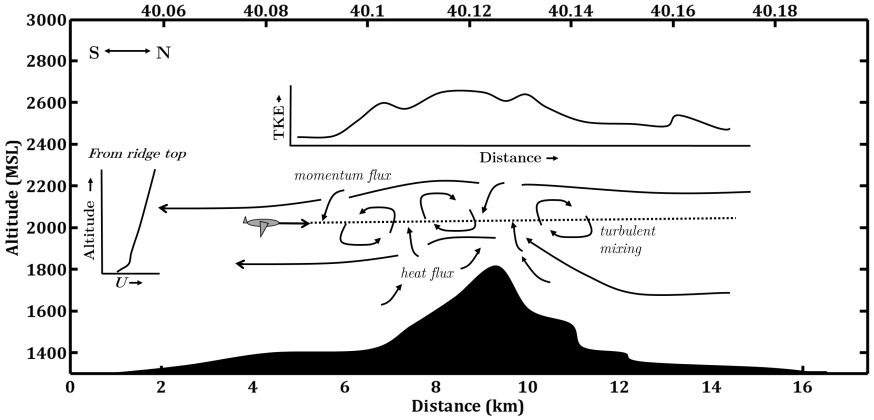

(b) Eastern Slope flow

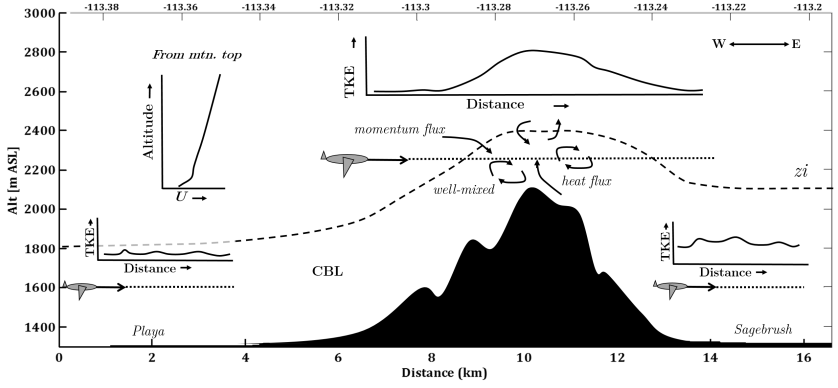

(c) Granite Peak

FIGURE 2.12: Conceptual diagram showing how the upward transport of positively buoyant air and downward transport of stronger momentum contributes to TKE over a.) the Eastern Slope during winds $> 5\,ms^{-1}$, b.) ridge top of across the Eastern Slope during weak winds ($< 5\ ms^{-1}$), and c.) the crest of Granite Peak during weak winds ($< 5\ ms^{-1}$). Conceptual cross-sectional plots of TKE (*black solid line*) over different regions are given in each figure. In addition, a vertical profile of the mean wind (U) from ridge top and the crest of Granite Peak is given. The Eastern Slope cross section only shows one ridge for simplicity. In reality, more ridges are present from the various tributary valleys.

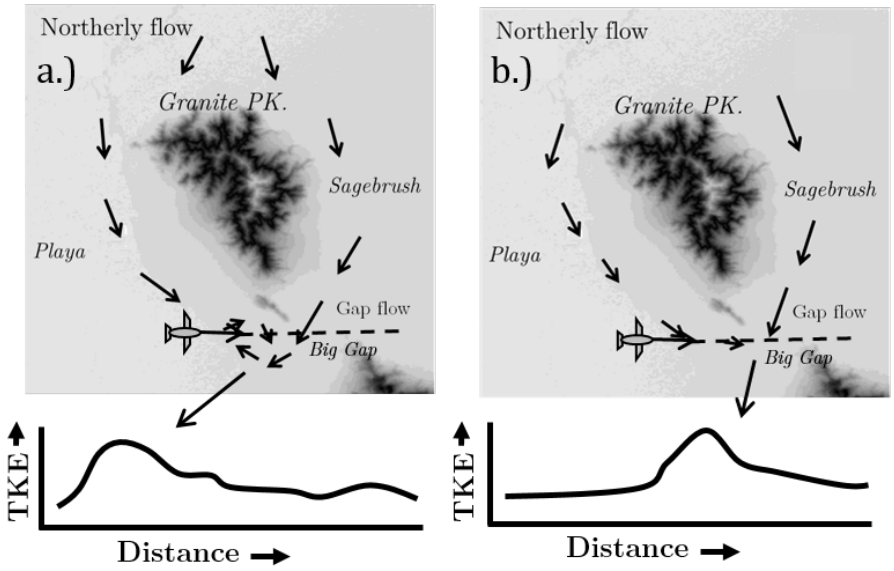

FIGURE 2.13: The observed TKE field during due to a.) terrain gap flow fanning out from the gap causing the formation of a turbulent wake and b.) the formation of a leeside turbulent region in the middle of the gap due to flow coming over and around Granite Peak. A conceptual cross-sectional plot of TKE through the gap (*black solid line*) is given.

Chapter 3

Sources and mechanisms of TKE

Abstract

In Part I of this two-part study, the location of turbulent kinetic energy (TKE) maxima was determined over the isolated mountain, Granite Peak, during seven different flight periods from the fall 2012 Mountain Terrain Atmospheric Modeling and Observation (MATERHORN) Program at Dugway Proving Ground (Utah, USA). The main objective of Part II of this study is to investigate the relative contribution of various turbulence production and destruction mechanisms in producing the observed TKE field for several case studies. The analysis focuses on the Eastern Slope during the 06Oct_{PM}, 10Oct_{AM} and 17Oct_{PM} flight periods and on Granite Peak during the 17Oct_{PM} flight period. Certain thermodynamic and dynamic processes are found to influence the mechanisms important for the generation of the TKE maxima. At lower levels over the slopes and ridge of the mountain, TKE maxima are generated by buoyant production associated with topographically and thermally forced regions of increased uplift and sensible heat flux. However, even during unstable conditions with weak synoptic flow (< 5 m s^{-1}), shear production is a significant contributor to the generation of TKE maxima. The contribution of shear production to TKE is attributed to enhanced entrainment of momentum into the CBL over topography. During periods with synoptic flow > 5 m s^{-1} over the slopes and ridges, dynamically forced flows contribute to the TKE maxima by producing regions with increased shear instability. This shear instability is attributed to the downward transport of momentum in a wave breaking region that forms downwind of a ridge top.

3.1 Introduction

Observations of atmospheric turbulence over the last few decades have advanced our knowledge of dynamic and thermodynamic processes in the atmospheric boundary layer. The development and evaluation of turbulence parameterization schemes that are widely used in atmospheric numerical models rely on these observations and have led to the improvement of weather and climate models.

In a previous paper, we investigated the spatial variability of TKE in and above the CBL over an isolated mountain ridge. The focus of the investigation was on localized regions of increased TKE. Airborne data were used from the first Mountain Terrain Atmospheric Modeling and Observations Program experiment (MATERHORN-X; Fernando et al. 2015) performed over the isolated mountain Granite Peak in Utah (elevation $\approx$ 2159 m MSL; length $\approx$ 10 km; base width $\approx$ 1.5 km; ridge top height $\approx$ 800-900 m). Localized regions of increased TKE were found to coincide with the crest of Granite Peak and with ridges associated with tributary valleys along the Eastern Slope. TKE was found to decrease by an order of magnitude 5 km east (downwind) and 2.5 km west (upwind) of Granite Peak. Although the study was conducted during conditions with weak synoptic forcing, observations show flow features that are common in conditions with strong cross barrier flow (e.g. dynamically forced flow over terrain, wakes, and small wave breaking regions). These features influenced the TKE structure downwind of the mountain and in a terrain gap to the south.

In the current paper, we investigate the relative contribution of shear and buoyancy-generated turbulence and the underlying processes over and downwind of the isolated mountain for several case studies. The observations from these case studies are suitable for calculating shear and buoyancy production/destruction and TKE dissipation as three primary terms in the TKE budget equation. Through an investigation of the magnitude and spatial variability of these budget terms, significant sources and sinks of turbulence associated with the various TKE maxima can be identified.

We will use turbulence-based aircraft data, Doppler wind lidar, and surface meteorological observations collected during the MATERHORN-X campaign (Fernando et al.

2015). The remainder of the paper is organized as follows: Section 3.2 provides background information on TKE budgets in the CBL over flat homogeneous and mountainous terrain. Section 3.3 describes the experimental data set used for analysis. Section 3.4 addresses methods to calculate TKE budget terms from airborne observations. Section 3.5 presents the results and discussion of the budget terms where TKE maxima were found over the Eastern Slope and Granite Peak. A detailed conceptual discussion of the dynamic/thermodynamic processes important for the generation of the TKE maxima during the different case studies is also provided. The summary and conclusions are presented in Section 3.6.

3.2 Background

3.2.1 TKE budget terms over flat homogeneous terrain

Many studies have attempted to quantify turbulence and identify the turbulence production mechanisms by calculating TKE and associated budget terms. These terms include buoyancy production/destruction, shear production, and dissipation of turbulence. Results from these studies have led to a general understanding of the structure and profile of TKE over flat and homogeneous terrain during quiescent fair weather (e.g. Wyngaard and Coté 1971; Lenschow 1974; Kaimal et al. 1976; Caughey and Palmer 1979).

The TKE budget equation is simplified considerably if horizontal homogeneity is assumed, where mean quantities only vary in the vertical and the mean velocity U is aligned with the mean wind. If turbulence is also assumed to be isotropic, and the TKE budget is in equilibrium (i.e. left-hand side of Eq. (1) is zero), the TKE budget equation becomes (Hahn 1980):

$$0 = -\overline{u'w'}\frac{\partial \overline{u}}{\partial z} - \overline{v'w'}\frac{\partial \overline{v}}{\partial z} + g\frac{\overline{w'\theta_v'}}{\overline{\theta_v}} - \epsilon - \frac{\partial}{\partial z}\left[\frac{1}{\rho}(\overline{w'p'} + \overline{w'e})\right] \tag{3.1}$$

Where $\overline{e}$, represents the physical value of TKE ($\overline{e} = \frac{1}{2}(u'^2 + v'^2 + w'^2)$). In Eq.(2), the remaining terms are (in order): shear or mechanical production, buoyant production, dissipation, and vertical and pressure transport. The first four terms are measurable and are often considered in experimental studies. The last term represents the transfer of

kinetic energy from one region in space to another due to correlations between fluctuating pressure and velocity.

In the surface layer, Wyngaard and Coté (1971) investigated the TKE budget. They found that buoyancy and shear production of TKE was largest near the surface due to the rising and mixing of thermals and wind shear. Other investigations have studied the height variation of TKE budget terms above the surface layer (e.g. Wyngaard and Coté 1971). Kaimal et al. (1976) and Caughey and Wyngaard (1979) showed that TKE generated in the surface layer is transported vertically into the mixed layer. Above the surface layer, Caughey and Palmer (1979) found that shear production decreases significantly and becomes unimportant in the mixed layer where the vertical wind gradient is small. Lenschow (1974) used aircraft observations and a model to investigate the TKE budget terms in the mixed layer and near the CBL top. This study found that buoyancy was the dominant TKE production mechanism in the mixed layer. However, buoyancy decreased with height, and the vertical transport of TKE increased almost linearly to balance the decrease of the buoyancy-generation term. Dissipation of TKE was found to be relatively constant with respect to height in the mixed layer and proportional to the production of TKE.

In the entrainment zone, stable air from the free atmosphere is engulfed by CBL air and, as a result becomes part of the CBL (Randall and Schubert 2004). Studies have noted TKE destruction by buoyancy in this region (e.g. Caughey and Palmer 1979; Lenschow and Stephens 1980, Caughey 1982). These investigations have also found that higher momentum air from above the CBL can be mixed downwards by entrainment. As a result, some production of TKE by shear was found within the entrainment zone. Dissipation increased slightly near the entrainment zone to compensate for the shear production of TKE. The vertical transport of TKE was maximum at the base of the entrainment zone and decreased above.

A CBL solely driven by buoyancy rarely exists in nature. Usually, CBL flow structure is modified by combination of buoyant forcings and wind shear. (Fedorovich and Conzemius 2008; Pino and Vilà-Guerau De Arellano 2008; Conzemius and Fedorovich 2006a; Conzemius and Fedorovich 2006b; Moeng and Sullivan 1994). Differences in CBL flow structure are known to affect the relative combination of wind shear and buoyancy

forces that produce TKE within and near the CBL top. Shear instabilities occur locally, while buoyancy forces set up vigorous thermals, which result in non-local transport of heat and momentum. Depending on the flow structure, buoyancy and shear can act together to modify the TKE field (Moeng and Sullivan 1994). Numerous modeling and observational studies have investigated the variability of the TKE budget terms during differing conditions with a range in shear and buoyancy combinations (e.g. Fedorovich and Conzemius 2008; Pino and Vilà-Guerau De Arellano 2008; Conzemius and Fedorovich 2006a; Conzemius and Fedorovich 2006b; Moeng and Sullivan 1994; Caughey and Palmer 1979; Zeman and Tennekes 1977; Tennekes 1973; LeMone 1973; Lenschow 1970).

Boundary layers that are solely driven by shear usually occur during stable and neutral conditions and are characterized by wind speed that steadily increases with height above the surface. Moeng and Sullivan (1994) found from large eddy simulations that shear production dominates the generation of TKE from the surface layer through the mid part of the boundary layer. The contribution of buoyancy production was negligible through the depth of the boundary layer.

Additionally, boundary layers can be characterized by both buoyancy and shear processes (Moeng and Sullivan 1994). Even early observational studies noted the combined effects of wind shear and buoyancy on the development of the CBL and TKE. Hoxit (1974) conducted a study analyzing radiosonde data over four consecutive cold seasons. Their findings provide evidence of turbulent downward transport of horizontal momentum associated with shear above the CBL. Kaimal et al. (1976) analyzed data from a field experiment in northwestern Minnesota and found unexpectedly large turbulent stress in the upper portion of the CBL, which was taken as evidence of heat and momentum entrainment into the CBL. Caughey and Palmer (1979) confirmed the effects of entrainment by investigating heat and momentum flux profiles in the CBL. Their observations indicated enhancement of entrainment by shear near the CBL top and subsequent shear production of TKE in the upper half of the CBL. Chou et al. (1986) measured turbulence using aircraft in a horizontally evolving CBL during a cold air outbreak over the Atlantic Ocean off the east coast of the United States. Their analysis of TKE budgets showed that shear was a significant term in the turbulence production in

the CBL. The shear term was not only important near the surface, where it was largest, but also near the CBL top. However, there was uncertainty in the estimate of the local shear at the CBL top since the vertical spacing of flight legs was large. Nevertheless, the data provided evidence that shear production was a significant contributor to the TKE production in that particular CBL.

More recent model based studies have investigated the influence of shear on CBL structure and TKE in more detail. Fedorovich and Conzemius (2008) showed that when wind shear near the CBL top is present, the mixed layer acquires a two-layer structure. The two-layer structure is composed of a layer of height-constant buoyancy and velocity, which is similar to the shear-free CBL, topped by a shear-driven layer whose turbulence is maintained by a balance among shear generation, buoyancy consumption, and dissipation of TKE. The shear enhances mixing near the CBL top and effectively transports higher momentum air down from the FA, increasing TKE by shear production (Pino and Vilà-Guerau De Arellano 2008; Fedorovich and Conzemius 2008). Dissipation of TKE is nearly uniform with height in the lower half of the CBL. In the upper half of the CBL, dissipation increases to compensate for shear production induced by entrainment processes. Most of the shear that exists in the entrainment zone is locally created and dissipated.

3.2.2 TKE budget terms over complex terrain

Over non-uniform and complex topography with variability in surface characteristics, such as vegetation, moisture, and topography, additional uncertainties exist in the variability and magnitude of the TKE budget terms (Rotach and Zardi 2007; Weigel et al. 2007b; Weigel et al. 2007a; Orlanski 1975).

Previous studies over mountainous terrain in unstable boundary layers (e.g. Hahn 1980) and neutral boundary layers (e.g. Karacostas and Marwitz 1980; Hahn 1980; Lothon et al. 2003; Jiang et al. 2010) have shown that underlying terrain substantially influences the production mechanisms of TKE. In a neutral boundary layer, Lothon et al. (2003) showed that strong Foehn winds over the Alps created strong slope winds, rotors, waves, and wakes downwind of mountain ridges. These flow features produced localized regions of increased TKE driven by shear production. Karacostas and Marwitz (1980)

investigated the TKE budget across the isolated Elk Mountain, WY during strong winds (> 10 m s^{-1}) in a neutral boundary layer. The study found that TKE was largest in the lee side due to shear instability induced by a hydraulic jump and stationary eddy. Also, dissipation was the largest term and proportional to the production of TKE by shear and buoyancy.

Hahn (1980) conducted a study analyzing TKE budget terms over the Front Range of the Rockies during conditions characterized by weak winds in the CBL and strong westerly winds at the mountain ridge top. The study showed that buoyancy production acted as an important source of turbulence at lower levels, especially over isolated ridges (regions with warm thermals). The enhanced buoyancy production was attributed to the convergence of thermally driven slope flows and increased heat fluxes. Buoyancy production became invariant with height and was found to become less important for TKE generation at upper levels. Shear production of TKE was also shown to be a major contributor to TKE within the CBL despite weak CBL winds. The investigation found that shear production was due to the downward transport of momentum from the upper-level winds into the CBL. This process occurred when the air below the ridge top, being well-mixed due to surface heating, and the air above ridge top, being well-mixed due to shear instability, approached the same potential temperature. These conclusions are consistent with the study by Lenschow et al. (1979), which found mixing above topography transported higher momentum air from aloft to lower levels, increasing the generation of TKE through shear production. In both studies by Karacostas and Marwitz (1980) and Hahn (1980), dissipation was found to be largest where TKE was driven by shear production.

3.3 Experimental data set

Measurements in this study were collected by a Navy Twin Otter (TO) over and around the isolated Granite Peak, Utah (elevation $\approx$ 2159 m MSL; length $\approx$ 10 km; base width $\approx$ 1.5 km; ridgetop height $\approx$ 800-900 m) during the MATERHORN campaign in the fall of 2012 (MATERHORN-X; Fernando et al. 2015). The immediate area surrounding Granite Peak is characterized by relatively flat terrain ($\approx$ 1300 m MSL). The average

TABLE 3.1: Flight times of Eastern Slope flight plans on 06Oct_{PM}, 10Oct_{AM}, and 17Oct_{PM} and Granite Peak flight plan on 17Oct_{PM}.

Flight period	**Time (MST)**
06Oct_{PM} ESLP	$1702 - 1722$
10Oct_{AM} ESLP	$1202 - 1219$
17Oct_{PM} ESLP	$1649 - 1702$
17Oct_{PM} GRNT	$1621 - 1634$

TO speed was 50 m s^{-1} and aircraft measurements include *in-situ* 10 Hz observations of horizontal and vertical wind velocity components (u, v, and w), potential temperature (θ), and specific humidity (q). Additionally, TODWL wind profiles were obtained at a vertical resolution of about 50 m (from about 200 m AGL to 2200 m AGL) and a horizontal resolution of about 1500 m to investigate the effects of Granite Peak on the mean flow patterns approximately 120 to 150 minutes before the *in-situ* measurements. Airborne observations are available from seven flights on five days in October 2012: 06 October (06Oct_{PM}), the morning of 07 October (07Oct_{AM}), the afternoon of 09 October (09Oct_{PM}), the morning of 10 October (10Oct_{AM}), the morning of 14 October (14Oct_{AM}), the afternoon of 14 October (14Oct_{PM}), and the afternoon of 17 October (17Oct_{PM}). Part I gives a further description of Granite Peak, surrounding terrain, flight data-set, and flight periods and regions.

In this study, we focus on selected observations from the Eastern Slope flights on 06Oct_{PM}, 10Oct_{AM}, and 17Oct_{PM} and the Granite Peak flight on 17Oct_{PM}. During these flight periods, significant TKE maxima were observed over the Eastern Slope and Granite Peak, and legs were flown at multiple heights. These two factors made it possible to provide estimations of the TKE budget terms over and around Granite Peak within and above the CBL. The flight paths and flight times during each of these periods are given in Fig. 3.1 and Table 3.1, respectively.

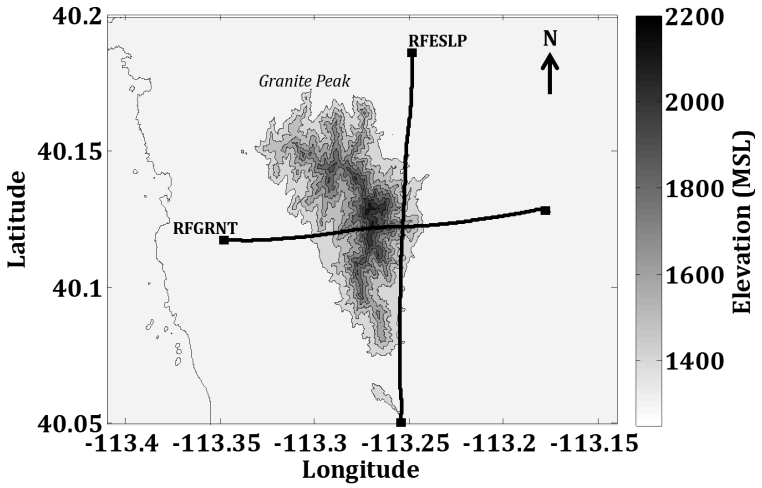

FIGURE 3.1: *Black solid lines* represent the approximate location of research flights (RF) during the 06Oct_{PM}, 10Oct_{AM}, and 17Oct_{PM} used for analysis over the Eastern Slope (RFESLP) and 17Oct_{PM} over Granite Peak (RFGRNT). Granite Peak is centered.

3.4 Methods and approach

3.4.1 Determination of TKE budget terms

The first term on the right side of Eq.(2) is the shear production term, $\tau/\rho \cdot \partial U/\partial z$, which can be estimated using a combination of aircraft and TODWL observations. The buoyancy production term, $g\ \overline{w'\theta_v'}/\overline{\theta_v}$, can be estimated by *in-situ* aircraft measurements. The buoyancy term can be a source or a sink of TKE, depending on the sign of the vertical heat flux. The final term in Eq.(2), ϵ, is the rate of dissipation of TKE to internal energy. Also known as the eddy dissipation rate, ϵ can be calculated from *in-situ* aircraft observations.

The remaining terms in Eq. (2) (not calculated), are the pressure transport, and vertical transport terms. The pressure transport term, $\partial/\partial z \cdot 1/\rho \cdot \overline{w'p'}$, represents the transfer of turbulent energy in space due to pressure fluctuations. This term is the least understood of the TKE budget terms, and cannot be easily calculated from aircraft observations because of the difficulty of measuring small perturbations in pressure as well as large vertical spacing between flight legs (Karacostas and Marwitz 1980; Hahn 1980). The third term in Eq.(2), $\partial/\partial z \cdot \overline{w'e}$, is the vertical transport of TKE which usually has large scatter (Lothon et al. 2003; Hahn 1980). The airborne observations do

not allow accurate estimation of these terms. By neglecting the pressure transport and vertical divergence terms the TKE budget equation, Eq. (2) now becomes:

$$0 = \frac{\tau}{\rho}\frac{\partial U}{\partial z} + g\frac{\overline{w'\theta_v'}}{\overline{\theta_v'}} - \epsilon \tag{3.2}$$

The remaining terms in this equation are shear, buoyancy, and dissipation respectively.

The turbulent fluctuations in Eq. (3), are determined by the same method as in Part I of this study. A 500 m moving average is subtracted from the wind velocity and potential temperature series to get the fluctuations of u', v', w' and θ'. These fluctuations are then used to estimate the TKE budget terms.

The estimation of the shear production term is subject to several challenges. The term requires the calculation of wind shear and the Reynolds stress (momentum flux) at each flight level. Previous investigations over mountainous and flat terrains (e.g. Chou et al. 1986; Hahn 1980, Karacostas and Marwitz 1980) have used either radiosonde or *in-situ* flight observations to estimate the vertical wind shear. These studies have noted that there are uncertainties in the estimate of the shear since the vertical spacing of flight legs used to calculate shear can be large. Also, the location of radiosondes and flight observations do not always correspond. Here, we estimate vertical wind shear from airborne Doppler wind lidar profiles. Estimation of shear from TODWL alleviates some of the uncertainties since TODWL provides a comprehensive visualization of the flow at the level of flight observations used to calculate the shear term. Fig. 3.2 gives a comparison of vertical wind shear estimated from Doppler wind lidar observations over the Eastern Slope and radiosonde observations over the Sagebrush during the 10Oct_{AM} flight period. It is clear that the radiosonde observations are not able to sufficiently capture the spatial variability of the vertical wind shear, which are captured by using TODWL observations.

Note that there are a few considerations when estimating shear production from TODWL. The TODWL observations and *in-situ* observations are separated temporally from the *in-situ* measurements by as much as 120 to 150 minutes and spatially by as much as 500 to 1000 m. In addition, the horizontal resolution of TODWL (1.5 km)

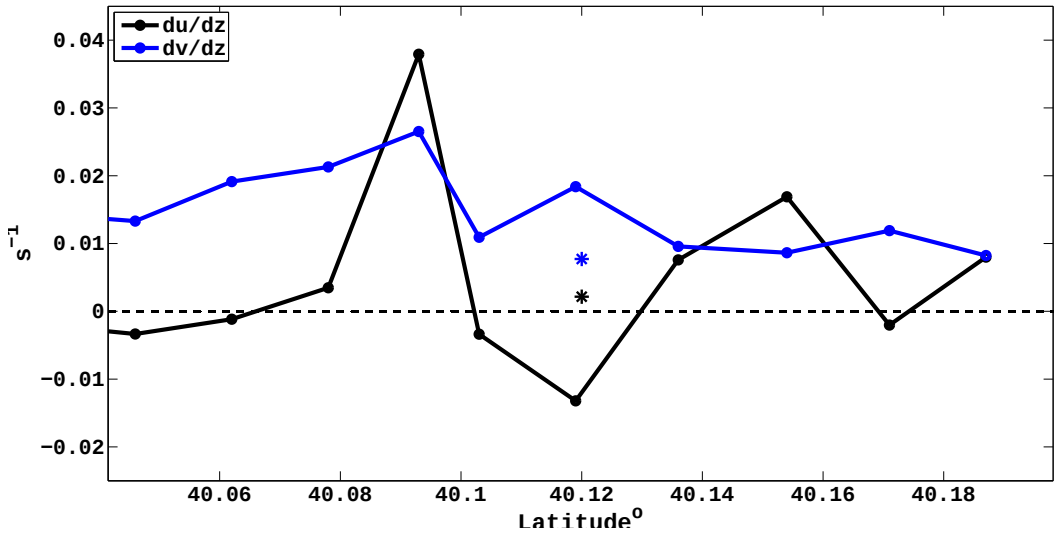

FIGURE 3.2: Comparison of vertical wind shear ($\partial u/\partial z$ and $\partial v/\partial z$) calculated at the lower flight level during the 10Oct_{PM} period from TODWL vertical wind profiles (*solid lines*) over the Eastern Slope and radiosonde observations (*stars*) over the Sagebrush.

may not be sufficient to capture small-scale variations in shear that are characteristic of heterogeneous flow over complex topography. Nonetheless, observations from TODWL still provide a more spatially comprehensive representation of shear than what could be estimated from *in-situ* airborne or radiosonde observations.

The Reynolds stress, $\tau = (-\overline{\rho}\overline{u'w'}^2 - \overline{\rho}\overline{v'w'}^2)$, is estimated from fluctuations of the u', v', and w' components as observed by vertically aligned aircraft flight legs. The series of τ is then averaged, $\overline{\tau}$, using a 500 m running mean. The vertical wind shear is estimated as follows. Using TODWL observations, TODWL wind profiles that are in the same region as the low-level *in-situ* flights were chosen for analysis. In each TODWL vertical wind profile, $\partial u/\partial z$ and $\partial v/\partial z$ is estimated at a vertical resolution of 50 m and then averaged over a 200 m layer containing each flight level of interest (flight leg centered). This gives an estimate of the $\partial\overline{u}/\partial z$ and $\partial\overline{v}/\partial z$ at each flight level every 1.5 km, which is the approximate horizontal resolution of TODWL observations.

Buoyancy production of TKE is estimated using aircraft measurements of θ_v and w. The term $\overline{\theta_v}$ is estimated from a 500 m moving average of θ_v across flight legs. The eddy dissipation rate (ϵ) can be determined in different ways. Two different approaches were used to provide some information on the uncertainty of this term. We choose one of these methods for further calculations and present the estimation of dissipation using

this method.

The first approach consists of finding the inertial subrange, also known as the eddy dissipation range, from fitting the w spectra calculated for each flight leg d with a -5/3 slope. The eddy dissipation range is taken where the spectra and -5/3 slope are parallel (e.g. Večenaj et al. 2012; Jiang et al. 2010). For our cases, the eddy dissipation range resides in scales of motion between 25m and 200m (2-0.25 Hz) (Fig. 3.3). By considering the w variance in this range, eddy dissipation can be calculated as (e.g. Stull 1988):

$$\epsilon = \left[\frac{\lambda^{5/3} S_i(\lambda)}{\alpha}\right]^{3/2} \tag{3.3}$$

Where λ, $S_i(\lambda)$, and α_w are the wavelength, power spectrum, and Kolmogorov constant for the vertical velocity component, respectively. To calculate a spatial series of ϵ, an estimation of the variance is completed as follows. The w time series for each flight leg is linearly detrended and then broken into segments equal to 500m in length (100 data points). In each 500m segment, Fast Fourier Transform (FFT) spectra of the w component are calculated, using windows of 64 data points. Then, the variance in the inertial subrange is calculated by integrating the spectral energy between 2-0.25 Hz (length scales 25-200 m). Using Eq. (4), with the constant $\alpha_w = 0.50$ (e.g. Lothon et al. 2003), a spatial series of eddy dissipation ϵ at a horizontal resolution of 500 m is obtained.

The second approach to calculate dissipation consists of estimating the variance at each observation point by applying a high-pass Butterworth filter to the w time series so that only frequencies between 2-0.25 Hz are passed and, then, squaring the terms (Hahn 1980). Dissipation is estimated using the w variance in this range:

$$\epsilon = \frac{2\pi}{V_a}\left[\frac{S_i(\lambda)}{\alpha}\right]^{3/2} \tag{3.4}$$

Where $S_i(\lambda)$ is the variance accounted for in the inertial subrange, V_a is the average true airspeed, and α is the Kolmogorov constant equal to 0.50. Note that a value for dissipation is given for each observation point. Then, the dissipation is smoothed, using a moving average of 500 m.

Both approaches to estimate dissipation correspond well and differ within $\approx 20\%$. In

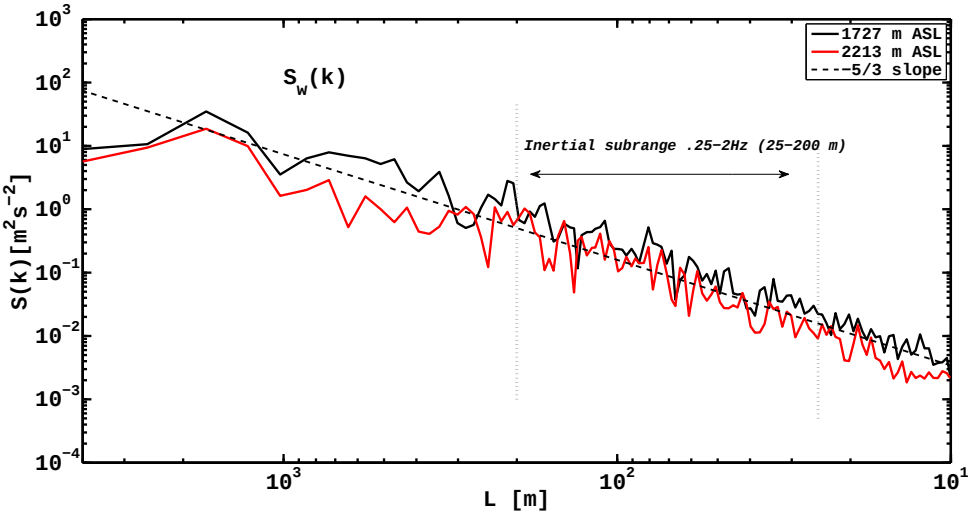

FIGURE 3.3: Power spectra of vertical velocity component from two flight legs over the Eastern Slope on 06Oct_{PM}. *Dashed line* represents the -5/3 slope. Vertical *dotted lines* represent the boundaries of where the w spectra is parallel to the -5/3 line (2-0.25 Hz)

the remainder of this study, we present dissipation estimated from the method given by Hahn (1980). We focus on this method because it provides an estimation of dissipation at each observation point and is consistent with how we estimate the other TKE budget terms.

3.5 Results and discussion

In the following section, we first describe the ambient conditions during each of the flight periods. Second, we attempt to explain the processes responsible for the observed TKE field and the associated maxima that were identified over the Eastern Slope during the 06Oct_{PM}, 10Oct_{AM}, and 17Oct_{PM} periods and over Granite Peak during the 17Oct_{PM} period. For each flight period, the general flow structure and stability using TODWL and *in-situ* aircraft observations are given. The spatial distribution of the shear, buoyancy, and dissipation terms of the TKE budget equation along the relevant flight tracks is presented. The processes important for the observed TKE structure are discussed using TODWL and *in-situ* observations. Third and last, a conceptual discussion of the effects of dynamical and thermodynamical processes on the generation of TKE in and above the mountain CBL is presented.

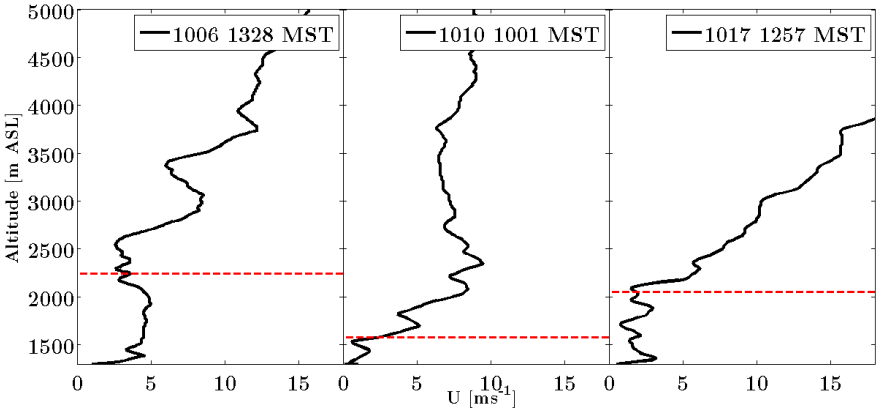

(a) Wind speed

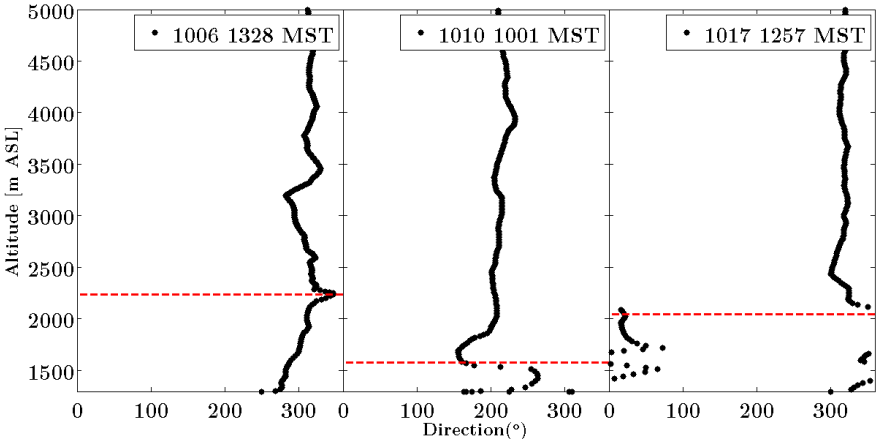

(b) Wind direction

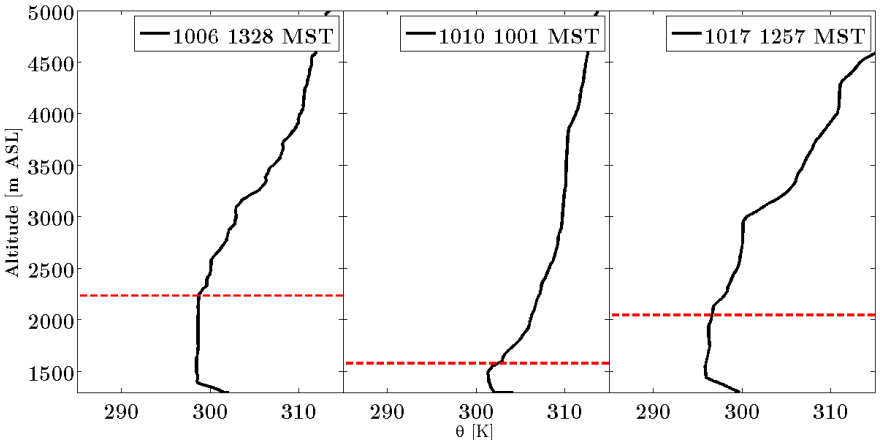

(c) Potential temperature

FIGURE 3.4: Vertical profiles of a.) wind speed, b.) wind direction, and 3.) potential temperature derived from radiosondes launched over the Sagebrush (3 km east of Granite Peak). The *red dotted line* represents *zi* estimated from radiosonde observations.

TABLE 3.2: Ambient conditions during the $06Oct_{PM}$, $10Oct_{AM}$, and $17Oct_{PM}$flight periods. CBL wind and shear measured from 1300-zi, Wind and shear above CBL $zi - 2500$ m MSL. Surface sensible heat (H) and stability measured 5 km to the west of Granite Peak.

Flight period	**CBL wind (m s^{-1})**	**Wind above CBL (m s^{-1})**	**Wind direction**	**CBL shear (s^{-1})**	**Shear above CBL (s^{-1})**	**H (W m^{-2})**	**Surface stability ($-z/L$)**
$06Oct_{PM}$	$2-3$	$4-6$	330°	10^{-4}	10^{-3}	120	66
$10Oct_{AM}$	$5-7$	$8-10$	200°	10^{-3}	10^{-3}	90-100	55
$17Oct_{PM}$	$3-4$	$5-15$	315°	10^{-4}	10^{-3}	90-100	30

3.5.1 Ambient conditions

The ambient conditions during the $06Oct_{PM}$, $10Oct_{AM}$, and $17Oct_{PM}$ flight periods are summarized in Fig. 3.4 and Table 3.2. The periods can be categorized into two types of CBLs that are expected to be different in the amount of shear generated turbulence. One type, represented by $06Oct_{PM}$ and $17Oct_{PM}$, illustrates a CBL with weak winds and shear within the CBL and relatively strong wind shear at the CBL top. The other type, represented by $10Oct_{AM}$, illustrates relatively strong wind speed and shear throughout the CBL.

The $06Oct_{PM}$ flight period is characterized by relatively weak winds (2-3 m s^{-1}) and north-northwesterly flow within the CBL (1300-2100 MSL) (Fig. 3.4a and 3.4b). Wind shear within the CBL is relatively small ($10^{-4}s^{-1}$). However, in the layer between 1900 to 2500 m MSL, wind speed increases from 1 to 6 m s^{-1} and is characterized by larger shear ($10^{-3}s^{-1}$) than within the CBL (Fig. 3.4b). Relatively unstable conditions ($-z/L \approx 66$ and H ≈ 120 W m^{-2}) are present during the $06Oct_{PM}$ period. In addition, the CBL is well-developed and deep compared to the other flight periods (3.3c). Less unstable conditions exist during the $10Oct_{AM}$ flight period (Table 3.2), and the CBL is also relatively shallow compared to $06Oct_{PM}$ and $17Oct_{PM}$ (Fig. 3.4c). This is mainly because this flight period was flown earlier in the day (1151-1318 MST). Observations show that the CBL mean wind is south-southwesterly and relatively strong, with 2 m s^{-1} near the surface, increasing to 8-10 m s^{-1} at 2500 m MSL (Fig. 3.4a). Wind shear within the CBL is 10^{-3} s^{-1} (Table 3.2). During the $17Oct_{PM}$ flights, surface conditions are

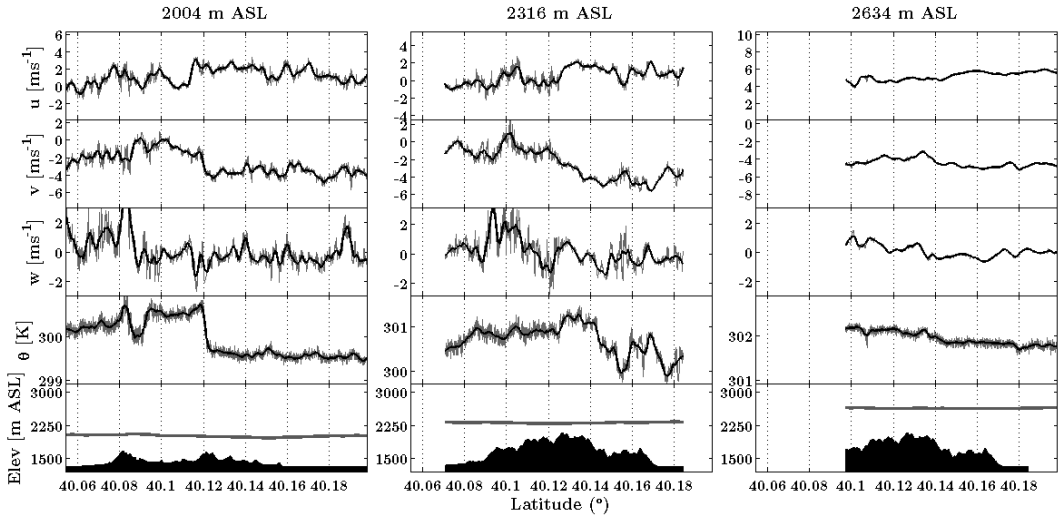

FIGURE 3.5: Airborne *in-situ* observations of u, v, w, and θ on 06Oct_{PM} over the Eastern Slope. Elevation cross sections are given for each flight leg

unstable ($-z/L \approx 30$ and H $\approx$ 100 W m^{-2}), and winds within the CBL are on the order of 3-4 m s^{-1} and north-northwesterly. However, winds above *zi* ($\approx$ 2000 m MSL) increase from 5 to 10 m s^{-1} at 3000 m MSL (Fig. 3.4a). These flow characteristics create a layer of relatively weak shear (10^{-4} s^{-1}) topped by a layer of larger shear (10^{-3} s^{-1}).

3.5.2 Eastern Slope: $\mathbf{06Oct_{PM}}$

The mean flow structure over the Eastern Slope is given in Fig. 3.5 and 3.6. The wind is 4-6 m s^{-1} north of a ridge in the underlying terrain (40.14° − 40.20° N). Weaker winds at 2-3 m s^{-1} exist over a ridge top (40.06° − 40.14° N) (Fig. 3.5 and 3.6). Considerable vertical uplift (1.5-3 m s^{-1}) and increased variability in the horizontal wind velocities exists over terrain at the lower and mid levels. The wind shear derived from the TODWL vertical wind profiles within the CBL (< 2200 m MSL) is relatively small $10^{-4}s^{-1}$. However, there is greater shear on the order of $10^{-3}s^{-1}$ in the layer 2200-2600 m MSL. Estimates of *zi* show the CBL varied between 2100 and 2300 m MSL over the Eastern Slope. The lower level flight flew within the CBL, while the mid-flight flew within the CBL over the ridge top. The upper flight flew above *zi*.

The TKE budget analysis over the Eastern Slope on 06Oct_{PM} is given in Fig. 3.7.

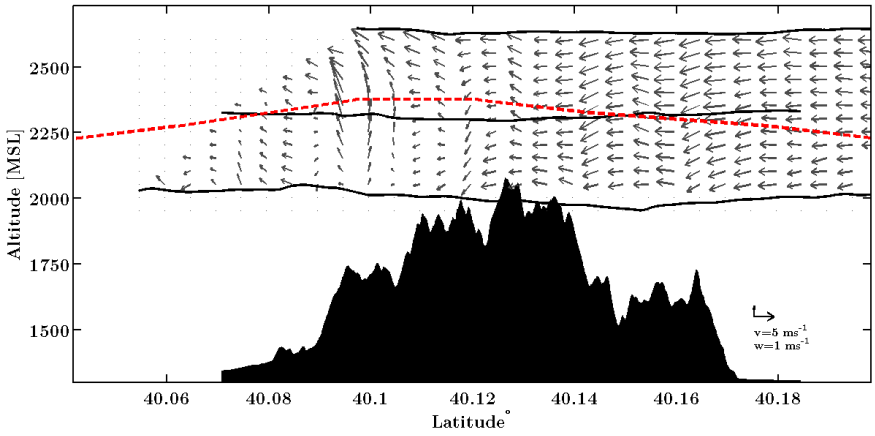

(a) *In-situ* $\overrightarrow{VW}$ wind vectors

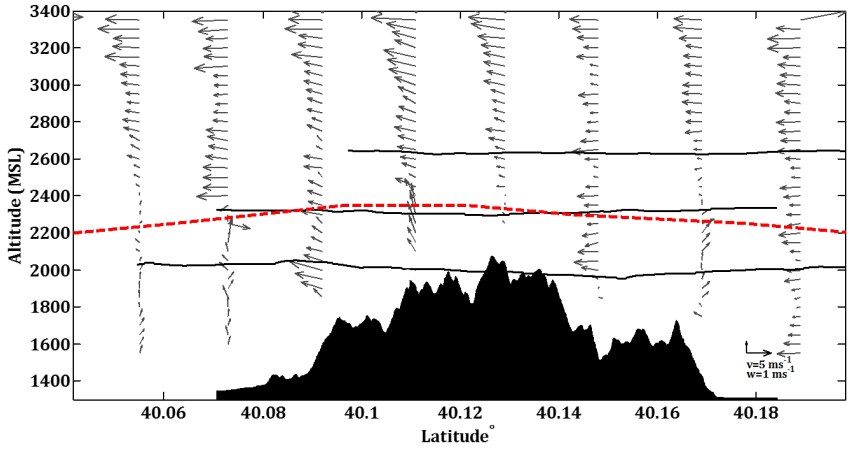

(b) TODWL $\overrightarrow{VW}$ wind vectors

FIGURE 3.6: $\overrightarrow{VW}$ wind vectors from a.) airborne *in-situ* observations and b.) TODWL vertical wind profiles on 06Oct_{PM} over the Eastern Slope. *Dotted red line* represents the *zi* estimated from TODWL aerosol structure, *in-situ* airborne, and TKE observations.

In Part I of this study, the largest values of TKE and TKE maxima were found between 40.06°-40.13° N at the lower and mid flights. Buoyancy production is of higher magnitude in the lower levels at 40.08° N and becomes more neutral in the mid-level flight leg (where it even tends to compensate slightly for shear production). The positive buoyancy at the lower flight level is associated with increased heat fluxes and upward motions (> 2 m s^{-1}) (Fig. 3.5 and 3.6). Shear production is generally small and positive but has a few relatively large positive maxima at the lower (40.08° N) and mid-flight levels (40.10° N) . Negative heat and momentum fluxes are evident in these regions, indicating entrainment of FA air into the CBL. The mid-flight level flew near *zi*, so the influence of

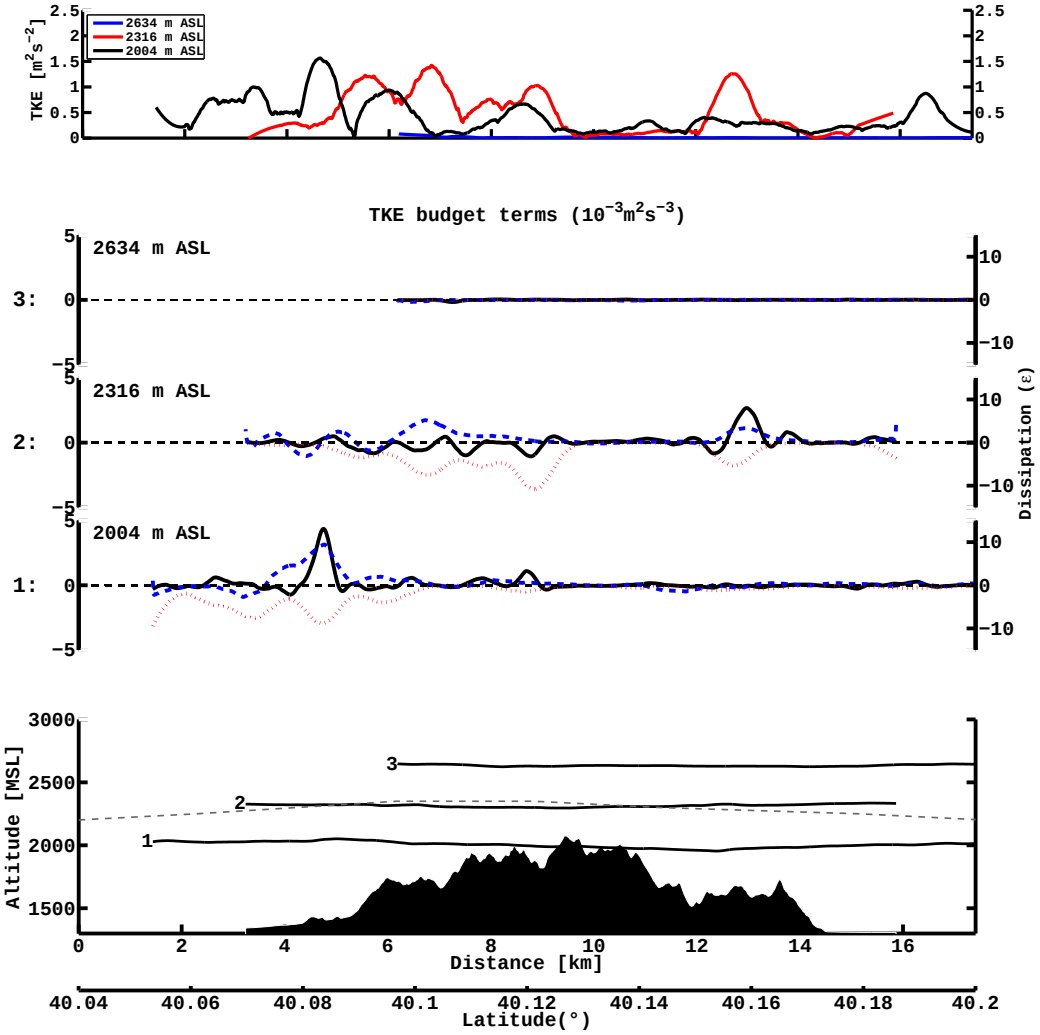

FIGURE 3.7: TKE (top) and budget terms over the Eastern Slope on 06Oct_{PM}. *Black solid line* represents buoyancy, *blue solid line* is shear production, and the *red dotted line* is ϵ using Hahn (1980). *Gray dashed line* is *zi* estimated from TODWL and TKE observations.

entrainment processes is likely (Fig. 3.5 and 3.6). The local maximum in TKE, buoyancy, and shear at the mid-flight at 40.16° N is associated with a locally warm region of air (+ 0.75 K) and increased uplift (Fig. 3.5). These characteristics signal the edges of a thermal (Lenschow 1970). Past investigations have noted that thermals are efficient at transporting heat and momentum through the CBL (Moeng and Sullivan 1994). The transport of heat and momentum by the thermal is responsible for production of TKE in this region.

Some of the local TKE maxima at the lower and mid-flight legs are not well explained

by buoyancy or shear production. The TKE maxima that are not justified by shear or buoyancy production correlate well with the observed region of increased vertical velocity (Fig. 3.5). Dissipation corresponds well to buoyancy, shear production, and TKE and is the largest of the terms.

3.5.3 Eastern Slope: $\mathbf{10Oct_{AM}}$

Wind speed over the Eastern Slope increases from 5 m s^{-1} to 10 m s^{-1} in the layer between 2100 and 2500 m MSL. TODWL and *in-situ* observations indicate there is strong shear ($10^{-3}s^{-1}$) through this layer. Cross-sectional plots of the mean flow structure and airborne observations suggest the presence of a wave-breaking phenomenon to the lee of a small ridge at mid and upper flight levels (Fig. 3.8 and Fig. 3.9). In this region, flight observations indicate strong vertical velocities ($\pm$ 3 m s^{-1}) and large deviations in the horizontal wind velocities and potential temperature just downwind of a small ridge (40.13° N) (Fig. 3.8 and Fig. 3.9). The wave breaking region is not evident at the lower flights. At the lower level, strong vertical velocities (1-2 m s^{-1}) are associated with a large variability in the horizontal wind (Fig. 3.8). The estimates of *zi* show that the CBL top varied between 1650-1850m MSL over the Eastern Slope (Fig. 3.9). This means that the lower level flight flew within the CBL and near *zi*. The mid and upper flights flew above *zi*.

Cross-sectional plots of the various TKE parameters are displayed in Fig. 3.10. In Part I of this study, TKE maxima are found at the lower flight between $40.07° - 40.09°$ N and $40.1° - 40.15°$ N. In the lower levels, TKE is primarily due to shear production. However, buoyancy contributes to TKE production over a small ridge in the underlying terrain (40.13° N). There is a local maximum in shear production at 40.08° N at this level. It is not associated with the small ridge top but does correspond with TKE maxima (2.0 m^2 s^{-2}). TKE maxima (2.3-2.5 m^2 s^{-2}) are also evident at the mid and upper flights in the wake of a small ridge ($40.1° - 40.15°$ N). The major contribution to TKE at the mid-flight level is from shear production. Shear production is small and does not significantly contribute to TKE at the upper flight. In contrast, buoyancy has a positive maximum in this region, indicating it aided in TKE generation. This is a unique feature compared to the upper level flights on other flight days. Typically,

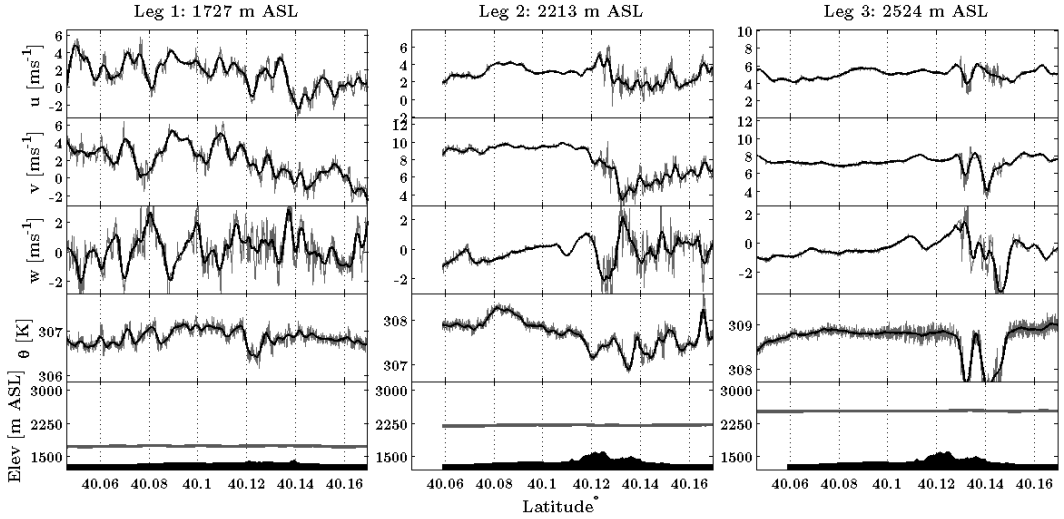

FIGURE 3.8: Airborne *in-situ* observations of u, v, w, and θ on 10Oct_{AM} over the Eastern Slope. Elevation cross sections are given for each flight leg

because of stable stratification, buoyancy destroys TKE at these levels (above the CBL top). Dissipation compensates for the production of TKE from buoyancy and shear. However, at some points along the lower flight, shear and buoyancy production are negligible, but dissipation and TKE remains significant.

Waves are important for turbulence when they break. Often, wave-breaking regions are characterized by turbulent billows, increased shear instability, and increased generation of TKE. To determine if conditions were favorable for the existence of turbulent billows at the mid and upper flights, we estimated the Richardson number at these levels. Previous works have noted wave-breaking regions that are characterized by a low Richardson number (< 1) (e.g. Jiang et al. 2010; Jiang and Doyle 2004; Hahn 1980; Miles 1961; Howard 1961). *In-situ* airborne observations have revealed detailed structure of the billows over complex terrain (e.g., Jiang et al. 2010). The criteria for their onset is considered to be a Richardson number $R < .25$ (R_c). However, the formation of turbulent billows can also be associated with a Richardson number less than unity (Jiang and Doyle 2004). In this study, the estimated Richardson number is found to be larger than R_c but less than unity ($R < 1$) at the mid and upper flights.

Observations reveal that the wave-breaking/turbulent billows are associated with relatively strong downward motion of stable (negative heat flux) and higher momentum

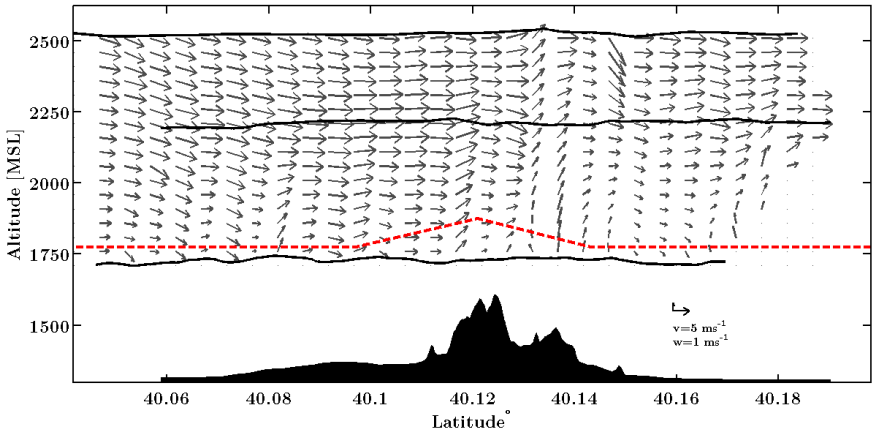

(a) *In-situ* $\overrightarrow{VW}$ wind vectors

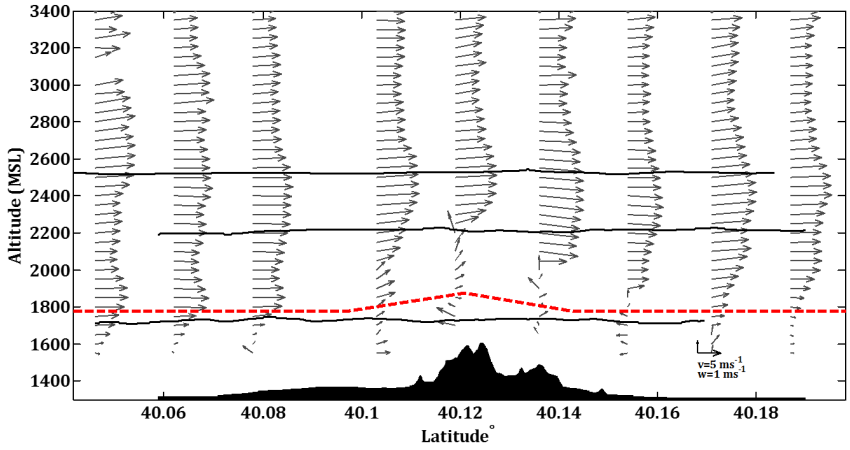

(b) TODWL $\overrightarrow{VW}$ wind vectors

FIGURE 3.9: $\overrightarrow{VW}$ wind vectors from a.) airborne *in-situ*observations and b.) TODWL vertical wind profiles on 10Oct_{AM} over the Eastern Slope. *Dotted red line* represents the *zi* estimated from TODWL aerosol structure, *in-situ* airborne, and TKE observations.

(negative momentum flux) air at the mid and upper flights (Fig. 3.8). In this region, the air is stable and turbulence is strong (TKE = 2.25 m^2 s^{-2}) (Fig. 3.10). Smaller momentum fluxes are associated with this feature at the upper-level, and shear production is less significant. This is because there is less small-scale variability (< 500 m) in wind velocity field at the upper-level compared to the mid-level flight. Interestingly, there is a symmetrical sink-source of buoyancy associated with forced flow and the wave-breaking region at the upper flight. The contribution of buoyancy to TKE at this level is attributed to the descending of the upper-level flow, which is potentially warmer and rising in this region. The mid and upper-level flight observations in this study suggest

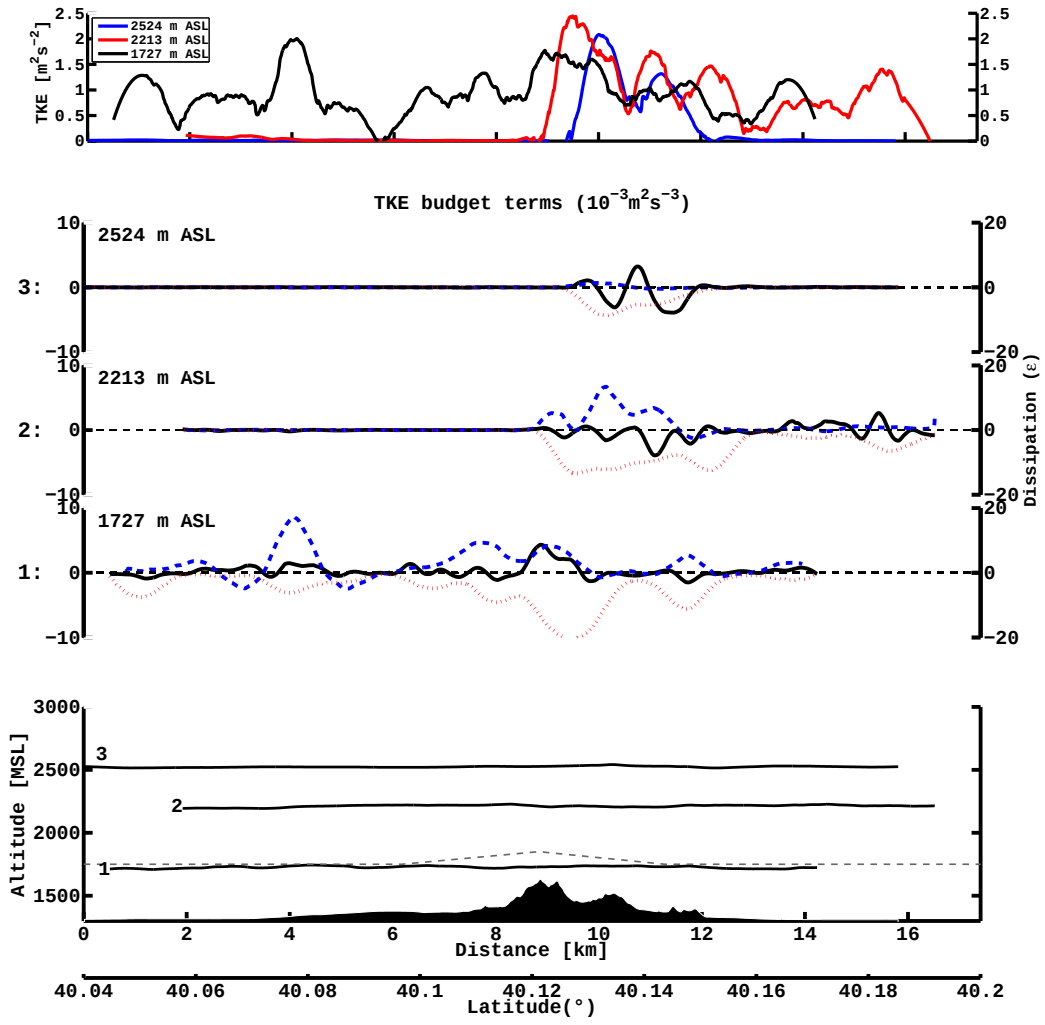

FIGURE 3.10: TKE (top) and budget terms over the Eastern Slope on 10Oct_{AM}. *Black solid line* represents buoyancy, *blue solid line* is shear production, and the *red dotted line* is ϵ using Hahn (1980). *Gray dashed line* is *zi* estimated from TODWL and TKE observations.

that the wave-breaking feature has a wavelength of about 2.0 km and an amplitude of ≈ 300 m. The wavelength, local stability, and strong momentum fluxes are consistent with the observed structure and size of wave-breaking regions noted in previous observations during conditions with moderate to strong winds (> 7 m s^{-1}) (Jiang et al. 2010; Hahn 1980).

The lower flight seems to be unaffected by the wave feature seen at mid and upper flight levels. As seen in Fig. 3.8 and 3.9, the interaction of the mean flow and the underlying small ridge produces increased vertical uplift over the ridge crest (40.12° – 40.14° N). Increased sensible heat fluxes are observed (not shown), suggesting that uplift

over the ridge top aided in the vertical transport of warm air near the ridge slopes to an area above the ridge. A local maximum in buoyancy production and TKE (1.5 m^2 s^{-2}) (Fig. 3.10) is associated with this region of increased vertical motion (Fig. 3.8 and Fig. 3.9). There are other regions of strong vertical velocities (± 2 m s^{-1}) and increased variability in the horizontal wind and potential temperature at the lower flight not associated with the ridge top. Relatively significant negative momentum fluxes exist in these regions and suggest the exchange of higher momentum FA air down into the CBL (e.g Fedorovich and Conzemius 2008; Sullivan et al. 1998; Moeng and Sullivan 1994; Caughey and Palmer 1979) (Fig. 3.8). Dissipation correlates well with the observed TKE and is the largest of the terms.

3.5.4 Eastern Slope: $\mathbf{17Oct_{PM}}$

Over the Eastern Slope, the horizontal flow is on the order of 2 to 4 m s^{-1} at the lower and mid-flight levels and 11 m s^{-1} at the upper flight level (Fig. 3.11 and 3.12). This large increase in wind speed produces a layer (2200-2600 m MSL) of relatively large shear ($10^{-3}s^{-1}$). There is increased vertical velocity over a ridge top in the underlying terrain (40.13° N) as well as increased variability in the horizontal wind at both the mid and upper levels (Fig. 3.11). Estimates show that *zi* varied between 2100 to 2300 m MSL over the terrain during the $17Oct_{PM}$ flight period (Fig. 3.12). This means the lower and mid-level flight legs flew within the CBL mixed layer or near *zi*. The upper-level flight leg flew above the CBL top or near the top of the entrainment zone.

Cross-sectional plots of the TKE budget terms for the $17Oct_{PM}$ Eastern Slope flight period are given in Fig. 3.13. TKE maxima were found over a ridge top between $40.09° - 40.14°$ N in Part I of this study. Shear production is generally positive and corresponds well with the observed TKE field at the three flight levels. Negative buoyancy production and dissipation tend to compensate for it in the lower and upper two flight levels. At the mid-flight level, buoyancy contributes to TKE production over the ridge top (40.13° N).

Shear production correlates well with the observed TKE, indicating shear is the dominant contributor to turbulence. However, a buoyant plume associated with strong vertical velocities exists over the ridge top and significantly contributes to TKE at

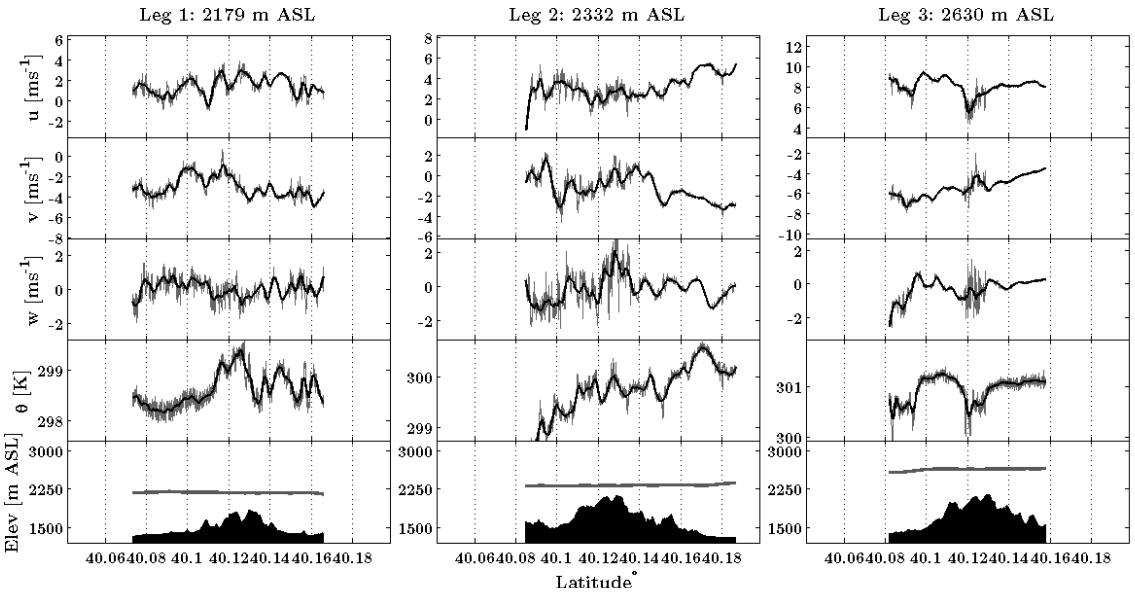

FIGURE 3.11: Airborne *in-situ* observations of u, v, w, and θ on 17Oct_{PM} over the Eastern Slope. Elevation cross sections are given for each flight leg

the mid-flight level (Fig. 3.11 and 3.12). Interestingly, this plume becomes negatively buoyant at the upper flight, which is near the stable layer (Fig. 3.13). The region of negative buoyancy is associated with a large drop in potential temperature (0.75 K) over the ridge top (40.13° N) (Fig. 3.11). Negative momentum fluxes are associated with the region of negative buoyancy, indicating that the interaction of the plume and stable layer caused entrainment of higher momentum FA air downward (Moeng and Sullivan 1994; Caughey and Palmer 1979). At the lower flight, a buoyant plume is not evident. However, negative momentum fluxes and negligible/negative sensible heat fluxes are apparent (Fig. 3.11). The sign of these fluxes corresponds to entrainment processes (Moeng and Sullivan 1994; Caughey and Palmer 1979). It is important to note the increased shear near the CBL top during this period. We suggest that the shear-enhanced the turbulent exchange of higher-momentum upper level between the FA and CBL over the ridge top (Fedorovich and Conzemius 2008; Conzemius and Fedorovich 2006a). This process appears to influence the shear production of TKE.

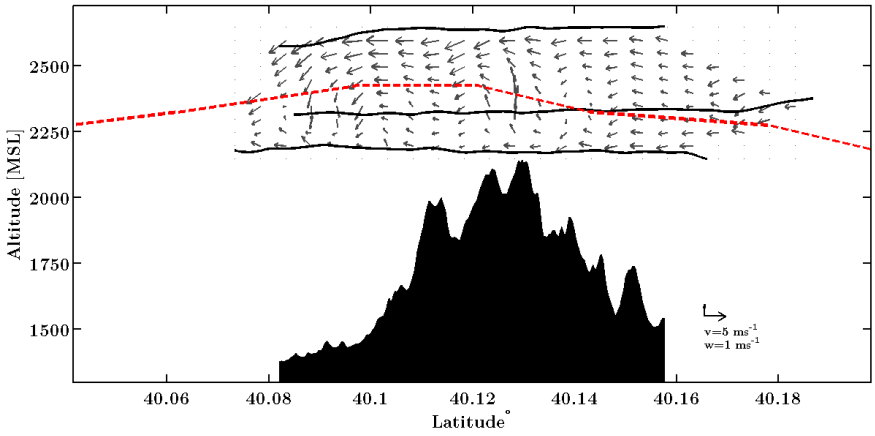

(a) *In-situ* $\overrightarrow{VW}$ wind vectors

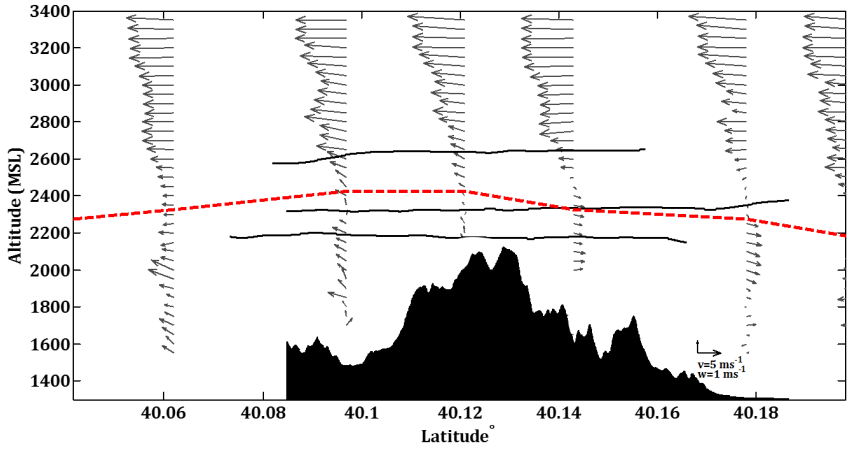

(b) TODWL $\overrightarrow{VW}$ wind vectors

FIGURE 3.12: $\overrightarrow{VW}$ wind vectors from a.) airborne *in-situ* observations and b.) TODWL vertical wind profiles on 17Oct_{PM} over the Eastern Slope. *Dotted red line* represents the *zi* estimated from TODWL aerosol structure, *in-situ* airborne, and TKE observations.

3.5.5 Granite Peak: 17Oct_{PM}

In-situ airborne observations along flight legs in Fig. 3.14 and TODWL vertical wind profiles in Fig. 3.15 exhibit the mean flow structure over Granite Peak. Most noticeable are the large vertical velocities at the lower to upper flight levels. Increased variability in the horizontal flow over the mountain crest is also evident (Fig. 3.14 and 3.15). The wind speed increases from 2 to 3 m s^{-1} at the lower level to 5 to 7 m s^{-1} at the upper-level. Similar to the Eastern Slope, a layer of increased shear (10^{-3} s^{-1}) exists near the CBL top (2100-2500 m MSL). Estimates of *zi* show that the CBL was terrain

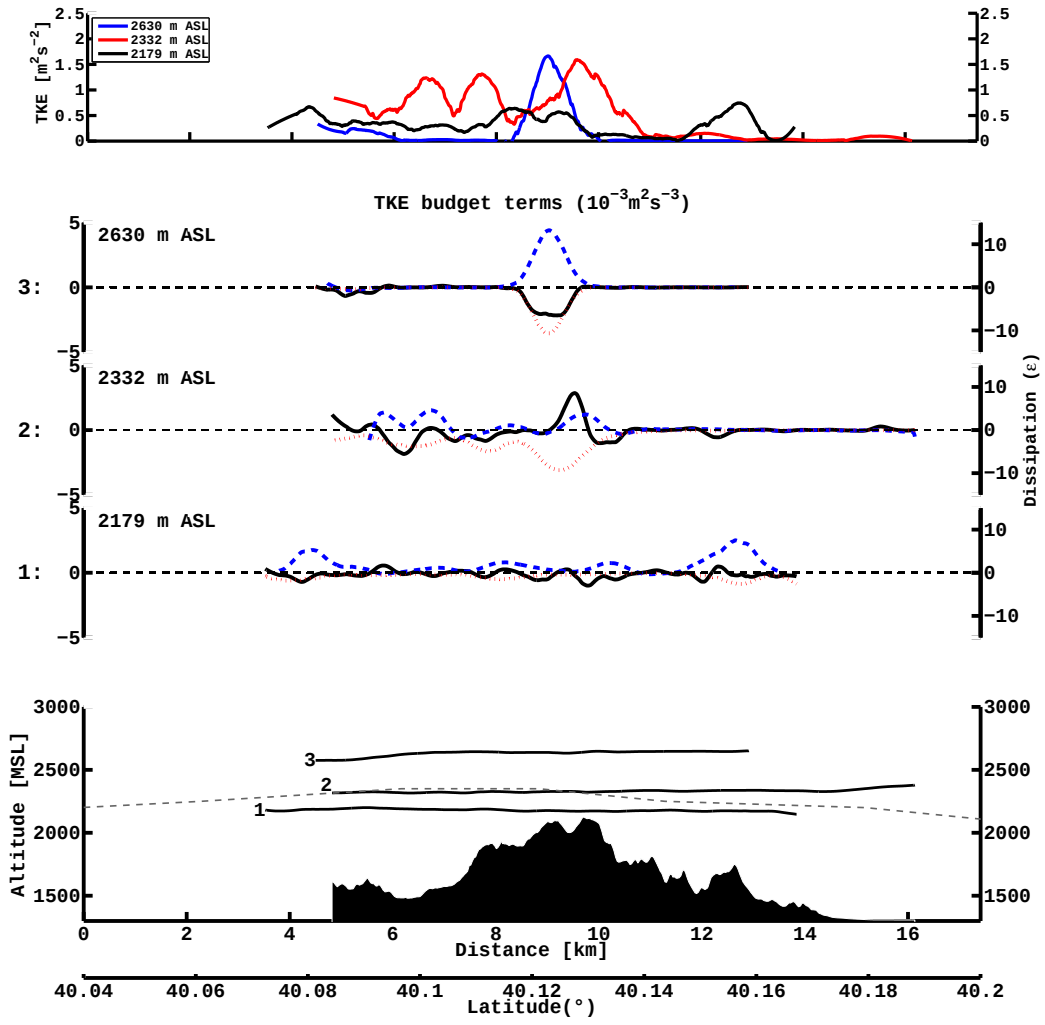

FIGURE 3.13: TKE (top) and budget terms over the Eastern Slope on 17Oct_{PM}. *Black solid line* represents buoyancy, *blue solid line* is shear production, and the *red dotted line* is ϵ using Hahn (1980). *Gray dashed line* is *zi* estimated from TODWL and TKE observations.

following over Granite Peak with $zi \approx 2400$ m MSL over the mountain and 2100 m MSL over the surrounding plains (Fig. 3.15). The lower flight flew within the CBL while the mid-flight leg flew near *zi* and the upper flight flew above *zi*.

The cross-sectional plots of the TKE and associated budget terms over Granite Peak are provided in Fig. 3.16. In Part I, TKE maxima were found along the three flight legs over Granite Peak between $113.31° - 113.21°$ W with maximum TKE centered over the mountain crest at the upper flight (113.26° W). As during the 17Oct_{PM} flights over the Eastern Slope, shear production is the primary contributor to TKE. However, buoyancy production ($113.26° - 113.25°$ W) also contributes to the TKE over the crest of the

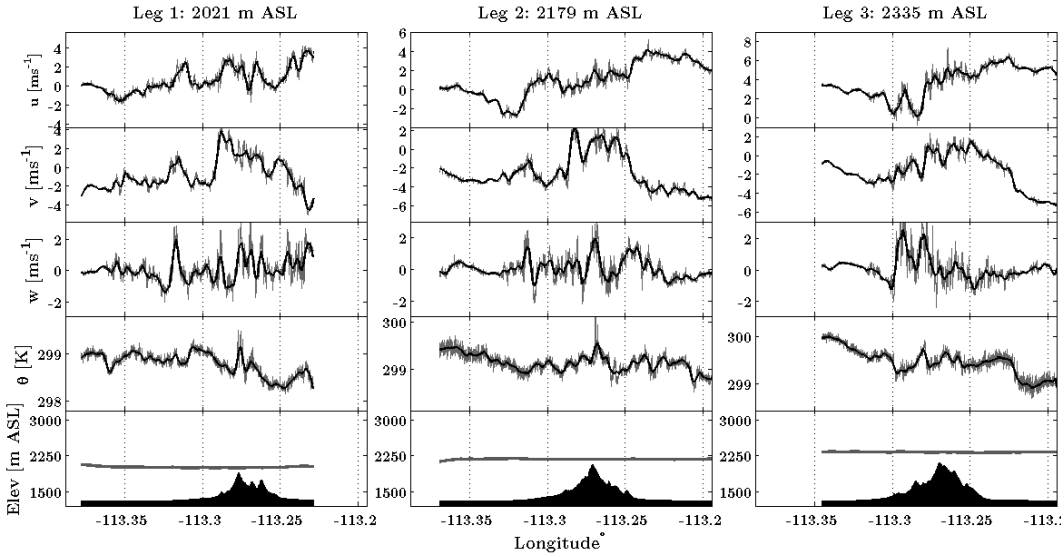

FIGURE 3.14: Airborne *in-situ* observations of u, v, w, and θ on 17Oct$_{\mathrm{PM}}$over the Granite Peak. Elevation cross sections are given for each flight leg

mountain in the lower and mid-levels. The upper-level maximum of TKE occurring over the mountain crest is due to shear production. Buoyancy is negative and acts as a sink of TKE in this region. Dissipation corresponds well to TKE. Not all of the observed TKE is explainable by shear or buoyancy production.

Often "hot spots", or regions where conditions are favorable for strong thermals to form, occur over mountain ridges. Their development is favored by warm and moist air at the lower levels that is transported vertically by upslope flows (e.g. Hahn 1980; Henz 1974). These requirements seem to be satisfied over the mountain crest of Granite Peak. Increased uplift (+ 2 m s^{-1}) (Fig. 3.14 and 3.15), heat fluxes, and larger mixing ratios (q = 2.3 g kg^{-1}), compared to the surrounding environment (1.3 g kg^{-1}), correspond to the large positively buoyant area over mountain crest at lower and mid flights. The convective plume/thermal contributes to TKE at the lower and mid-flight levels but becomes negatively buoyant at the upper flight near the stable layer/entrainment zone where it suppresses TKE (Fig. 3.16). Young (1988) and Greenhut and Singh Khalsa (1987) investigated the interactions of thermals and their environment and found that the interaction of negatively buoyant thermals and the stable layer initiated an exchange of air between the CBL and FA. Although the negative buoyancy acts to suppress the

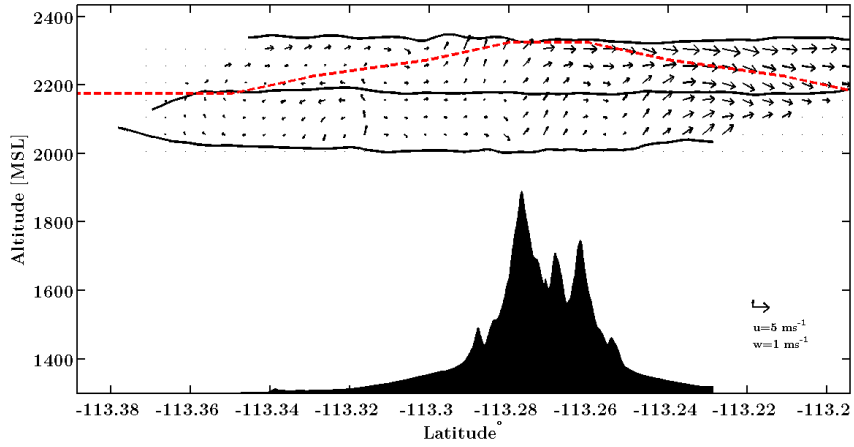

(a) *In-situ* $\overrightarrow{UW}$ wind vectors

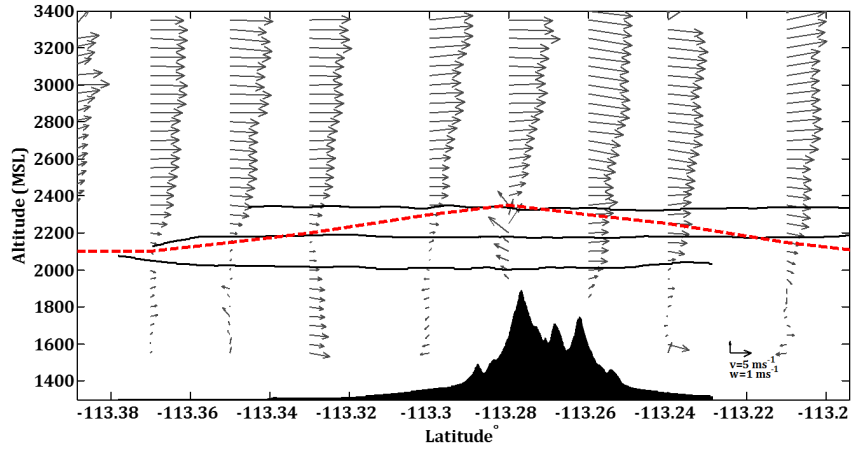

(b) TODWL $\overrightarrow{UW}$ wind vectors

FIGURE 3.15: $\overrightarrow{UW}$ wind vectors from a.) airborne *in-situ* observations and b.) TODWL vertical wind profiles on 17Oct_{PM} over the Granite Peak. *Dotted red line* represents the *zi* estimated from TODWL aerosol structure, *in-situ* airborne, and TKE observations.

development of TKE, entrainment due to the interaction of the thermal and stable layer mixes down faster (higher momentum) upper-level air and increases shear production. Past studies have found similar effects of entrainment on turbulence in the CBL (e.g. Moeng and Sullivan 1994; Boers and Eloranta 1986; Boers et al. 1984 ; Caughey and Palmer 1979).

The effects of entrainment on the generation of TKE by shear production are also noticed at the lower and mid flights. Strong updrafts and downdrafts (-1.5 to 2 m s^{-1}) are associated with increased variability in the horizontal wind velocities and potential temperature at these levels (Fig. 3.14). In addition, regions of moist air (2-2.5

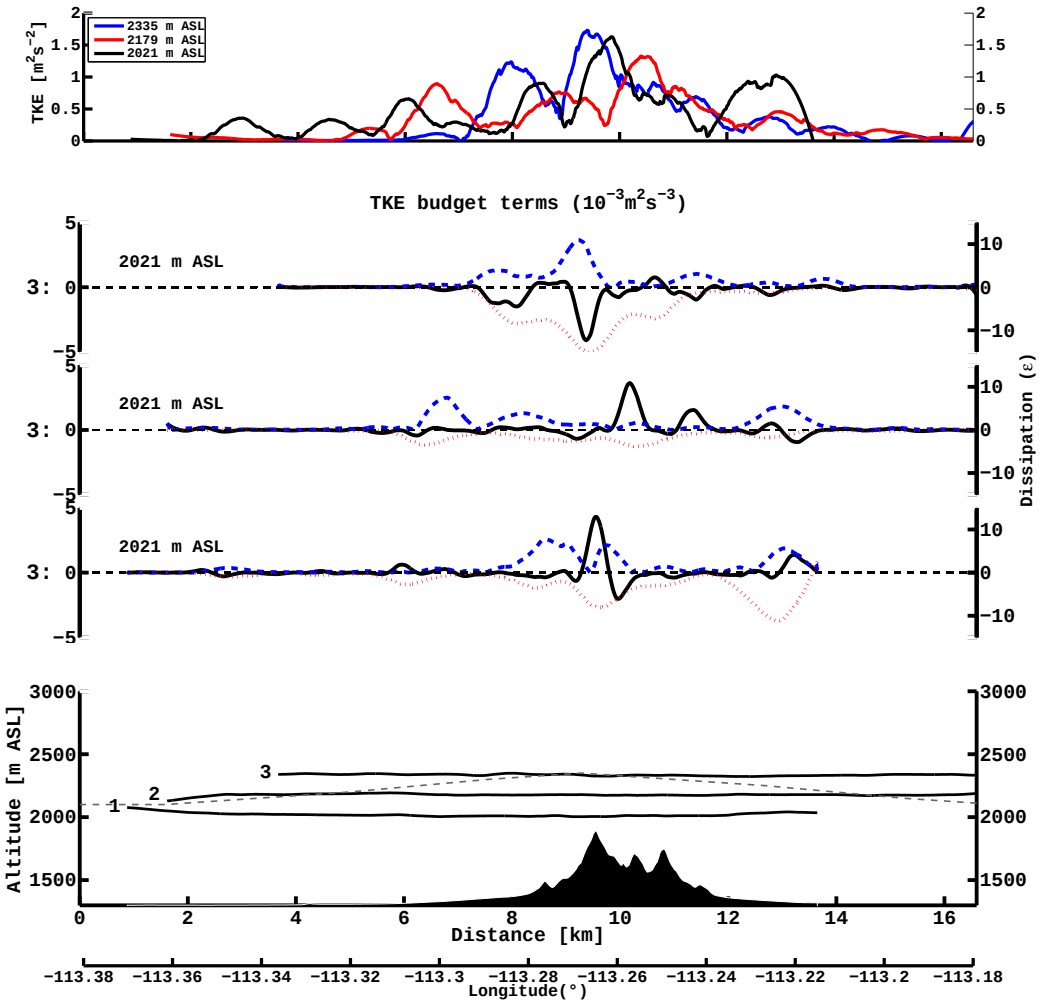

FIGURE 3.16: TKE (top) and budget terms over the Granite Peak on 17 Oct. *Black solid line* represents buoyancy, *blue solid line* is shear production, and the *red dotted line* is ϵ using Hahn (1980). *Gray dashed line* is *zi* estimated from TODWL and TKE observations.

g kg^{-1}), apparently derived from the lower boundary layer, are evident at these levels (not shown). These features suggest the rising and subsequent entrainment of low-level moist parcels of air (e.g. Tennekes 1973; Zeman and Tennekes 1977; Caughey and Palmer 1979; Young 1988; Moeng and Sullivan 1994; Sullivan et al. 1998). Similar to over the Eastern Slope, the increased shear near the CBL top during this period likely enhanced the turbulent entrainment processes evident over Granite Peak (Fedorovich and Conzemius 2008; Conzemius and Fedorovich 2006a).

3.5.6 Conceptual discussion of the mechanisms and sources of TKE

Many of the turbulent features of the boundary layer over the mountains are explainable by various mechanisms specific to mountainous topography and the CBL. A description of TKE without reference to these mechanisms is incomplete. The mechanisms important for the location and development of TKE maxima are discussed in this section.

We encountered two different types of CBLs during our selected flight periods. The first type of CBL occurs during the 06Oct_{PM} and 17Oct_{PM} flights and is characterized by a layer of weak wind and shear within the CBL and a shear driven layer near the CBL top. This is similar to the two-layered CBL structure noted by past investigations in a shear-topped CBL (e.g. Fedorovich and Conzemius 2008; Pino and Vilà-Guerau De Arellano 2008; Conzemius and Fedorovich 2006a. A distinctly different type of CBL exists during the 10Oct_{AM} period. The CBL, in this case, involves strong wind and shear through the depth of the CBL and near the CBL top. Among the processes responsible for influencing the TKE field during these types of CBLs is the transport of higher momentum, upper-level flow downward. Although this feature was noted across both types of CBLs different mechanisms were involved. Analysis of the flow structure, wind velocity, potential temperature field, and spatial variability of the TKE budget terms helped reveal the presence of these mechanisms.

During periods characterized by a shear topped CBL with weak lower level winds (< 5 m s^{-1}), buoyancy production of TKE occurs in localized regions (hot spots) over ridge tops. These regions are associated with rising warm moist, buoyant plumes and with the convergence of upslope flows above terrain. These buoyant plumes provide energy for TKE generation at lower levels but suppress TKE as they become negatively buoyant in the stable layer and entrainment zone. This finding is consistent with previous studies over both flat homogeneous and complex topography (e.g. Wyngaard and Coté 1971; Kaimal et al. 1976; Caughey and Palmer 1979; Hahn 1980).

The interaction of the rising buoyant plumes over the topography and the stable layer generates strong horizontal and downward velocities near the CBL top. Strong horizontal, downward motions near the edges of the plumes pull down pockets of higher momentum and warm air from above the CBL (Sullivan et al. 1998). These pockets of higher momentum and warm air are then scoured off by turbulent motions and entrained

into the CBL. Similar to findings from sheared CBLs over flat terrain, these entrainment processes are enhanced by shear near the CBL top. The enhanced entrainment increases the transport of higher momentum FA air downward (Fedorovich and Conzemius 2008; Pino and Vilà-Guerau De Arellano 2008; Conzemius and Fedorovich 2006a; Conzemius and Fedorovich 2006b; Caughey and Palmer 1979; Zeman and Tennekes 1977; Tennekes 1973; LeMone 1973; Lenschow 1970). Negatively buoyant air (stable) also accompanies the downward transport of upper-level flow and positive shear production. However, the balance between the shear generation of TKE, consumption of TKE by buoyancy, and dissipation maintains turbulence.

Past studies have also noted that the downward transport of upper-level momentum over mountainous terrain can be important for generation of TKE by shear (e.g. Hahn 1980; Lenschow et al. 1979). However, these studies found that it was the transition from a CBL top below mountain top level to above the mountain that initiated the mixing of strong winds from the mountain top to lower levels. The CBLs in this investigation are above topography during the flight periods. Thus, we do not see the same CBL development in our studies. Instead, we show that entrainment and subsequent mixing of higher momentum upper-level flow into the CBL are due to the interaction of localized buoyant plumes generated over topography and the stable layer. This mechanism can be enhanced when increased shear is present near the CBL top or when strong mixing is initiated by the interaction of topography and the ambient flow. Enhanced shear production in the CBL has been found in shear topped CBLs over flat terrain. Studies over complex terrain have yet to detail the effects of this mechanism on TKE production in a CBL.

During periods characterized by moderate lower level flow (5-10 m s^{-1}) and relatively large wind shear, the turbulent regions form downwind of the ridge top above the CBL top. The flow follows the underlying terrain and creates waves that break region on the lee side of a ridge. Shear instability causes turbulence and aids the downward transport of higher momentum and stable air. Past studies have noted these features during conditions with wind speeds $>$ 10 m s^{-1} (e.g., Hahn 1980; Karacostas and Marwitz 1980; Jiang et al. 2010; Jiang and Doyle 2004). However, these features, as well as their effects on the location and development of TKE maxima, have not been investigated

during unstable conditions with winds < 10 m s^{-1}.

In this study, a large part of the TKE maxima can be explained by buoyancy and shear production. However, in certain situations the balance between shear and buoyancy production in some regions does not correspond to the observed magnitude of TKE or dissipation. In these situations, TKE budget terms such as the vertical transport term that are unaccounted for in this study could explain this discrepancy.

The vertical transport of TKE has not been investigated much over mountainous terrain in previous investigations due to dataset constraints and perception that this term is usually small. However, previous studies over flat homogeneous terrain have acknowledged this term can be important for redistributing turbulence near the CBL top (e.g. Moeng and Sullivan 1994; Caughey and Palmer 1979). These findings suggest that vertical transport and redistribution of TKE in the presence of large updrafts can also be an important turbulence mechanism in a CBL over complex terrain.

3.6 Summary and conclusions

The goal of this investigation was to determine the dominant mechanisms important for the generation of TKE maxima over an isolated mountain in a CBL. TKE and associated budget terms were estimated from airborne *in-situ* and TODWL to investigate TKE structure within and above the CBL. The analysis focused on three different flight plans over the Eastern Slope during the 06Oct_{PM}, 10Oct_{AM}, and 17Oct_{PM} flight period and one flight plan over Granite Peak during the 17Oct_{PM} flight period.

Two different types of CBLs, one characterized by weak CBL winds and a layer of shear at the CBL top and the other by relatively stronger CBLs winds and shear, illustrated how features of the CBL over mountainous terrain affect the TKE structure. During both types of CBLs, regions of increased buoyancy-generated TKE coincide with ridge tops, especially at the lower levels above these terrain features. Buoyancy becomes less important for TKE generation at higher altitudes above topography, which is consistent with previous studies.

As found in CBLs over flat terrain, shear generated TKE due to the entrainment of momentum played a significant role in the shear topped CBL. This mechanism was

due to the interaction of localized convective plumes generated over topography and the stable layer. During periods characterized by moderate winds and shear, wave breaking occurred and contributed to the shear generation of TKE. Previous theoretical and numerical studies suggest that the presence of a critical level or a small Richardson number layer in strong ambient flow favors wave breaking and turbulent billows. The case presented in this study not only provides observational evidence for this process but also shows that turbulent billows can occur over mountainous terrain within a CBL characterized by weak to moderate winds 5-10 m s^{-1}.

The use of TODWL in the calculation of shear production term proved to be particularly useful. TODWL observations were used to visualize the vertical and horizontal flow structure in the same region as *in-situ* aircraft flight legs. The spatial changes in the flow, given by the TODWL, provided valuable information on the spatial variability of vertical wind shear that would otherwise be missed using radiosonde or *in-situ* observations.

In some instances, the observed TKE is not explained well by buoyancy or shear production. The vertical transport and redistribution of TKE could explain some of this uncertainty. Although this term is commonly ignored, the vertical transport of TKE could be an important mechanism of TKE production over complex terrain

This study showed that even over an isolated mountain, determining the factors important for turbulence development is not straightforward. There are numerous interactions between CBL phenomena (e.g. thermals, eddies, and entrainment) and dynamical phenomena (e.g. topographical forced flow) that affect the location and development of TKE maxima. A few different processes responsible for TKE production are found that have not been previously noted in CBLs over complex terrain. The results from this study can inform modelers and future studies on important mechanisms for TKE development. Additionally, they provide important information for model validation and planning of future studies investigating turbulence over complex terrain.

Chapter 4

Conclusion

4.1 Summary and Conclusions

The main aim of this study was to investigate the structure of the TKE field over and around an isolated mountain. This study had two main objectives. The first focused on investigating the effects of topography, flow structure, and stability on the location of TKE maxima in and above the CBL. The second was to investigate the dominant mechanisms and underlying processes important for the generation of TKE maxima over complex topography. To address these objectives, airborne *in-situ* 10 Hz meteorological measurements and TODWL observations of the horizontal and vertical flow structure collected by a Twin Otter research aircraft during the fall MATERHORN-X experiment, at Dugway Proving Grounds, Utah, were used.

In the first part of this thesis, TKE was estimated from the wind velocity components measured by aircraft over five main regions over and around Granite Peak. These regions include the Sagebrush, Big Gap, Playa, Granite Peak, and the Eastern Slope. The flight legs were flown over these regions to investigate how effects from different surface and terrain types influence CBL turbulence. The spatial variability of TKE across flight legs was investigated, and TKE maxima were identified. In addition, TODWL wind profiles and *in-situ* airborne observations were used to examine the effects of the ambient flow structure and stability on TKE. Terrain was shown to influence TKE significantly. The largest TKE maxima were found over ridge tops on the Eastern Slope, the mountain crest of Granite peak, and in the Big gap. The generation of TKE over the ridge tops and mountain crest was attributed to 1) shear production associated with forced flow over topography and the downward transport of faster flow from aloft and 2) buoyant

production associated with increased heat fluxes over ridge tops and the mountain crest. These regions of increased TKE were characterized by the presence of dynamically and thermally induced flow features such as breaking waves and organized convective plumes, respectively. TKE maxima in center and exit of the Big gap were due to two different mechanisms 1) the Bernoulli or 'venturi' effect that accelerated the air passing through the gap, and a produced a turbulent wake at the gap exit and 2) the generation of lee side turbulence in the wake south of Granite Peak as northerly flow went over and around the mountain. This type of turbulence could have also occurred without the presence of a gap. Interestingly, the location and magnitude of TKE maxima were found to be rather independent of the ambient flow structure and stability. We found that there was no consistent relationship between flow and stability and the observed TKE.

The second part of this thesis investigated the relative contribution of shear and buoyancy generated turbulence and the processes important for affecting the observed TKE field and associated maxima during several case studies. We used turbulence based aircraft data, Doppler wind lidar, and surface meteorological observations collected during the MATERHORN-X campaign (Fernando et al. 2015). The spatial variability of the TKE budget terms, primary sources, and sinks of turbulence associated with the various TKE maxima were identified. Shear production correlated well with TKE and in many instances was the primary source of turbulence. It was found that shear production of TKE was associated with the downward transport of higher momentum air from aloft. The transport of higher momentum air was due to enhanced entrainment in the upper part of the CBL and with lee wave-breaking regions above the CBL top. The contribution of buoyancy production was large over ridge tops and the mountain crest, where convective plumes and topographically forced uplift were observed. The interaction of these convective plumes and the stable layer increased shear production in the CBL indirectly by entraining faster upper-level flow downward. Buoyancy decreased with height and became negligible and even negative at upper levels.

This thesis provided a detailed and comprehensive investigation of how an isolated mountain and surrounding terrain can influence the TKE structure within and above a CBL. *In-situ* and TODWL observations of the turbulence and flow field provide a valuable dataset for the evaluation of numerical models. Future model simulations will

hopefully add to the understanding of the current study by investigating how buoyant plumes, lee wave breaking, and entrainment of FA air into the CBL over topography affect the TKE structure. While this study provides insight into a number of mechanisms and processes that are important for turbulence generation, future research is needed to further the understanding of CBL turbulence structure over complex terrain.

Appendix A

Appendix

A.1 Twin Otter instrumentation

The TO is an instrumented twin-engine turboprop aircraft. Previously, TO aircraft measurements were performed in many field experiments around the world focusing on the CBL process studies like the Southern California Ozone Study - NARSTO (Vuilleumier et al., 2001), the Coupled Boundary Layers/Air-Sea Transfer Defense Research Initiative (CBLAST DRI, Zhang et al., 2009), the VAMOS Ocean-Cloud-Atmosphere-Land Study Regional Experiment (VOCALS-REX, Mechoso et al. 2009), the 2010 California Research at the Nexus of Air Quality and Climate Change field study (CalNex, Ryerson et al., 2013), and very recently, the Physics of Stratocumulus Top experiment (POST, Malinowski et al. 2013). In situ instruments include Rosemount total temperature probe, Krypton fast Humidity sensor, Dew Point Temperature (EdgeTech, Chilled Mirror device), Wind (Radome, flow angle probe, TAS, Mean Wind, Slip- and Attack angles), Barometric, Dynamic, Radome-Angle Pressures, and Infrared temperature sensor for surface temperature field along the track. In addition to the meteorological and turbulence instrumentations, the TO also included aerosol probes and positions devices: Condensation Particle Counter (3010), Ultrafine Condensation Particle Counter (3025), TANS Vector platform attitude (Trimble, Inc; GPS, Pitch, Roll, Heading), NovAtel GPS, C-MIGITS-III, GPS/INS. Time series of state variables, turbulence flux, profiles of vertical velocity, horizontal wind speed and direction from VAD, SNR as a proxy for aerosol distribution, LOS radial velocity field from stare measurements.

A.2 Twin Otter Doppler Wind Lidar

A nadir-pointing scanning Doppler lidar aboard a Twin Otter flight performed measurements of both vertical velocity and horizontal wind speed in addition to the aerosol backscatter profiles. The key aim behind the deployment of the TODWL (Twin Otter Doppler Wind Lidar) was to capture interaction between mesoscale and synoptic scale flows, obtain wind measurements at high spatial resolution over horizontals distances of at least a few tens of km as well as spatial variability in the daytime *zi* and the locations of the key aerosol layers over the experimental area. The TODWL also provides vertical cross-sections of aerosol backscatter measured along the flight track which we used to estimate spatially resolved fields of *zi*.

TODWL provides two dimensional cross-sections of the absolute wind vector with high accuracy (< 0.1 m s^{-1} in three components of wind) and high vertical (50 m) and horizontal (≈ 1.5 km) resolution. The TODWL is equipped with a 2-micron wind lidar with coherent detection technique (Godwin et al. 2012). The receiving unit consists of two rotating refractive wedges on a scanner mounted on the aircraft side door that deflect the lidar beam off-nadir such that it performs conical scans below the aircraft at an azimuth step of 30^o. A total of 12 such stares were performed in about 20-25 s during an entire scan covering a distance of $\approx$ 1-1.2 km. Additionally, TODWL performs nadir pointing measurements for 5 s between two consecutive conical scans. The individual profiles are accumulated to 1 s averages in order to obtain better SNR. The few occasionally remaining outliers are removed individually during the post-processing.

Appendix B

Appendix

B.1 Prevailing synoptic conditions during flight missions

IOP's during MATERHORN were designated during periods of relatively similar clear, calm, and quiescent synoptic conditions. Four IOP's were selected for analysis in the present study (IOP 4: 6-7 October, IOP 5: 9-10 October, IOP 6: 14-15 October, and IOP 7: 17 October). Each IOP spanned over 12-30 hours, which facilitated the capture of boundary layer processes taking place during the morning and evening transitional periods.

B.1.1 6-7 October 2012 (IOP 4)

The 850 mb and 700 mb winds during 6-7 October were northwesterly on the order of 1-3 m s^{-1} and 3-5 m s^{-1} respectively. These winds were associated with a northeasterly edge of the upper level ridge located over the experimental area. At the surface, high pressure was located over the northern Great Plains (northeast of Granite Mountain). This setup provided clear skies and high pressure to build into the experimental area over the course of IOP 4. Surface winds, associated with the western edge of the surface high pressure, were northwesterly and on the order of 3-5 m s^{-1} during the daytime portions of the IOP 4. In general, the experimental region was dominated by weak synoptic forcings and clear quiescent conditions.

B.1.2 9-10 October 2012 (IOP 5)

At the surface, a broad area of high pressure, associated with a southward intruding cold air mass, existed over the U.S north central Great Plains, and low pressure existed

off the central California coast and the desert southwest. The 700 mb winds were west-northwesterly and on the order of 3-5 m s^{-1} and 850 mb winds north-northwesterly on the order of 2-3 m s^{-1} over Dugway during late afternoon on 9 October. On 10 October, surface high pressure developed to the southeast of Dugway. Late on 9 October the upper-level winds changed from weak west-northwesterly to moderate 5-7 m s^{-1} south-southwesterly winds. The southwesterly winds grew in strength the remainder of IOP 5, with the strongest upper level winds of 7-10 m s^{-1} occurring on 10 October. In general, dry conditions persisted till the end of 9 October. IOP 5 took place during a transition from dry quiescent west-northwesterly flow to a moderate south-southwesterly upper level flow.

B.1.3 14-15 October 2012 (IOP 6)

Between 12 and 13 October, a disturbance associated with a passage of an upper level low brought precipitation to the Dugway area. Surface high pressure and dry conditions moved into the region on 14 October. During IOP 6, the 700 mb winds over Dugway transitioned from moderate north-northwesterly (5-7 m s^{-1}) to weak west-southwesterly upper flow (2-3 m s^{-1}). Surface level winds were primarily weak south-southeasterly and on the order of 2-3 m s^{-1}. In general, there was a broad ridge and anticyclonic conditions characterized the prevailing synoptic conditions over the Dugway experimental area and dry fair weather conditions existed for the entire IOP 6.

B.1.4 17 October 2012 (IOP 7)

Unlike the previous IOP's, the synoptic conditions that characterized IOP 7 were moderate rather than quiescent, and the IOP lasted over approximately half the time period ($\approx$ 12 hrs) of previous IOP's. At the beginning of 17 October, surface conditions over the experimental area were dominated by high pressure and variable winds. A shallow upper level trough deepened over the course of 17 October and brought increasingly moderate synoptic conditions to the region. The 700 mb upper level winds increased to moderate speeds (10-15 m s^{-1}) during IOP 7. The peak synoptic winds occurred at the beginning of IOP 7 and decreased throughout the remainder of the IOP. Cold air advection at the surface, associated with northwesterly upper level and surface winds

over Dugway, brought relatively cooler and drier air into the Dugway region for IOP 7. The synoptic conditions that characterized IOP 7 were the strongest of the four IOP's.

Bibliography

Attié, J., A. Druilhet, P. Durand, and B. Bénech, 1997: Two-dimensional structure of mountain wave observed by aircraft during the pyrex experiment. *Annales Geophysicae*, Springer-Verlag, Vol. 15, 823–839.

Baines, P., 1979: Observations of stratified flow past three-dimensional barriers. *Journal of Geophysical Research: Oceans (1978–2012)*, **84 (C12)**, 7834–7838.

Baines, P. G., 1987: Upstream blocking and airflow over mountains. *Annual review of fluid mechanics*, **19 (1)**, 75–95.

Banta, R. M., 1984: Daytime boundary-layer evolution over mountainous terrain. part 1: Observations of the dry circulations. *Monthly Weather Review*, **112 (2)**, 340–356.

Boers, R., and E. Eloranta, 1986: Lidar measurements of the atmospheric entrainment zone and the potential temperature jump across the top of the mixed layer. *Boundary-Layer Meteorology*, **34 (4)**, 357–375.

Boers, R., E. Eloranta, and R. Coulter, 1984: Lidar observations of mixed layer dynamics: Tests of parameterized entrainment models of mixed layer growth rate. Tech. rep., DTIC Document.

Bougeault, P., and P. Lacarrere, 1989: Parameterization of orography-induced turbulence in a mesobeta–scale model. *Monthly Weather Review*, **117 (8)**, 1872–1890.

Caughey, S., and S. Palmer, 1979: Some aspects of turbulence structure through the depth of the convective boundary layer. *Quart. J. Roy. Meteor. Soc*, **105 (81)**, 1–827.

Caughey, S., and J. Wyngaard, 1979: The turbulence kinetic energy budget in convective conditions. *Quarterly Journal of the Royal Meteorological Society*, **105 (443)**, 231–239.

Caughey, S. J., 1982: Observed characteristics of the atmospheric boundary layer. *Atmospheric turbulence and air pollution modelling*, Springer, 107–158.

Chou, S.-H., D. Atlas, and E.-n. Yeh, 1986: Turbulence in a convective marine atmospheric boundary layer. *Journal of the atmospheric sciences*, **43 (6)**, 547–564.

Conzemius, R. J., and E. Fedorovich, 2006a: Dynamics of sheared convective boundary layer entrainment. part i: Methodological background and large-eddy simulations. *Journal of the atmospheric sciences*, **63 (4)**, 1151–1178.

Conzemius, R. J., and E. Fedorovich, 2006b: Dynamics of sheared convective boundary layer entrainment. part ii: Evaluation of bulk model predictions of entrainment flux. *Journal of the atmospheric sciences*, **63 (4)**, 1179–1199.

Corby, G., 1954: The airflow over mountains. a review of the state of current knowledge. *Quarterly Journal of the Royal Meteorological Society*, **80 (346)**, 491–521.

Demko, J. C., and B. Geerts, 2010: A numerical study of the evolving convective boundary layer and orographic circulation around the santa catalina mountains in arizona. part ii: Interaction with deep convection. *Monthly weather review*, **138 (9)**, 3603–3622.

Doran, J., W. Shaw, and J. Hubbe, 1995: Boundary layer characteristics over areas of inhomogeneous surface fluxes. *Journal of applied meteorology*, **34 (2)**, 559–571.

Doran, J., and Coauthors, 1992: The boardman regional flux experiment. *Bulletin of the American Meteorological Society*, **73 (11)**, 1785–1795.

Fedorovich, E., and R. Conzemius, 2008: Effects of wind shear on the atmospheric convective boundary layer structure and evolution. *Acta Geophysica*, **56 (1)**, 114–141.

Fernando, H., and Coauthors, 2015: The materhorn-unraveling the intricacies of mountain weather. *Bulletin of the American Meteorological Society*, **(2015)**.

Foken, T., and B. Wichura, 1996: Tools for quality assessment of surface-based flux measurements. *Agricultural and forest meteorology*, **78 (1)**, 83–105.

Godwin, K., S. De Wekker, and G. Emmitt, 2012: Retrieving winds in the surface layer over land using an airborne doppler lidar. *Journal of Atmospheric and Oceanic Technology*, **29 (4)**, 487–499.

Greenhut, G. K., and S. J. Singh Khalsa, 1987: Convective elements in the marine atmospheric boundary layer. part i: Conditional sampling statistics. *Journal of climate and applied meteorology*, **26 (7)**, 813–822.

Hahn, D. C., 1980: *Observed characteristics of turbulence in the atmospheric boundary layer over mountainous terrain*. Department of Atmospheric Science, Colorado State University.

Henz, J. F., 1974: *Colorado High Plains Thunderstorm Systems: A Description Radar-synoptic Climatology*.

Houghton, D. D., and A. Kasahara, 1968: Nonlinear shallow fluid flow over an isolated ridge. *Communications on Pure and Applied Mathematics*, **21 (1)**, 1–23.

Howard, L. N., 1961: Note on a paper of john w. miles. *J. Fluid Mech*, **10 (4)**, 509–512.

Hoxit, L. R., 1974: Planetary boundary layer winds in baroclinic conditions. *Journal of the Atmospheric Sciences*, **31 (4)**, 1003–1020.

Hunt, J., and W. Snyder, 1980: Experiments on stably and neutrally stratified flow over a model three-dimensional hill. *Journal of Fluid Mechanics*, **96 (04)**, 671–704.

Jiang, Q., and J. D. Doyle, 2004: Gravity wave breaking over the central alps: Role of complex terrain. *Journal of the atmospheric sciences*, **61 (18)**, 2249–2266.

Jiang, Q., J. D. Doyle, V. Grubišic, and R. B. Smith, 2010: Turbulence characteristics in an elevated shear layer over owens valley. *Journal of the Atmospheric Sciences*, **67 (7)**, 2355–2371.

Kaimal, J., and J. Wyngaard, 1990: The kansas and minnesota experiments. *Boundary-Layer Meteorology*, **50 (1-4)**, 31–47.

Kaimal, J., J. Wyngaard, D. Haugen, O. Coté, Y. Izumi, S. Caughey, and C. Readings, 1976: Turbulence structure in the convective boundary layer. *Journal of the Atmospheric Sciences*, **33 (11)**, 2152–2169.

Kaimal, J., J. Wyngaard, Y. Izumi, and O. Coté, 1972: Spectral characteristics of surface-layer turbulence. Tech. rep., DTIC Document.

Karacostas, T. S., and J. D. Marwitz, 1980: Turbulent kinetic energy budgets over mountainous terrain. *Journal of Applied Meteorology*, **19 (2)**, 163–174.

Kirshbaum, D. J., 2013: On thermally forced circulations over heated terrain. *Journal of the Atmospheric Sciences*, **70 (6)**, 1690–1709.

Kirshbaum, D. J., and C.-C. Wang, 2014: Boundary layer updrafts driven by airflow over heated terrain. *Journal of the Atmospheric Sciences*, **71 (4)**, 1425–1442.

Kossmann, M., R. Vögtlin, U. Corsmeier, B. Vogel, F. Fiedler, H.-J. Binder, N. Kalthoff, and F. Beyrich, 1998: Aspects of the convective boundary layer structure over complex terrain. *Atmospheric Environment*, **32 (7)**, 1323–1348.

LeMone, M. A., 1973: The structure and dynamics of horizontal roll vortices in the planetary boundary layer. *Journal of the Atmospheric Sciences*, **30 (6)**, 1077–1091.

Lenschow, D., 1970: Airplane measurements of planetary boundary layer structure. *Journal of Applied Meteorology*, **9 (6)**, 874–884.

Lenschow, D., B. Stankov, and L. Mahrt, 1979: The rapid morning boundary-layer transition.

Lenschow, D., and P. Stephens, 1980: The role of thermals in the convective boundary layer. *Boundary-Layer Meteorology*, **19 (4)**, 509–532.

Lenschow, D. H., 1974: Model of the height variation of the turbulence kinetic energy budget in the unstable planetary boundary layer. *Journal of the Atmospheric Sciences*, **31 (2)**, 465–474.

Lenschow, D. H., and B. B. Stankov, 1986: Length scales in the convective boundary layer. *Journal of the atmospheric sciences*, **43 (12)**, 1198–1209.

Lothon, M., A. Druilhet, B. Bénech, B. Campistron, S. Bernard, and F. Said, 2003: Experimental study of five föhn events during the mesoscale alpine programme: From synoptic scale to turbulence. *Quarterly Journal of the Royal Meteorological Society*, **129 (592)**, 2171–2193.

Mahrt, L., 1998: Flux sampling errors for aircraft and towers. *Journal of Atmospheric and Oceanic technology*, **15 (2)**, 416–429.

Mayr, G. J., 2005: Gap flows–our state of knowledge at the end of map. *Hrvatski meteorološki časopis*, **40 (40)**, 6–10.

Michels, B. I., and A. M. Jochum, 1995: Heat and moisture flux profiles in a region with inhomogeneous surface evaporation. *Journal of hydrology*, **166 (3)**, 383–407.

Miles, J. W., 1961: On the stability of heterogeneous shear flows. *Journal of Fluid Mechanics*, **10 (04)**, 496–508.

Moeng, C.-H., and P. P. Sullivan, 1994: A comparison of shear-and buoyancy-driven planetary boundary layer flows. *Journal of the Atmospheric Sciences*, **51 (7)**, 999–1022.

Orlanski, I., 1975: A rational subdivision of scales for atmospheric processes. *Bulletin of the American Meteorological Society*, **56**, 527–530.

Pino, D., and J. Vilà-Guerau De Arellano, 2008: Effects of shear in the convective boundary layer: analysis of the turbulent kinetic energy budget. *Acta Geophysica*, **56 (1)**, 167–193.

Randall, D. A., and W. H. Schubert, 2004: Dreams of a stratocumulus sleeper. Cambridge University Press, 95–114 pp.

Raymond, D. J., and M. H. Wilkening, 1982: Flow and mixing in new mexico mountain cumuli. *Journal of the Atmospheric Sciences*, **39 (10)**, 2211–2228.

Rotach, M. W., and D. Zardi, 2007: On the boundary-layer structure over highly complex terrain: Key findings from map. *Quarterly Journal of the Royal Meteorological Society*, **133 (625)**, 937–948.

Scorer, R., 1953: Theory of airflow over mountains: Ii-the flow over a ridge. *Quarterly Journal of the Royal Meteorological Society*, **79 (339)**, 70–83.

Stull, R. B., 1988: An introduction to boundary layer meteorology.

Sullivan, P. P., C.-H. Moeng, B. Stevens, D. H. Lenschow, and S. D. Mayor, 1998: Structure of the entrainment zone capping the convective atmospheric boundary layer. *Journal of the atmospheric sciences*, **55 (19)**, 3042–3064.

Tennekes, H., 1973: A model for the dynamics of the inversion above a convective boundary layer. *Journal of the atmospheric sciences*, **30 (4)**, 558–567.

Večenaj, Ž., D. Belušić, V. Grubišić, and B. Grisogono, 2012: Along-coast features of bora-related turbulence. *Boundary-layer meteorology*, **143 (3)**, 527–545.

Vickers, D., and L. Mahrt, 1997: Quality control and flux sampling problems for tower and aircraft data. *Journal of Atmospheric and Oceanic Technology*, **14 (3)**, 512–526.

Weigel, A. P., F. K. Chow, and M. W. Rotach, 2007a: The effect of mountainous topography on moisture exchange between the "surface" and the free atmosphere. *Boundary-layer meteorology*, **125 (2)**, 227–244.

Weigel, A. P., F. K. Chow, and M. W. Rotach, 2007b: On the nature of turbulent kinetic energy in a steep and narrow alpine valley. *Boundary-layer meteorology*, **123 (1)**, 177–199.

Whiteman, C. D., 1990: Observations of thermally developed wind systems in mountainous terrain. *Atmospheric processes over complex terrain, Meteor. Monogr*, **45**, 5–42.

Wulfmeyer, V., and Coauthors, 2011: The convective and orographically-induced precipitation study (cops): the scientific strategy, the field phase, and research highlights. *Quarterly Journal of the Royal Meteorological Society*, **137 (S1)**, 3–30.

Wyngaard, J., and O. Coté, 1971: The budgets of turbulent kinetic energy and temperature variance in the atmospheric surface layer. *Journal of the Atmospheric Sciences*, **28 (2)**, 190–201.

Young, G. S., 1988: Turbulence structure of the convective boundary layer. part ii. phonenix 78 aircraft observations of thermals and their environment. *Journal of the atmospheric sciences*, **45 (4)**, 727–735.

Zeman, O., and H. Tennekes, 1977: Parameterization of the turbulent energy budget at the top of the daytime atmospheric boundary layer. *Journal of the Atmospheric Sciences*, **34 (1)**, 111–123.